DRY DEPOSITION OF SPECIATED AMBIENT FINE PARTICLES MEASURED USING EDDY CORRELATION MASS SPECTROMETRY

by

Daniel A. Gonzales

A Dissertation Presented in Partial Fulfillment
of the Requirements for the Degree
Doctor of Philosophy

ARIZONA STATE UNIVERSITY

December 2007

DRY DEPOSITION OF SPECIATED AMBIENT FINE PARTICLES

MEASURED USING EDDY CORRELATION MASS SPECTROMETRY

by

Daniel A. Gonzales

has been approved

November 2007

Graduate Committee Members:

Jonathan O. Allen, Chair
Jean M. Andino
Ronald J. Calhoun
Nancy B. Grimm
Jeffrey J. Heys

ACCEPTED BY THE GRADUATE COLLEGE

ABSTRACT

Dry deposition of fine particles from the atmosphere is an important mechanism for the removal of particulate pollution and for the addition of materials to downwind ecosystems. The focus of this research was the development and demonstration of a novel technique to directly measure local chemically speciated fine particle dry deposition—eddy correlation mass spectrometry (ECMS). For regional scale assessment of ecosystem perturbations due to nitrogen deposition at urban-influenced Sonoran desert sites the inferential method was used to measure fluxes of gaseous and particulate nitrogen species.

Synchronous wind and aerosol composition measurements were made at an agricultural site using a sonic anemometer and a Quadrupole Aerosol Mass Spectrometer in order to demonstrate the ECMS method. Chemically speciated fine particle deposition velocities were measured; these were not dependent on chemical composition. Mean deposition velocities were 0.05 centimeters per second during moderately unstable atmospheric conditions, in agreement with previous measurements.

The eddy correlation method requires rapid and synchronous measurements of wind velocity and concentration. For practical reasons, the aerosol sample is usually drawn through a sampling line to a sensor. The attenuation of fine particle concentration fluctuations was studied for isokinetically sampled laminar flow using experiments and theoretical calculations. Measured attenuation of isokinetically sampled particle concentration fluctuations was less than 1% at 5 Hertz, suitable for eddy correlation measurements. Maximum frequency response in the isokinetic sample was predicted to be approximately four orders of magnitude higher than in the main flow.

Inferential deposition measurements are practical for multiple sites over a large study area. Atmospheric nitrogen species were measured at Sonoran desert sites located upwind, within, and downwind of Phoenix, Arizona. Air-surface exchange parameterizations were developed from eddy correlation measurements. Characteristic inferred deposition fluxes were 0.92, 2.28, and 1.47 kilograms nitrogen per hectare per year at the upwind, core, and downwind sites, respectively. The main contributors to nitrogen flux were nitric acid and ammonia.

ACKNOWLEDGMENTS

I would like to thank the people who have contributed, in their own ways, to this work. First, my sincere thanks to my advisor, Jonathan Allen, for his professional and technical guidance. His constant support and high standards have provided me with a solid foundation for my future endeavors. I also thank the members of my thesis committee, Jean Andino, Ron Calhoun, Nancy Grimm, and Jeff Heys, for their comments and advice.

Thanks to the supporting staff in the Department of Chemical Engineering: Claire Zanakis, Alicia Stiers, Paul Grillos, and Veronica Lupampa. Thanks to Fred Pe a who provided guidance and assistance with the materials for all of the experimental work.

The Salt River eddy correlation experiment was partially funded by the Environmental Protection Agency (R-82817201-0). Thanks to Ken Smith at the Massachusetts Institute of Technology, Doug Worsnop, John Jayne, and Manjula Canagaratna at Aerodyne Research, Inc., and Jose-Luis Jimenez at the University of Colorado at Boulder for developing the Q-AMS eddy correlation mode. Bobby Ramirez, Ondrea Barber, and Stan Belone from the Salt River Pima-Maricopa Indian Community helped coordinate the experiment. Thanks to Henry Guzman and his family who kindly provided electrical power and access to the Salt River site.

The nitrogen deposition measurement is based upon work supported by the National Science Foundation under Grant No. DEB-0514382 (Ecosystem Response to N and Organic C Deposition from the Urban Atmosphere) and Grant No. DEB-0423704 (Central Arizona - Phoenix Long-Term Ecological Research). Thanks to those who collected and analyzed the filter and denuder samples: Ryan Sponseller, Sam Norlin, Quincy Stewart, David Huber, and Cathy “CK” Kochert. Tom Colella at the Goldwater Environmental Lab assisted with the ammonia analysis method development. Thanks to Linda Williams, Nikol Grant, Estella O’Hanlon, Stevan Earl, Wayne Porter, and Corinna Gries at CAP LTER and the Global Institute for Sustainability. Thanks to Bob Sherman and the staff at the Lost Dutchman State Park for allowing use of the LDP site. Thanks to Randy Redman from the Arizona Department of Environmental Quality for assistance in setting up the tower at the LDP site. Thanks to Bob Martin and the staff at

the Desert Botanical Garden who helped install the tower at the DBG site. Special thanks to Andrew Martin and Boy Scout Troop 824 for help installing the tower at the DBG site. Thanks to the staff at the White Tank Mountains Regional Park for access to the WTM site.

I would like to thank several students who have helped in the experimental work. Sean Coury coded the first version of the model to calculate deposition velocities from standard meteorological measurements. Amber Summers helped design and complete the isokinetic sampling line experiments. Corey Tyree provided particle loss calculations for the isokinetic sampling setup used for the sampling line and eddy correlation experiments, helped set up the Salt River eddy correlation experiment, and offered extensive feedback for all of this work.

The Java interface for data acquisition using National Instruments hardware (jnidaq class), which was used in the eddy correlation and sampling line experiments, followed the development of the NIDaq class by José Lu s Malaquias at LaSEEB - Instituto de Sistemas e Robótica, Lisbon, Portugal. Quang Han, an undergraduate student, coded and tested an update of the jnidaq class.

I thank the fellows and associates of the IGERT in Urban Ecology and the CAP LTER graduate student community for helpful discussions of the experimental results. Thanks to my friends, Corey Tyree, Fred Pe a, Olga Alexandrova, Quincy Stewart, Ryan Sponseller, Dave Huber, Sam Norlin, Xia Su, and Teresa Sun, for their help and support. I thank my family for their love and support. Especially, I thank Paula and Caleb for their love, encouragement, and patience.

TABLE OF CONTENTS

Page

Page

Page

LIST OF TABLES

LIST OF FIGURES

Figure Page

Figure Page

1. BACKGROUND AND SIGNIFICANCE

Atmospheric particulate matter (PM) concentrations are regulated by the United States Environmental Protection Agency (US EPA) because PM has been shown to negatively affect human health (Dockery *et al.*, 1993). Increases in the concentration of fine particles, those smaller than 2.5 μm in diameter ($PM_{2.5}$), are strongly associated with increases in mortality rates in the US (Dockery *et al.*, 1993). A prospective mortality study showed that for every 10 $\mu g\ m^{-3}$ increase in fine particle concentration, the risk of death by cardiopulmonary disease and lung cancer increases by 6% and 8% respectively, after controlling for smoking, diet, obesity, and other risk factors (Pope *et al.*, 2002).

From a simple mass balance perspective, the concentration of particles in the atmosphere is the integrated difference between the rate of input into the system and the rate of removal from the system. Therefore, the rate of removal of PM from the atmosphere affects the concentration of PM in the atmosphere and thus affects human health. Particles are eventually removed from the atmosphere by deposition to the earth's surface. The atmospheric lifetime of fine aerosol particles based on the total removal rate is on the order of days to weeks (Seinfeld and Pandis, 1998). Thus, atmospheric aerosols also represent a vector for the transport of anthropogenic pollution hundreds of kilometers downwind of their source.

The chemical components associated with fine particles can affect ecosystems when they interact with water, soil, and plants. For example, particulate nitrate deposition provides an additional source of nitrogen, which is a limiting nutrient in most of the world's terrestrial ecosystems (Vitousek *et al.*, 1997a). As a result, particulate nitrate deposition increases rates of plant production and carbon storage within ecosystems (Vitousek *et al.*, 1997b). Nitrogen deposition also has the potential to reduce biological diversity by favoring species that are better adapted to high nutrient levels (Stevens *et al.*, 2004).

In order to understand the effects of particulate matter on human health and ecosystems, quantitative information about the atmospheric concentrations of aerosol fine particles is required. Dry deposition (removal in the absence of precipitation) is a key component of the removal process, especially in arid regions such as the western United States, where it is the

dominant removal mechanism (Fenn *et al.*, 2003). The generally accepted formulation for dry deposition is to assume that the dry deposition flux, F, is proportional to the concentration, c,

$$F = -v_d c \tag{1.1}$$

where v_d is known as the deposition velocity (Businger, 1986). The deposition velocity has units of length per time, and is positive for a downward flux ($F < 0$).

The rate of fine particle removal by dry deposition is difficult to measure, resulting in a wide range of deposition velocity estimates (Wesely and Hicks, 2000). Semiempirical models have been constructed from measurements of the loss rate of well-characterized particles to ideal surfaces in wind tunnels. Direct measurement of particle deposition using the eddy correlation technique have improved estimates, including size resolved deposition velocities. Particle deposition velocity measurements differ by an order of magnitude and differ from predicted values by 2-3 orders of magnitude (Gallagher *et al.*, 1997). Estimates of speciated fine particle deposition velocities have not been directly measured, mainly because fine particle measurement methods were inadequate for application of the eddy correlation technique.

The focus of this research is the measurement of speciated fine particle dry deposition using eddy correlation mass spectrometry (ECMS). This work included: design and validation of a method to sample fine particles for eddy correlation measurements that maintains the temporal coherence of the aerosol with minimal particle loss; quantification of the ECMS system response; and field deployment of the ECMS system to measure speciated fine particle dry deposition. Atmospheric deposition of gaseous and particulate nitrogen was also measured in the Phoenix, Arizona, area using the inferential method.

1.1. Fine Particles in the Atmosphere

1.1.1. *Effect of Fine Particles on Human Health*

The human health effects of fine particles have been demonstrated by Dockery *et al.* (1993), who showed that there is an association between fine particle ($PM_{2.5}$) concentrations and increased mortality in six U.S. cities. The adjusted mortality rate ratio was 26% higher in the most polluted city studied compared to the least polluted (see Figure 1.1). No corre-

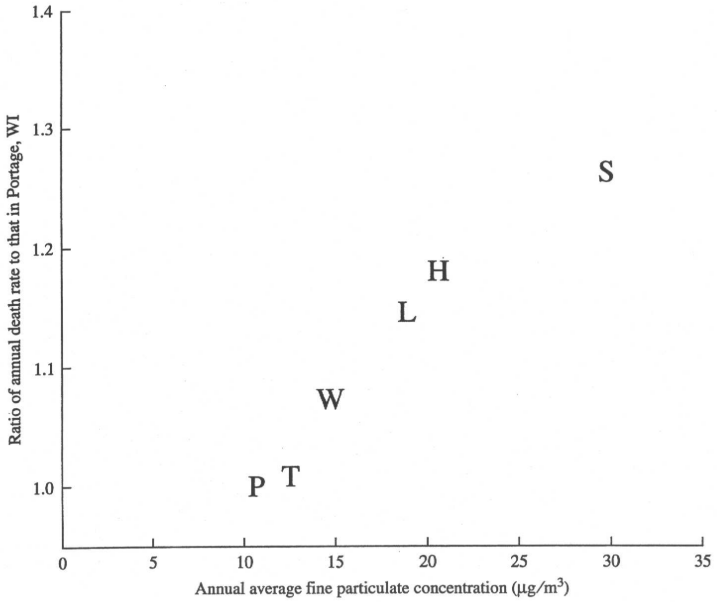

Figure 1.1: Ratio of death rates to that in Portage, WI, as a function of fine particle concentration (P = Portage, WI; T = Topeka, KA; W = Watertown, MA; L = St. Louis, MO; H = Harriman, TN; and S = Steubenville, OH) (Dockery *et al.*, 1993).

lation was found between total particle concentrations, which includes all particle sizes, and increased mortality. Fine particle pollution has been demonstrated to have a larger impact than total particle pollution. For each 10 μg m^{-3} increase in fine particle pollution, the risk of mortality from all causes, cardiopulmonary causes, and lung cancer increased by 4%, 6%, and 8%, respectively (Pope *et al.*, 2002).

Particle size is critical in determining human exposure since fine particles penetrate deeper into the lung (Brain and Valberg, 1979). Particle composition plays an important role since some particles are composed of less harmful chemicals, such as sea salt, while other particles, such as diesel soot, contain toxic components that can damage the lung tissue (Pyne, 2002).

1.1.2. *Sizes of Atmospheric Particles*

Atmospheric aerosol particles range in size from a few nanometers to hundreds of micrometers. The idealized size distribution shown in Figure 1.2 is a paradigm of the atmo-

spheric aerosol, including the processes that influence the particle size distribution. Particles of different sizes behave in the environment in fundamentally different ways because chemical composition, atmospheric transport, and deposition varies with particle size. Therefore, any discussion of these atmospheric aerosols must distinguish between particles based on their size.

Fine particles can be segregated into two sub-modes: the ultrafine mode and the accumulation mode (see Figure 1.2). The ultrafine mode consists of particles with diameter, D_p, less than 0.1 μm; these particles are formed from the condensation of combustion gases and from nucleation of atmospheric gases to form new particles. The accumulation mode consists of particles from 0.1 to 2.5 μm, formed by coagulation of ultrafine particles and condensation onto existing particles. Fine particles are also directly emitted into the atmosphere from natural and anthropogenic sources (not shown in Figure 1.2). The coarse particle mode are those larger than 2.5 μm, consisting of man-made and natural particles that are mechanically generated.

1.1.3. *Sources of Fine Particles*

Particles are generated from natural and anthropogenic sources, including primary and secondary particles (see Figure 1.2). Primary particles are those that are emitted directly into the atmosphere while secondary PM includes that formed in the atmosphere by condensation of precursor gases to form new particles or add mass to existing particles.

Human activities produce fine particles and gases that contribute to fine PM. Soot, which contains both elemental and organic carbon, comes solely from primary emissions since it is formed during combustion of carbon-containing materials. Estimates of global emissions of soot aerosols are in the range of 5–20 Tg y^{-1} (Kiehl and Rodhe, 1995). Industrial sources add an additional 40–130 Tg y^{-1} of primary fine particles (Kiehl and Rodhe, 1995).

Combustion from industrial activities and agricultural biomass burning emits precursor gases, such as SO_2, NO_x (NO + NO_2), and volatile organic compounds (VOCs) that react to form secondary particles or condense on existing particles to form larger particles. Sulfate

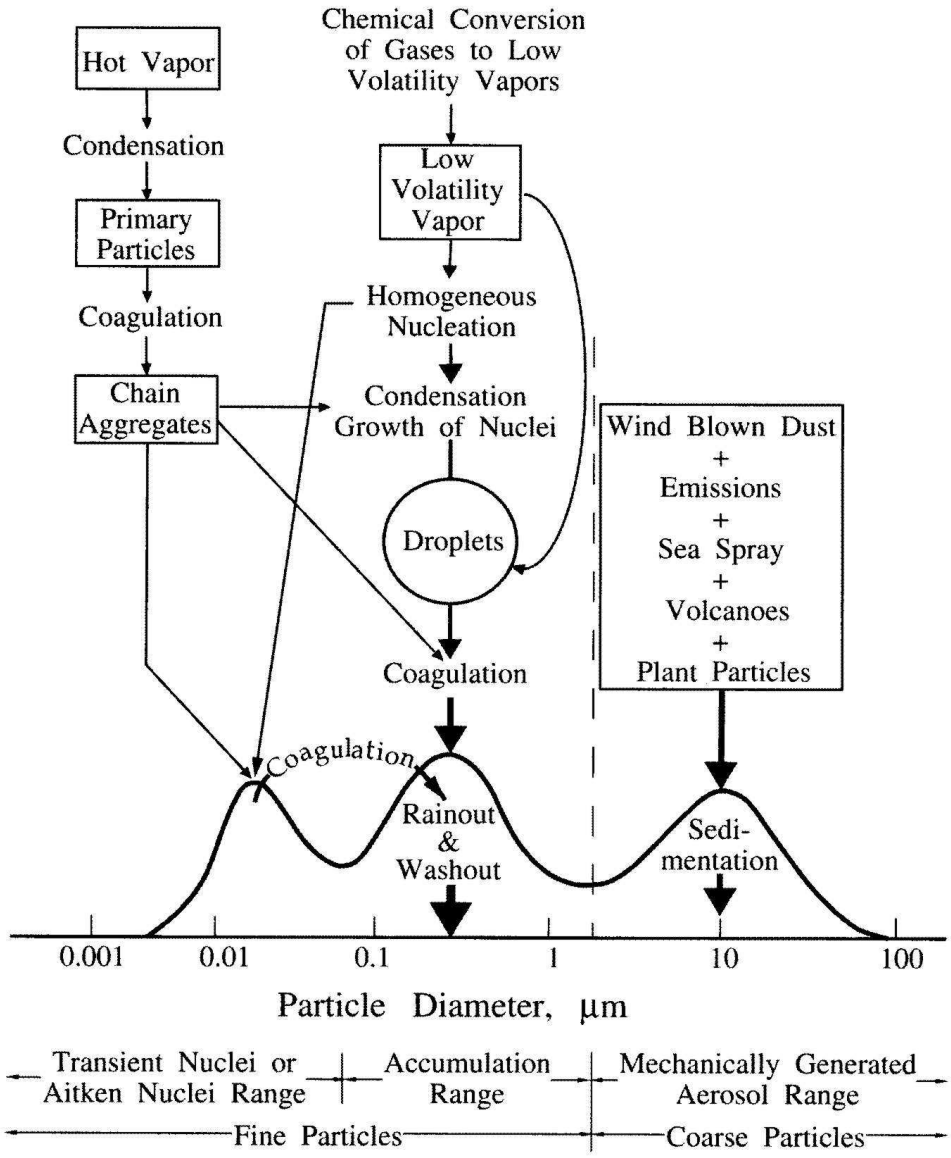

Figure 1.2: Idealized atmospheric aerosol size distribution (Whitby and Cantrell, 1976). Major sources and sinks are shown for coarse and fine particle modes.

and nitrate, assumed to occur as ammonium salts in fine particles, are emitted at estimated rates of 170–250 Tg y^{-1} and 25–65 Tg y^{-1}, respectively (Kiehl and Rodhe, 1995). In addition, agricultural activities increase soil emissions of NO_x, and emissions of ammonia from animal waste and losses of excess fertilizers. Ammonia is important in the atmosphere because it is the primary gaseous base and the ammonium (NH_4^+) ion is an important component of atmospheric aerosols.

Primary particles from natural sources are usually generated by mechanical processes. These tend to be coarse mode particles, such as soil and volcanic dust, although some sources can produce fine mode particles (Kiehl and Rodhe, 1995). Biogenic gas phase emissions of sulfates, NO_x, VOCs, and ammonia produce some secondary fine particles through gas-to-particle conversion. Other natural sources of precursor gases include sulfates from volcanic SO_2 and VOCs from biomass burning.

1.1.4. *Fine Particle Concentration and Composition*

Total fine particle mass concentration typically ranges from 5 μg m^{-3} in remote areas to 90 μg m^{-3} in highly polluted urban areas (Solomon *et al.*, 1989; Heintzenberg, 1989). Fine particle emissions in nonurban areas are less than half that of urban areas, yet the average total fine particle mass is only a factor of 2 lower than that of urban areas (see Figure 1.3). This reflects the relatively long atmospheric residence time of fine particles, sufficient to allow for long range transport from urban areas (Seinfeld and Pandis, 1998). The average composition of these two regions is similar, also indicating that long range transport of particles from urban areas is important to downwind regions.

A typical atmospheric fine aerosol contains about 10–30% organic carbon (OC), 5–40% sulfate (SO_4^{2-}), 0–10% elemental carbon (EC), 5–10% ammonium (NH_4^+), and 5–20% nitrate (NO_3^-) (Solomon *et al.*, 1989; Heintzenberg, 1989) (see Figure 1.3). The remaining 20–50% of the total fine particle mass, shown as “Other” in Figure 1.3, is made up of trace metals, sea salt and other constituents. Nonurban areas tend to have much lower fractions of OC and EC than urban areas; these pollutants are attributed to anthropogenic combustion sources.

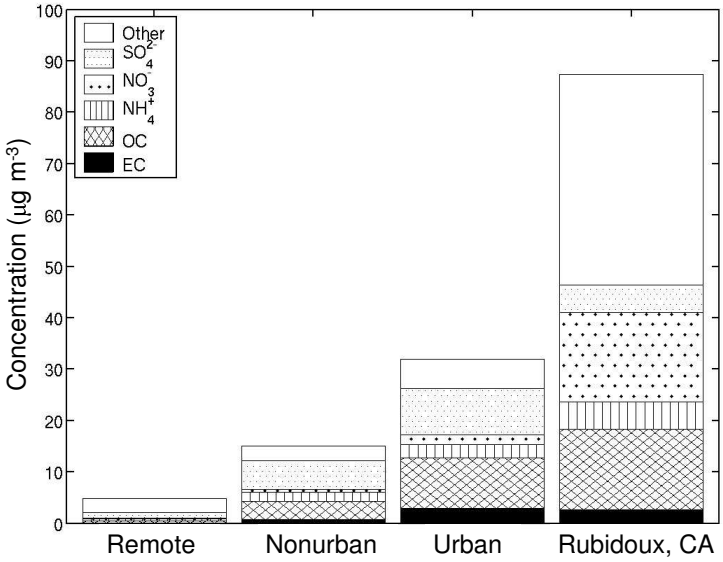

Figure 1.3: Global average of total fine particle mass and composition for regional atmospheric aerosols. Remote data are from 11 sites from 13 experiments at remote island locations or research vessels at sea. Nonurban data are from 14 sites from 16 experiments on the continents but away from large urban or industrial sources. Urban data are from 21 experiments in 19 areas in Chinese, European, Japanese, and United States cities. All of the above data is from the years 1976-1986 (Heintzenberg, 1989). Data for Rubidoux, CA is the 1986 annual average from data collected in the Los Angeles area (Solomon *et al.*, 1989).

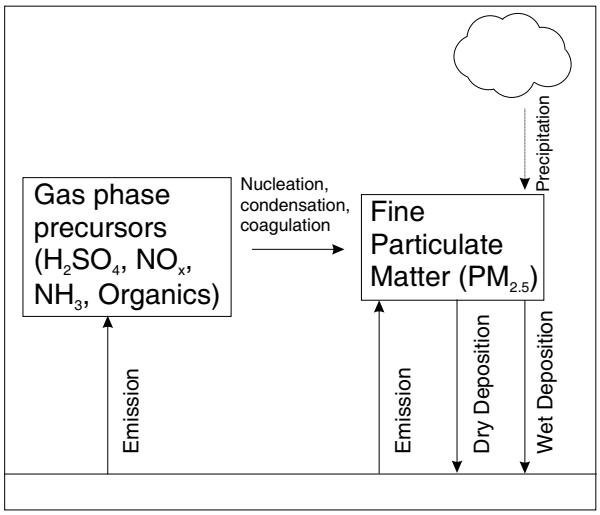

Figure 1.4: Atmospheric fine particle production, emission, and modification. Fine particles are eventually removed from the atmosphere by wet and dry deposition.

1.1.5. *Removal of Fine Particles from the Atmosphere*

Particles are eventually removed from the atmosphere by wet and dry deposition (see Figure 1.4). Wet deposition involves incorporation of particles into water droplets and transfer to the surface during precipitation events. The wet deposition can occur from either scavenging of particles by clouds with subsequent precipitation or by interception of particles by falling precipitation. Cloud or fog deposition, a part of wet deposition, involves interaction of particle laden water droplets directly with the surface. This mechanism can be important in some areas, but the magnitude is comparatively small at lower altitudes (Wesely and Hicks, 2000).

Particles are also removed from the atmosphere in the absence of precipitation by dry deposition. A convenient framework commonly used for the interpretation of gas and particle dry deposition is to consider the deposition process as occurring in three steps (Hicks *et al.*, 1987) (see Figure 1.5). The first step of dry deposition to a forest canopy, for example, is turbulent transport through the atmosphere to the quasi-laminar sublayer near the leaf surface. Second is transport through the surface sublayer to the surface by Brownian diffusion (transport to the surface due to interaction with gas molecules), impaction (interaction with

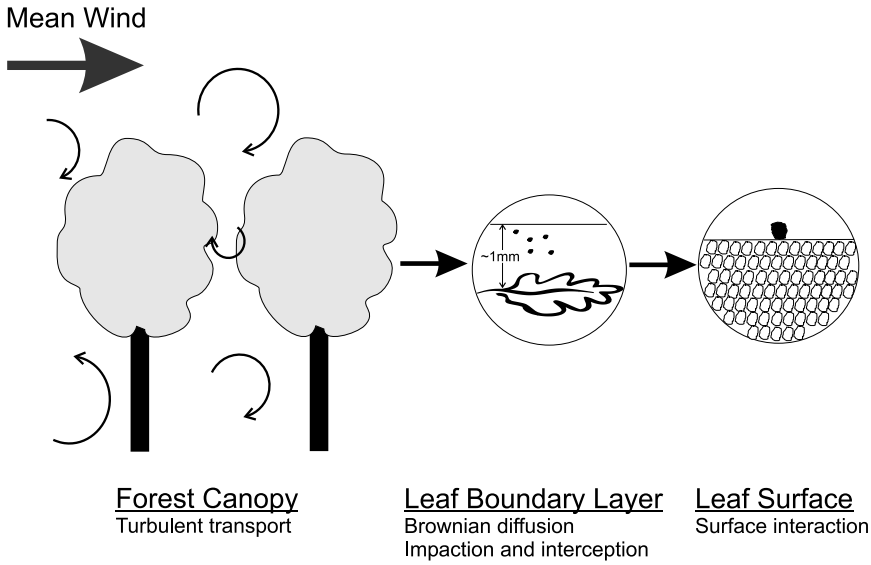

Figure 1.5: Simplified schematic of the dry deposition processes to a forest canopy. The process is considered in three steps: turbulent transport from the atmosphere to the boundary layer near the surface of individual leaves, boundary layer transport across the sublayer to the surface, and interaction with the surface.

the surface due to inertia), or interception (interaction with the surface due to proximity) (see Figure 1.6). The final step is interaction with the surface in which particles adhere to the surface. The processes that influence deposition depend on particle size (diffusion, impaction, etc.) and composition (surface interaction), as well as atmospheric properties that influence turbulent transport. These will be discussed in more detail in Section 1.6.

Dry deposition is thought to be comparable in magnitude to wet deposition in many cases, including sulfur deposition in eastern North America, sulfate and nitrate input to an oak forest in Tennessee, and atmospheric acidity in the western United States (Davidson and Wu, 1990). In arid regions, dry deposition may account for more than half of the total mass deposition of ionic chemical species that are primarily associated with fine particles, e.g. sulfate and nitrate (Lovett, 1994; Fenn *et al.*, 2003).

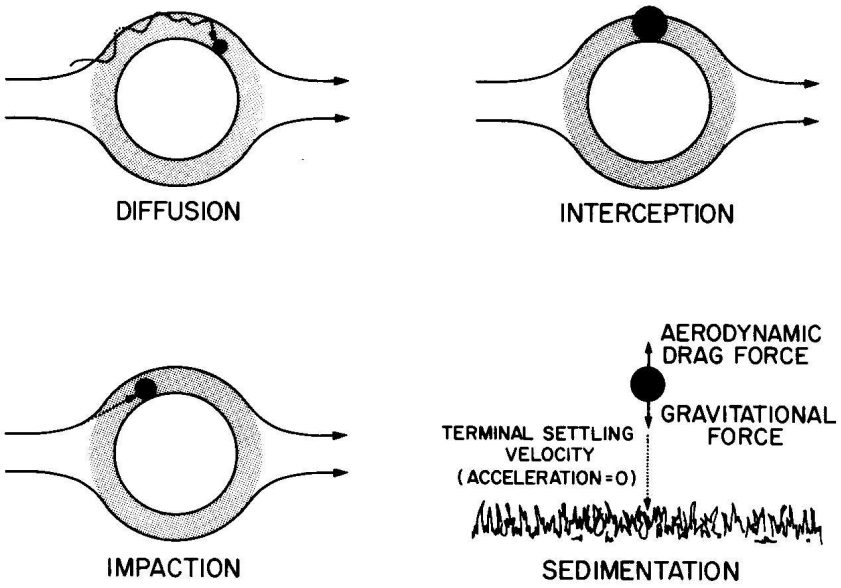

Figure 1.6: Mechanisms of particle transport through the surface sublayer. The obstacle is a circular cylinder surrounded by a surface sublayer (shaded area). Mean air flow is the thick lines around the obstacle and the particle path is the dashed line (Davidson and Wu, 1990).

1.2. Effects of Dry Deposition on Ecosystems

1.2.1. *Nutrient Cycling*

Human activities have significantly perturbed the natural cycles of sulfur (S), nitrogen (N), and other chemical species. For example, in natural ecosystems, N cycling is dominated by internal cycling between plants and various soil pools with little input or output (Schlesinger, 1997). Total N deposition rates have increased from about 7.8 Tg N y^{-1} to about 31 Tg N y^{-1} as oxidized N (NO_y) and from about 22 Tg N y^{-1} to about 48 Tg N y^{-1} as reduced N (NH_x) (Galloway, 1996). Similarly, estimates of preindustrial deposition rates for gas and particle phase S are about 240 Tg S y^{-1} and estimates of current rates are about 340 Tg S y^{-1} (Galloway, 1996).

The Phoenix, Arizona, metropolitan area is an example of an arid region with significant atmospheric pollution that results in increased deposition in and around the city. Modeled estimates of N dry deposition are about 7.5 kg N ha^{-1} y^{-1} for the upwind desert, 13.5 kg N ha^{-1} y^{-1} for the urban core and 15 kg N ha^{-1} y^{-1} for the downwind desert, with an

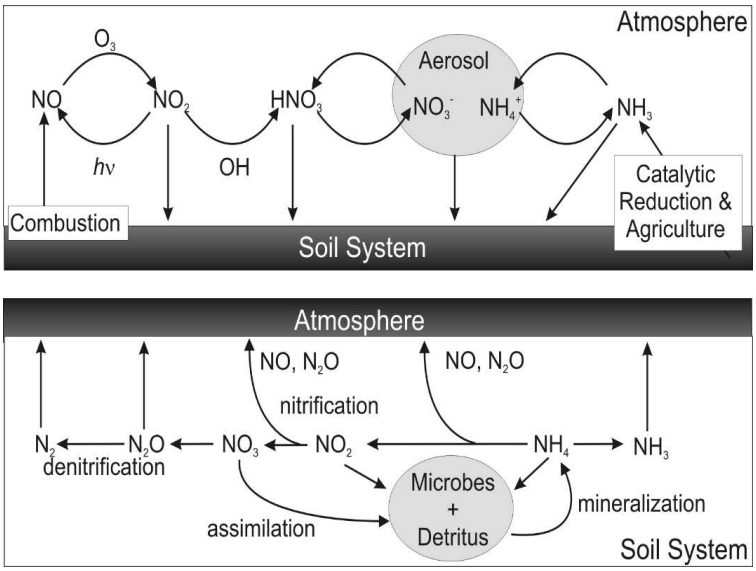

Figure 1.7: Simplified diagram of nitrogen cycling in the atmosphere and soil.

average of 12 kg N ha^{-1} y^{-1} for the entire modeled area (Fenn *et al.*, 2003). About 10% of the estimated totals are due to N in particulate form. For comparison, wet deposition averaged over the Phoenix area is estimated to be 2.4 kg N ha^{-1} y^{-1} (Baker *et al.*, 2001).

Nitrogen is the limiting nutrient in most of the world's terrestrial ecosystems (Vitousek *et al.*, 1997b). Anthropogenic sources account for more than half of terrestrial fixed N worldwide (Galloway *et al.*, 1995). The species that serve as important vectors for anthropogenic N deposition include 1) HNO_3 and NO_2 originally emitted as NO from combustion, 2) aerosol NO_3^- also from NO, 3) NH_3 emitted by agricultural processes and catalytic reduction, and 4) aerosol NH_4^+ originally emitted as NH_3 (see Figure 1.7).

Anthropogenic deposition increases the concentrations of N species in soil systems. The additional N provided by deposition of gas and particle phase species is a nutrient source for recipient ecosystems. This anthropogenic fertilization can increase rates of plant production and carbon storage within N-limited ecosystems (Vitousek *et al.*, 1997b). At the same time, N deposition can reduce biological diversity by favoring species that are better adapted to high nutrient levels (Stevens *et al.*, 2004).

The increase in available, fixed N from deposition also accelerates the rate of N cycling.

The rate of conversion of NH_4^+ to NO_2 and NO_3^- (nitrification) increases in response to increased N deposition (Fenn *et al.*, 2003). The overall rate of N cycling within the plant and soil system is thereby increased.

1.2.2. *Surface Water and Soil Acidification*

Acid deposition refers to the wet and dry deposition of acidic species. Once in the atmosphere, SO_2 and NO_x become oxidized to sulfate and nitrate through gas- and aqueous-phase oxidation. These species lower the pH of rainwater which increases the concentration of H^+ ions at the surface where it deposits. The acidity of the surface will increase once the buffering capacity is exhausted. In the same way, dry deposition of acidic species lowers the pH of the deposition surface.

In the case of surface waters, most of the acid-neutralizing capacity comes from the bicarbonate ion, HCO_3^-. As the concentration of H^+ increases, the equilibrium

$$2\ H^+ + HCO_3^- \rightleftharpoons\ CO_2 \cdot H_2O \tag{1.2}$$

shifts to the right and the bicarbonate in the water is consumed. The pH of the water remains unchanged if sufficient acid-neutralizing capacity is present. Once this supply of buffering ions is exhausted, the pH of the water will decrease. Individual surface waters vary in their composition, and hence their ability to neutralize acidity. Soils around the surface water may help to buffer the pH of the water by exchange of hydrogen ions with soil cations, such as Ca^{2+}, Mg^{2+}, Na^+, and K^+. Metals, such as aluminum, iron, manganese, copper, nickel, zinc, lead, cadmium, and mercury, may be solubilized as the pH decreases (Fernandez, 1990; Harvey, 1990).

Human induced increases in acid deposition have caused an observed increase in the acidity of lakes in polluted regions. For example, from 1957 to 1974, the pH of Lake Skarsj n in southwest Sweden decreased from about 5.3 to about 4.3 (Harvey, 1990) (see Figure 1.8). This caused about a tenfold increase in the concentration of manganese in the lake. Increased metal concentrations in lakes result in bioaccumulation and net metal export through lake runoff. Lime treatments are commonly used in efforts to neutralize lakes. The 1975 liming

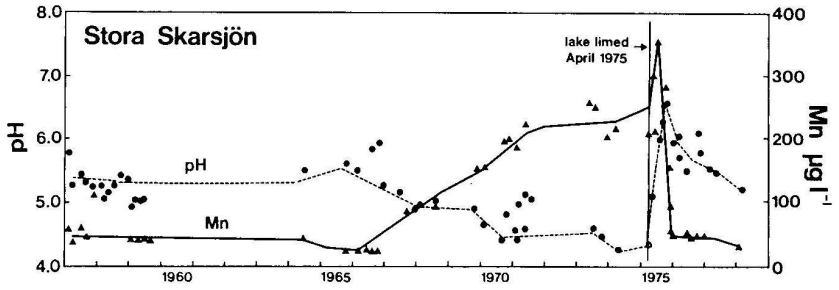

Figure 1.8: Acidification of Stora Skarsj n in southwest Sweden (Harvey, 1990). As the pH decreases metals such as manganese are solubilized, and increase in concentration. The lake was limed in 1975 to neutralize the pH and reduce metal concentrations.

of Lake Skarsj n had the desired effect of raising the pH and decreasing metal concentrations (see Figure 1.8) and the practice of lake liming remains common because of the large number of acidified lakes.

Decreases in the pH of surface waters cause changes in its chemistry which affect the aquatic biota. Some animal species, such as snails and crustaceans, are affected at pH values of about 6 (Fernandez, 1990). Field observations and laboratory studies show a correlation between increasing acidity and decreasing fish populations and fish diversity (see Figure 1.9). The main cause is thought to be the increased concentrations of aluminum and other metal species mobilized by acidic water (Fernandez, 1990).

Soils are similarly affected by acid deposition; soils with poor buffering capacity and low to moderate base saturation levels are most likely to be subject to rapid effects of acidic deposition (Fernandez, 1990). The increase in available hydrogen ions causes an increase in cation exchange capacity. This can lead to soil cation leaching and increased metal mobility. Aluminum mobility and toxicity in soils is associated with increased soil acidity. When soil base saturation is low, aluminum may be released by dissolution and hydrolysis or cation exchange. Soil acidity promotes aluminum toxicity with agricultural soil systems (Fernandez, 1990).

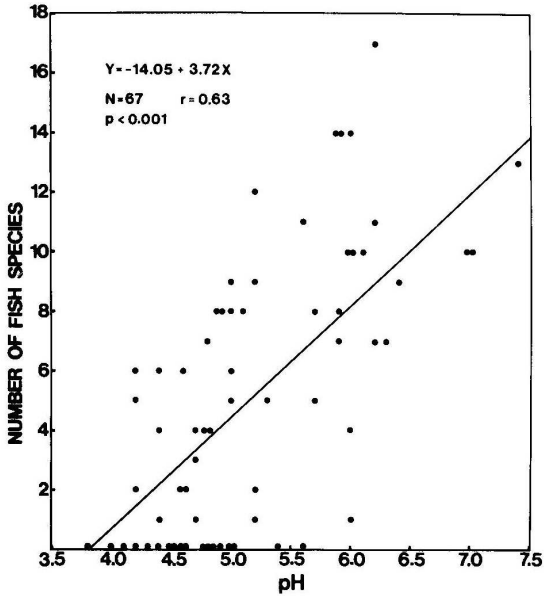

Figure 1.9: Observed correlation between the number of fish species and lake pH in La Cloche Mountain Lakes (Harvey, 1990).

1.3. Turbulent Transport in the Atmosphere

Turbulence is the process responsible for the dispersion and transport in the atmosphere. This is due to the irregular motion of fluid parcels, called eddies, in turbulent flows. The forces that generate turbulence, including surface friction, wind shear, and buoyancy, interact to produce turbulent mixing.

1.3.1. *Structure of the Atmospheric Boundary Layer*

The atmospheric boundary layer (ABL) is the layer of the atmosphere that is influenced by the earth's surface. Forcings from the ground on the air, including surface friction and vertical temperature gradients, combine with the effect of the earth's rotation to create turbulent mixing, which is sometimes used to define the height of the ABL. Because of the spatial and temporal variability of these processes, the height of the ABL can vary dramatically, ranging from hundreds of meters to a few kilometers (Stull, 1988).

On the timescale of days, the most important of these forcings is the vertical temperature profile, caused by the diurnal variation of incoming solar radiation (see Figure 1.10). The

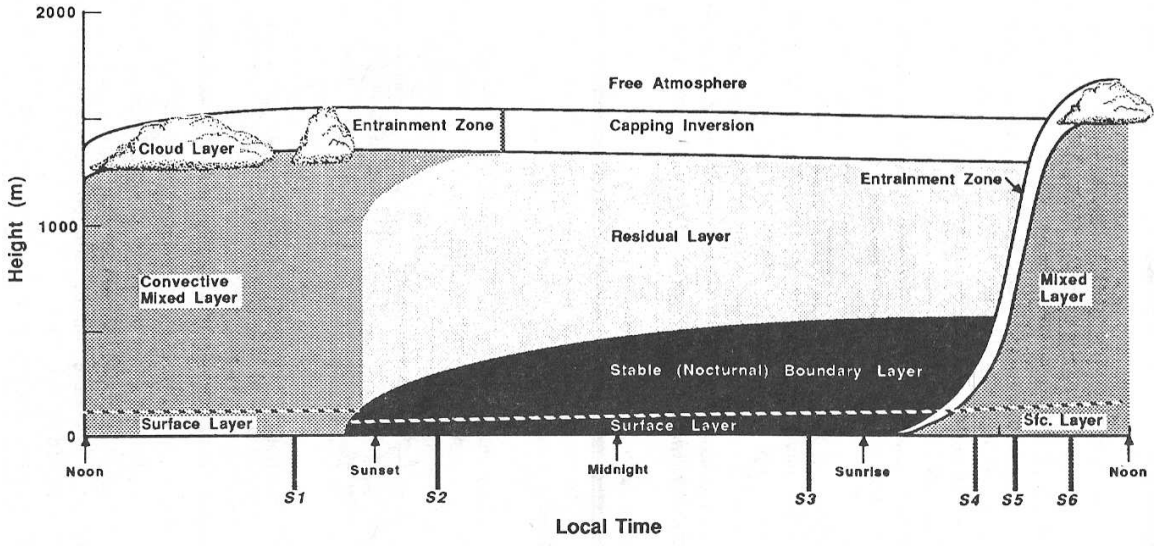

Figure 1.10: Evolution of the atmospheric boundary layer (ABL) in response to surface heating and cooling (Kaimal and Finnigan, 1994). At sunrise the ABL grows as the surface and the air above it warms, reaching its maximum height at the bottom of the inversion layer, z_i, at 1-2 km by mid-afternoon. At sunset the ground cools quickly along with the adjacent air, resulting in a layer of air that suppresses surface generated turbulence up to a nighttime ABL height, h.

height of the inversion layer, which will be described in detail in the next section, is based on the vertical temperature profile and defines the top of the ABL. Thus, the height of the daytime ABL, commonly termed the mixed layer, can reach 1-2 km and the height of the nighttime ABL, or stable boundary layer, is about an order of magnitude lower (Stull, 1988).

The surface layer makes up the bottom 10% of the ABL, where the air flow is insensitive to the earth's rotation and the influences of surface friction and the vertical temperature gradient dominate the wind structure (Stull, 1988). This layer is called the surface layer regardless of whether it is within the mixed layer or stable boundary layer (see Figure 1.10). A key feature of the surface layer is that the wind shear is constant with height, leading to the assumption that turbulent transport is constant within the surface layer. In fact, the surface layer height is defined by the extent of this constant flux layer. It is this layer that is of great interest since the turbulent transport in the surface layer controls overall surface-atmosphere exchange.

1.3.2. *Static Stability*

The vertical temperature profile is a useful way to characterize the atmosphere (Kaimal and Finnigan, 1994). Consider a deformable parcel of air with constant mass. If the parcel is forced upward, it will expand since the pressure decreases with height from the hydrostatic equation

$$\frac{dp(z)}{dz} = -\frac{Mgp(z)}{RT(z)} \tag{1.3}$$

where $p(z)$ is the atmospheric pressure as a function of the height, z, above the surface; M is the molecular weight of air; g is the gravitational constant; R is the gas constant; and $T(z)$ is the temperature as a function of height. If the expansion is adiabatic, that is, no heat is exchanged between the air parcel and its surroundings, the parcel will cool upon expansion. The parcel may have a different temperature than the surrounding air and it is this difference that affects the buoyancy of the air parcel, causing it to continue to rise or fall to its previous position.

The potential temperature, θ, is the temperature of an air parcel that is brought adiabatically to the surface

$$\theta = T\left(\frac{p}{p_0}\right)^{-(\gamma-1)/\gamma} \tag{1.4}$$

where T and p are the temperature and pressure at the original height, p_0 is the surface pressure, and $\gamma = \hat{c}_{\mathrm{p,air}}/\hat{c}_{\mathrm{v,air}}$, the ratio of the constant pressure to constant volume specific heat capacities of air. In the surface layer, $p \approx p_0$ so $\theta \approx T$. For air containing water vapor, the contribution of moisture to the air density is included by defining the virtual potential temperature

$$\theta_v = \theta\left(1 + \frac{R}{R_v}q\right) \tag{1.5}$$

where q is the specific humidity and R/R_v is the ratio of the ideal gas constant of dry air to that of water vapor which has a constant value of 0.61.

The virtual potential temperature is convenient since θ_v is constant with height under adiabatic conditions. Thus, a temperature profile based on the potential temperature is useful

to compare the vertical atmospheric temperature profile, or atmospheric lapse rate, to the adiabatic cooling rate of a displaced air parcel, or the adiabatic lapse rate to estimate atmospheric stability. The atmospheric lapse rate is

$$\frac{dT}{dz} = -\frac{g}{\hat{c}_{\mathrm{p,air}}} \tag{1.6}$$

and

$$\frac{d\theta_v}{dz} = 0 \tag{1.7}$$

For dry air the quantity $g/\hat{c}_{\mathrm{p,air}}$, commonly denoted Γ, is 9.76 K/km. If the atmospheric lapse rate is superadiabatic ($dT/dz > \Gamma$), the temperature of an air parcel forced upward will be warmer than that of the air at that height (see Figure 1.11). The density of the parcel will be less than that of the surrounding air and the parcel will be accelerated upward by buoyancy. The atmosphere is said to be unstable since any vertical forcing will be amplified by buoyancy. On the other hand, if the temperature of the parcel is colder than that of the surrounding air, resulting from a subadiabatic lapse rate ($dT/dz < \Gamma$), its density will be greater than that around it and the parcel will sink back to its original position. The atmosphere is said to be stable, where vertical motions are suppressed. In the special case that temperature increases with altitude, very strong stability results. This situation is called a temperature inversion. Neutral conditions result when the atmospheric lapse rate is equal to Γ (for dry air); then a displaced parcel will be at the same temperature as the surrounding air and will experience no net buoyancy forces.

The atmospheric lapse rate is therefore an important property of the atmosphere since this profile determines, in part, the degree to which turbulence propagates through the lower atmosphere. Static stability can be determined by comparison of the atmospheric lapse rate to the adiabatic lapse rate.

1.3.3. *Dynamic Stability*

The concept of static stability is applicable throughout the atmospheric boundary layer, including the surface layer where fluxes are measured. Static stability implies that no buoyant

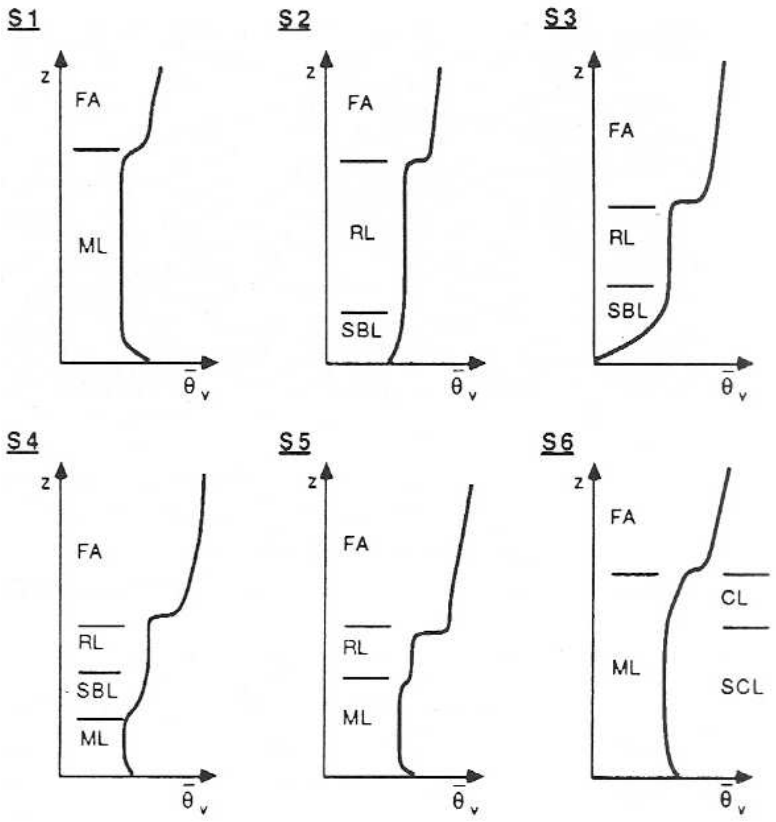

Figure 1.11: Potential temperature profiles in the atmosphere and their relation to atmospheric stability. Neutral conditions are found when the atmospheric lapse rate is adiabatic (vertical line). Stable conditions are found when the atmosphere is subadiabatic and unstable conditions are found when the atmosphere is superadiabatic.

forces are present to destabilize the flow. Destabilizing forces, such as surface friction and wind shear, commonly exist. It is therefore necessary to develop a way to estimate the dynamic stability of the surface layer, where the vertical and temporal variations of the forces that destabilize the flow are taken into account. This can be accomplished by comparing the relative magnitudes of the shear production of turbulence and suppression of turbulence by changes in buoyancy (Stull, 1988).

An indicator of dynamic stability is the nondimensional Richardson number, R_i, based on the ratio of the buoyancy and shear terms in the turbulence kinetic energy (TKE) budget equation (see Stull (1988) for derivation)

$$R_i = \frac{\left(\frac{g}{\overline{\theta}_v}\right)\left(\frac{\partial \overline{\theta}_v}{\partial z}\right)}{\left(\frac{\partial \overline{u}}{\partial z}\right)^2 + \left(\frac{\partial \overline{v}}{\partial z}\right)^2} \tag{1.8}$$

where u, v, and w are the streamline, lateral, and vertical wind velocities and overbars denote a time average. This equation makes some assumptions about the conditions under which atmospheric measurements are made which will be discussed in the following sections. The actual local gradients are rarely known, but over short time intervals it can be assumed that

$$\frac{\partial \overline{\theta}_v}{\partial z} \approx \frac{\Delta \overline{\theta}_v}{\Delta z} \tag{1.9}$$

and

$$\left(\frac{\partial \overline{u}}{\partial z}\right)^2 + \left(\frac{\partial \overline{v}}{\partial z}\right)^2 \approx \left(\frac{\Delta \overline{u}}{\Delta z}\right)^2 + \left(\frac{\Delta \overline{v}}{\Delta z}\right)^2 \tag{1.10}$$

Then the bulk Richardson number is

$$R_b \approx \frac{\left(\frac{g}{\overline{\theta}_v}\right)\Delta \overline{\theta} \Delta z}{(\Delta \overline{u})^2 + (\Delta \overline{v})^2} \tag{1.11}$$

This is a useful stability indicator close to the ground and is the form of the Richardson number most frequently used since measurements at discretely variable heights can be made (Stull, 1988).

Since wind shear is constant with height in the surface layer, stability can be estimated by estimating the production or suppression of turbulence by buoyancy. Scaling the produc-

tion term of the TKE equation by $-kz/u_*^3$ gives the stability parameter as

$$\zeta = \frac{z}{L} \tag{1.12}$$

where L is the Obukhov length given by

$$L = \frac{-\overline{\theta_v} u_*^3}{kg(\overline{w'\theta_v'})_0} \tag{1.13}$$

k is the von Karman constant ($k = 0.4$), $(\overline{w'\theta_v'})_0$ is the turbulent vertical heat flux (see below), and u_* is the friction velocity (Stull, 1988)

$$u_* = \left[\overline{u'w'}^2 + \overline{v'w'}^2\right]^{1/4} \tag{1.14}$$

The friction velocity is a velocity scale that varies with surface characteristics and wind speed, representing the effect of wind stress on the ground. The Obukhov length is a scaling parameter which is characteristic of mixing in the surface layer. Thus, the stability parameter, ζ, or the inverse of the Obukhov length, L^{-1}, can be used to indicate dynamic stability. Negative values of ζ, corresponding to positive buoyancy from the term $(\overline{w'\theta_v'})_0$, indicate unstable conditions and positive values indicate stable conditions. The Obukhov length can be assumed constant throughout the surface layer (Kaimal and Finnigan, 1994).

The terms $(\overline{w'\theta_v'})_0$, $(\overline{u'w'})$, and $(\overline{v'w'})$ in Equations 1.13 and 1.14 are known as eddy fluxes. Since atmospheric fluxes are almost entirely due to turbulent mixing, they can be defined in terms of the turbulent properties of the atmosphere. The flux across a horizontal plane implies a correlation between the vertical wind and the scalar. The covariance provides a direct measurement of the correlation

$$\overline{w'c'} = \frac{1}{N}\sum_{i=1}^{N}(w_i - \overline{w}) \cdot (c_i - \overline{c}) = \frac{1}{N}\sum_{i=1}^{N} w'c' \tag{1.15}$$

where c represents a scalar concentration, such as temperature, wind speed, or mass concentration. The scalar variables are separated into their mean and eddy parts, for example

$$w' = w - \overline{w} \tag{1.16}$$

where w' is the deviation from the mean and $\overline{w}$ is the mean. The eddy correlation method is an application of the direct experimental measurement of eddy fluxes and will be described in

detail in Section 1.4.

1.4. Eddy Correlation Method

Mass, energy, and momentum are exchanged between the surface and the atmosphere mainly by turbulent transport. In order to estimate transport across the atmosphere-surface interface from surface layer measurements, it is useful to first examine turbulence in the surface layer. In addition, some simplifying assumptions are made to facilitate this introduction; these will be reexamined in detail in the next section. In this section, a subset of the PROPHET 2001 field study data will be used to introduce the eddy correlation method (Gonzales *et al.*, 2006). Experimental methods were similar to those used during the Salt River experiment (Chapter 3).

1.4.1. *Conservation Equation for Scalar Fluxes*

The mass conservation in a control volume over a patch of the surface is the basic framework for interpreting mass transport and estimating micrometeorological fluxes. For clarity, c, which can represent any scalar quantity, will be used throughout the following development of the mass balance.

In rectangular Cartesian coordinates (see Figure 1.12), the concentration in the control volume must satisfy the continuity equation

$$\frac{\partial c}{\partial t} = -\nabla \cdot (u_i c) + \mathcal{D}\nabla^2 c + S_v \tag{1.17}$$

where u_i are the components of the wind velocity in the x_i directions (u, v, and w in the x, y, and z Cartesian coordinates respectively), $\mathcal{D}$ is the diffusion coefficient in air, and S_v is a volumetric source/sink term. The first term on the right-hand side of Equation 1.17 is the net rate of addition of c by advection, the second term is the net rate of addition of c by diffusion, and the last term accounts for sources or sinks of c within the control volume.

1.4.2. *Reynolds Decomposition of Atmospheric Quantities*

For a small volume of fluid in turbulent flow, u_i, as a function of time, fluctuates in a chaotic fashion with irregular deviations from a mean value because of its turbulent state. The

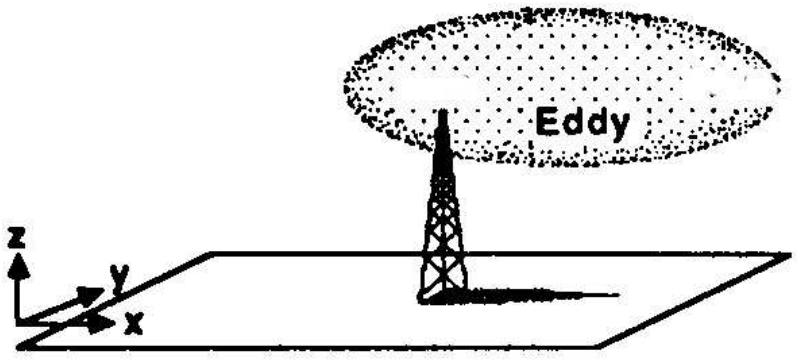

Figure 1.12: Schematic of a tower to measure fluxes above a surface patch (Stull, 1988). The Cartesian coordinate system is defined at the measurement point, oriented along the plane of the mean horizontal wind. The streamline, lateral, and vertical wind velocities (u, v, and w) correspond to the x, y, and z directions respectively.

actual velocity at any time is then the sum of the mean value, $\overline{u}_i$, and the deviation, u_i'

$$u_i = \overline{u}_i + u_i' \tag{1.18}$$

The time average operator is used to calculate the mean for a continuous variable as

$$\overline{u_i} = \frac{1}{t_0}\int_0^{t_0} u_i(t)dt \tag{1.19}$$

This is known as the Reynolds decomposition defined over the averaging time, t_0. The discrete form of this equation is

$$\overline{u}_i = \frac{1}{N}\sum_{i=1}^{N} u_i(t) \tag{1.20}$$

where N is the number of samples in the period t_0. The Reynolds decompositions of wind velocity data (u, v, and w) from the PROPHET 2001 field experiment show the irregular deviations of the instantaneous measurements from the mean over a 5-min averaging period (see Figure 1.13).

The following relations hold for Reynolds decomposition of turbulent variables (Stull,

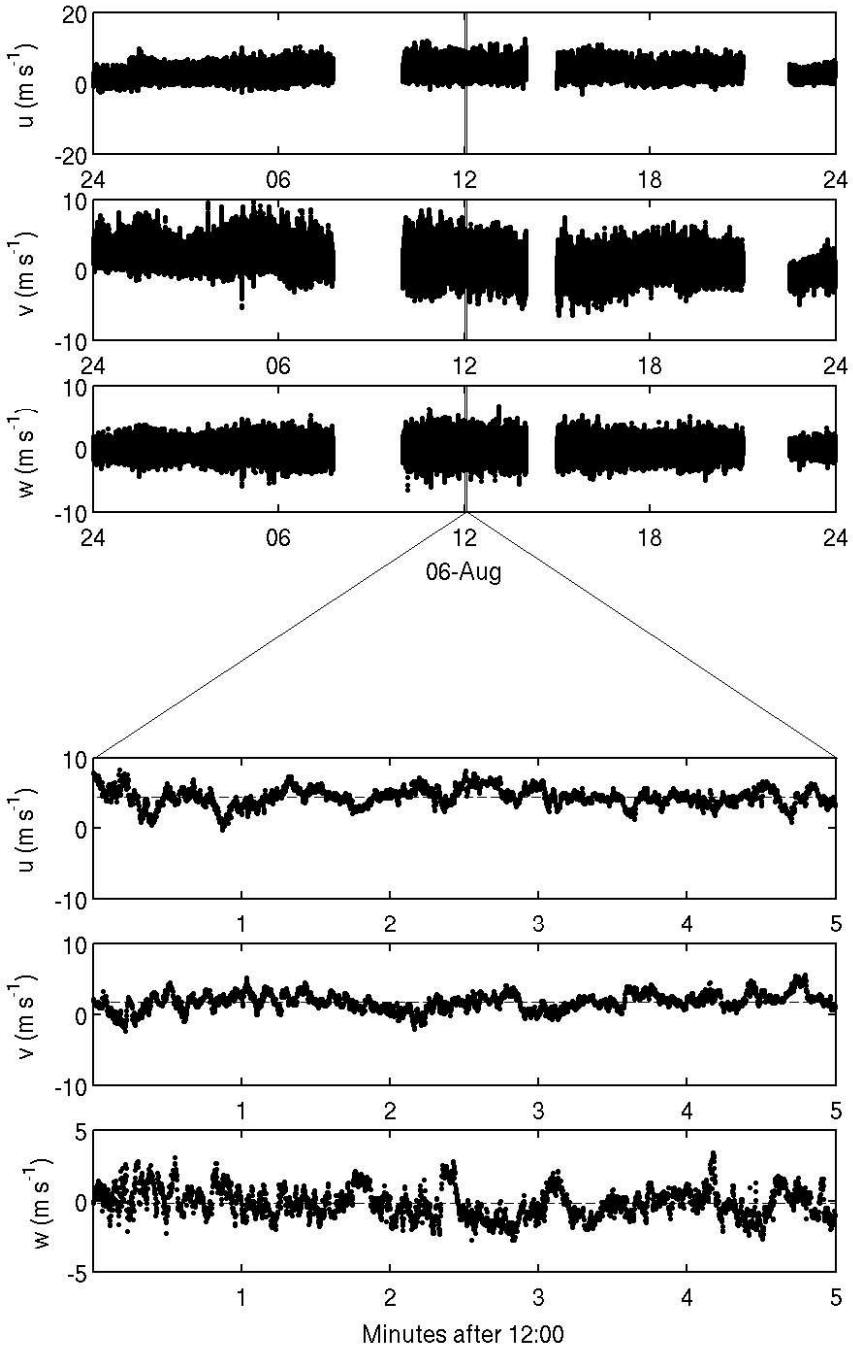

Figure 1.13: Reynolds decomposition of the wind velocity vectors (u, v, and w) on 6 August 2001. The turbulent part, u_i', of the 10 Hz data is calculated by subtracting the mean, $\overline{u}_i$ (dashed line in the lower figure), from the measured value, u_i over the averaging time, t_0 = 5 min.

1988)

$$\overline{\overline{u}_i} = \overline{u}_i \quad \overline{u'}_i = 0 \quad \overline{u_i' u_i'} \neq 0 \quad \overline{\overline{u}_i u_i'} = 0 \quad \overline{\frac{\partial}{\partial x_i} u_i} = \frac{\partial}{\partial x_i}\overline{u}_i \quad \overline{\frac{\partial}{\partial t} u_i} = \frac{\partial}{\partial t}\overline{u}_i \tag{1.21}$$

These rules of Reynolds averaging are useful in developing a method to estimate turbulent transport from measurable quantities. Although the net (or average) turbulent motion of the air is zero, i.e. $\overline{u'}_i = 0$, the turbulent part of u_i is nonzero. Nonlinear products such as $\overline{u'v'}$ are also nonzero because the local motions in the x and y directions may be correlated and this correlation represents a turbulent flux.

The scalar c can also be decomposed into a mean and fluctuating part, $c = \overline{c} + c'$. The Reynolds decomposition of the sonic temperature from the PROPHET 2001 field experiment shows the deviation of the temperature from the mean value caused by turbulent eddy mixing (Figure 1.14). The time average operator can be used on the equation of change (Equation 1.17) after Reynolds decomposition to yield

$$\frac{\partial \overline{c}}{\partial t} = -\frac{\partial}{\partial x_i}\overline{u}_i\,\overline{c} - \frac{\partial}{\partial x_i}\overline{u_i' c'} + \mathcal{D}\frac{\partial^2}{\partial x_i^2}\overline{c} + \overline{S_v} \tag{1.22}$$

The first term on the right-hand side accounts for the mean advection, the second term is turbulent transport, the third term is the molecular diffusion in air, and the last term accounts for sources or sinks within the control volume.

The ergodic hypothesis, the assumption that the time average is equivalent to the ensemble average, is used to develop Equation 1.22 (Stull, 1988). This implies that over the analysis period the turbulence is homogeneous, the properties of the flow are independent of horizontal position, varying only with height and time; and stationary, the statistics of the measurements do not vary over the averaging period.

1.4.3. *Simplifying Assumptions for Turbulent Transport*

Given the complexity of turbulent transport, it is common to simplify the analysis by eliminating some of the terms in the conservation equation. Assuming steady state, no sources or sinks in the control volume, and a horizontally uniform area, Equation 1.22 simplifies to

$$\frac{\partial}{\partial z}\overline{w'c'} = \mathcal{D}\frac{\partial^2 \overline{c}}{\partial z^2} \tag{1.23}$$

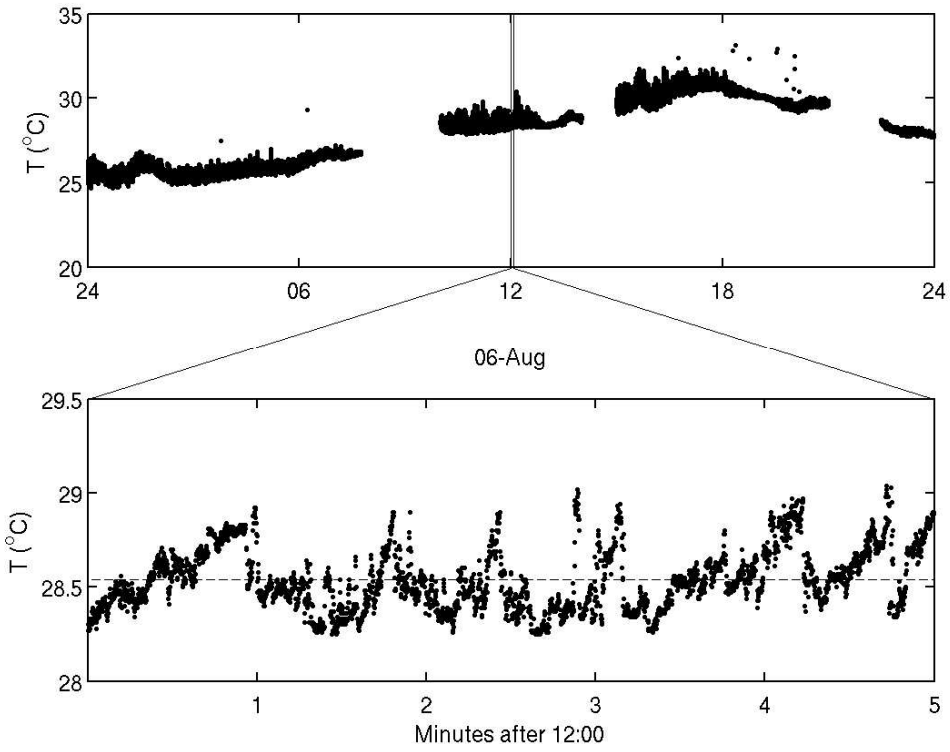

Figure 1.14: Reynolds decomposition of the sonic temperature on 6 August 2001. The turbulent part, T', of the 10 Hz data is calculated by subtracting the mean, $\overline{T}$ (dashed line in the lower figure), from the measured value, T, over the averaging time, t_0.

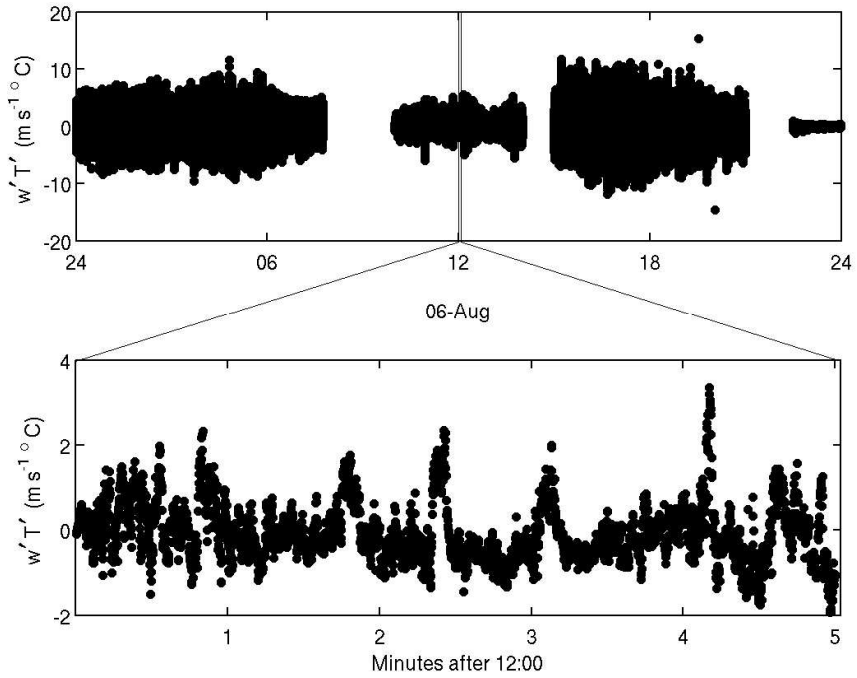

Figure 1.15: Turbulent sensible heat flux (unscaled) on the 10 Hz scale on 6 August 2001 study. The product $w'T'$ is nonzero at this resolution and the mean over longer averaging periods is also nonzero.

At a height, z_0, above the surface, turbulent transport is on the order of 10^{-9} kg m^{-3} s^{-1} and transport by molecular diffusion is negligible, on the order of 10^{-14} kg m^{-3} s^{-1}. Turbulence is suppressed near the surface, so turbulent transport decays to zero as z approaches zero. Thus, integrating Equation 1.23 with respect to height, the flux of c is

$$(\overline{w'c'})_{z_0} = -\mathcal{D}\left(\frac{\partial \overline{c}}{\partial z}\right)_0 \tag{1.24}$$

This equation implies that the vertical flux, F, is constant throughout the boundary layer. The right-hand side of the equation, which represents transport by diffusion at the surface, is not easily measured. However, the product of the w and c fluctuations, defined as the covariance, is generally nonzero (see Figure 1.15) and the correlation, $\overline{w'c'}$, can be measured directly.

The covariance is an indication of the degree of a correlation between two variables. The left-hand side of Equation 1.24 is known as the eddy flux since local fluctuations of vertical velocity and scalar concentration are correlated. The mean of the product of the variable parts

of two scalar quantities is the definition of the covariance (Equation 1.15)

$$\overline{w'c'} = \frac{1}{N}\sum_{i=1}^{N}(w_i - \overline{w}) \cdot (c_i - \overline{c}) = \frac{1}{N}\sum_{i=1}^{N} w'c' \tag{1.25}$$

If c represents temperature, gas concentration, or particle mass concentration, the covariance can be scaled to determine fluxes of sensible heat, gas phase species, or particulate species. The eddy correlation measurement method is a well-known application of this property of turbulent transport (Businger, 1986). For example, the covariance of w and T represents the kinematic eddy heat flux for over 30-min averaging periods from the PROPHET 2001 study (Figure 1.16). The sensible eddy heat flux can then be calculated by scaling the kinematic flux

$$Q_H = \rho_{\text{air}}\, \hat{c}_{\text{p,air}}\, \overline{w'T'} \tag{1.26}$$

where ρ_{air} is the density of air. Similarly, the eddy fluxes of latent heat and momentum are

$$Q_E = L_v\, \overline{w'q'} \tag{1.27}$$

and

$$F_M = \rho_{\text{air}}\, \overline{u'w'} \tag{1.28}$$

where L_v is the latent heat of vaporization of water.

1.5. Constraints on Eddy Correlation Measurements

In the previous section, assumptions were used to simplify the analysis of micrometeorological fluxes and demonstrate the concepts described. Micrometeorological methods measure the rate of transfer above a surface to determine the flux to the surface (Equation 1.24). This is true only under certain conditions. First, horizontal homogeneity is required in order to consider flux measurements representative of the area being sampled. Second, the ergodic hypothesis was employed in order to use time averages of measurements in the place of ensemble averages. This implies horizontal homogeneity and further requires that the turbulence is stationary. The steady state assumption was used to arrive at Equation 1.24. Measurement conditions, such as measurement height, fetch size, and sampling frequencies follow from these assumptions. Further, data analysis procedures are related to the sampling conditions and are constrained by the measurement methods.

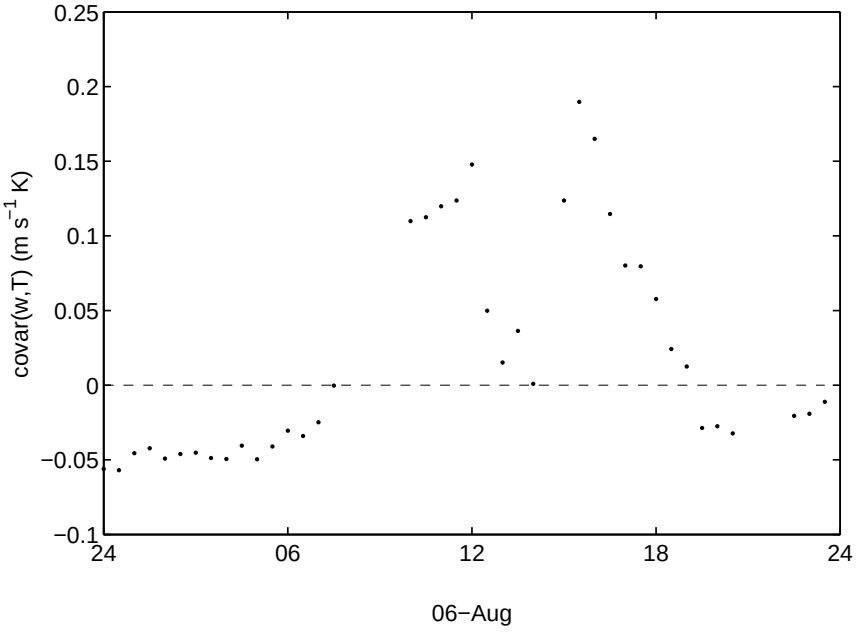

Figure 1.16: Covariance of the vertical wind velocity, w, and the sonic temperature, T, over 30-min averaging periods on 6 August 2001. The covariance can be scaled to determine the sensible heat flux over the averaging period, where positive covariances correspond to upward heat fluxes and negative covariances to downward heat fluxes.

1.5.1. *Validity of Eddy Correlation Method and Assumptions*

1.5.1.1. *Spectral and Cospectral Analysis*

Turbulent flow can be conceptualized as the superposition of eddies over a wide range of sizes (Kaimal and Finnigan, 1994). These eddies interact with each other and with the mean wind flow, continuously combining and transferring energy. The largest eddies are produced from instabilities in the mean flow due to buoyancy and shear forces. These eddies break up into smaller eddies because their interactions create instabilities. This mechanism continues, transferring energy down to the smallest size eddies, in the process known as the energy cascade, until the energy is converted to heat by viscosity (Stull, 1988).

The Fourier spectra and cospectra can used to associate eddies of each size scale with a corresponding energy scale (Kaimal and Finnigan, 1994). The Fast Fourier Transform (FFT) is commonly used to calculate the spectra and cospectra of turbulent data as a function of the frequency, f, of the turbulence. The energy spectrum peaks in the energy-containing range at approximately 0.01 Hz $< f <$ 1 Hz, where production of turbulent energy by buoyancy and shear occurs. At lower frequencies eddies interact and transfer energy by inertia with no net loss since the production of energy by larger eddies is dissipated at an equal rate to smaller eddies. This is known as the inertial subrange at approximately 1 Hz $< f <$ 10 Hz. At the smallest eddy scale, kinetic energy is converted to internal energy by viscosity. This low energy spectrum region is called the dissipation range at approximately $f >$ 10 Hz.

Spectral analysis can be used to verify the frequency response of instruments used for fast response measurements. Instruments must measure turbulent fluctuations at frequencies that make a significant contribution to turbulent transport. Experimental and theoretical research suggests that the inertial subrange of the power spectrum of wind velocity should obey the -5/3 power law (Kaimal *et al.*, 1972). This form of the inertial subrange holds for the temperature spectra as well and appears to be valid for other scalars (Kaimal and Finnigan, 1994).

Cospectral analysis can also be used to confirm the frequency response of the eddy

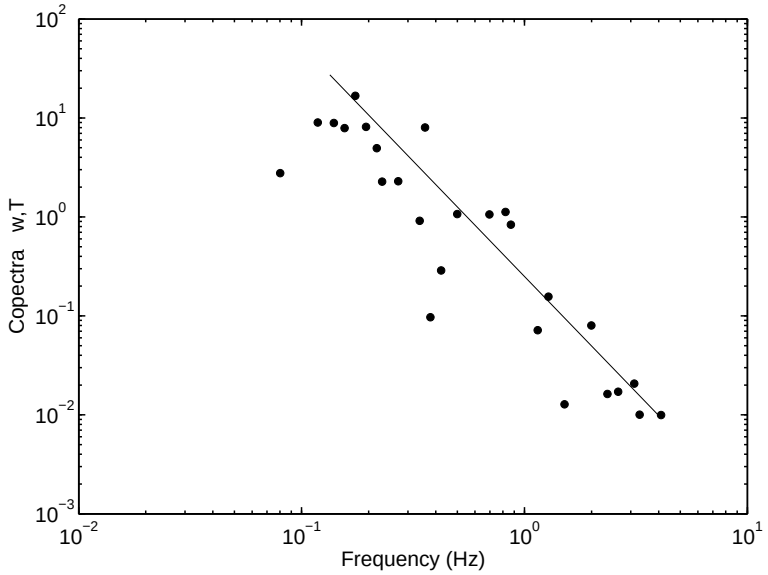

Figure 1.17: Cospectrum of vertical wind velocity, w, with sonic temperature, T, for 12:00-12:30 on 4 August 2001. The line is the -7/3 power slope of the spectra expected for $f > 2\overline{u}/z$.

correlation instruments. Kaimal *et al.* (1972) developed cospectral curves that can be used as guides for establishing sampling frequencies. The cospectrum of momentum falls off in the inertial subrange as $n^{-7/3}$, where n is the natural frequency. The cospectrum for sensible heat flux obeys the same -7/3 power law (see Figure 1.17) and available evidence suggests that the cospectrum for other scalars exhibit the same shape and characteristics as the heat flux (Kaimal and Finnigan, 1994).

For valid flux calculations, measurements of the scalar of interest must be made for the same air parcel as the wind measurements (Businger, 1986; Kaimal and Finnigan, 1994; Wesely and Hicks, 2000). Many instruments used to measure turbulent atmosphere-surface fluxes cannot be mounted at the same location as wind velocity measurements; for example the instrument may not be weatherproof, it may be too large for installation on a tower, it may require frequent maintenance and calibration, or it may cause distortions of the air flow. Therefore atmospheric samples are commonly drawn through a sampling line to a concentration sensor located at the base of the tower. Concentration fluctuations are attenuated between the sampling line and instrument inlets as a result of differential axial velocities and

radial transport. This attenuation leads to uncertainty in the estimated flux since measurement of fluctuations that contribute to the turbulent flux may be underestimated. Predictions for dispersion in laminar flows (Taylor, 1953) have been used to estimate attenuation of fluctuations in sampling lines (Philip, 1963a,b,c; Lenschow and Raupach, 1991). Sampling lines must be designed to reduce concentration fluctuation attenuation for valid eddy correlation measurements.

1.5.1.2. *Site and Sampling Characteristics*

Fluxes measured above the surface are the same as the bulk surface only if the flux is constant with height. Changes in the flux with height are possible when obstructions exist in the upwind sampled area (fetch), the surface is nonuniform in roughness due to vegetation or terrain, or the sampled species is transformed, for example by chemical reaction, within the fetch (Wesely and Hicks, 2000). For aerosol particles, gas-particle conversion and water uptake can also change the flux by modifying the particle size (Gallagher *et al.*, 1997; Vong *et al.*, 2004). Thus, the site must be horizontally homogeneous, meaning none of these processes change the flux with height.

Wesely and Hicks (2000), Businger (1986), and others suggest a homogeneous upwind fetch of 100-200 times the measurement height for the constant flux layer to develop sufficiently to assume horizontal homogeneity. Empirical results guide the recommendations for fetch requirements and effects of nonhomogeneous conditions are often manifested as nonstationary measurements (discussed below) in data analysis (Foken and Wichura, 1996). Under homogeneous conditions, the flux can be considered homogeneous and measurements made within the constant flux layer are considered representative of the surface-atmosphere exchange.

The ergodic hypothesis assumes that the time average is equal to the ensemble average. The ergodic hypothesis employed is only valid if the turbulence is horizontally homogeneous and stationary (Kaimal and Finnigan, 1994). Horizontal homogeneity means that the statistical properties of the flow are independent of horizontal position, varying only with height and

time. A horizontally homogeneous fetch usually corresponds to homogeneous turbulence since nonhomogeneous conditions can be caused by obstructions in the flow or nonuniform roughness.

Turbulence can also change over time due to changes in the wind direction, time of day, synoptic weather conditions, or the measurement point itself, causing nonstationary conditions. Tests for stationary conditions are often implemented in post processing of collected data. Variances and covariances of statistically stationary time series, $c(t)$, approach stable values as the averaging time, t_0, increases. Selection of the appropriate averaging time will be discussed below. Foken and Wichura (1996) suggest that measurements are considered stationary if there is less than 30% difference between the eddy covariance ($\overline{w'c'}$) over the averaging period and the mean of eddy covariances calculated over 4-8 intervals of about 5 minutes within the averaging period.

1.5.1.3. *Averaging Time for Flux Measurement*

The steady state assumption means that changes in mean turbulent measurements over time can be ignored. The validity of this assumption is based on the time scale considered. The time scale must be long enough to average rapid, small scale fluctuations but short enough that the mean of turbulent quantities do not change with time.

For a simple average, $\overline{c}$, the averaging time required to determine the mean, $\overline{c}$, with an accuracy ϵ is

$$t_0 = \frac{2t_i\overline{c'^2}}{\epsilon^2\overline{c}^2} \tag{1.29}$$

where t_i is the integral time scale and $\overline{c'^2}$ is the variance of c. The integral time scale can be estimated as the time it takes for the dominant eddy of size l to pass over the measurement point

$$t_i \approx l/\overline{u} \tag{1.30}$$

For daytime conditions, $l \approx 10z$ is typical (Businger, 1986) where z is the height of the measurement point above the canopy, resulting in $t_i = 10$ s for $z = 5$ m and $\overline{u} = 5$ m s^{-1}. Thus, for

typical daytime values of $\overline{c'^2}/\overline{c}^2 = 0.01$ and specifying $\epsilon = 0.01$, the estimated averaging time is $t_0 = 2000$ s, or approximately 33 min. This averaging time corresponds to the passage of two or three large convective cells that extend through the convective boundary layer (Kaimal and Finnigan, 1994).

The averaging period for eddy correlation calculations can also be determined using an ogive function (Oncley *et al.*, 1990; Foken and Wichura, 1996). The ogive function is defined as the cumulative integral of the cospectrum (e.g., $\overline{u'w'}$ for the momentum flux) from the highest frequencies to the lowest frequency, f_0, contributing to the integral

$$Og_{uw} = \int_{\infty}^{f_0} Co_{\overline{u'w'}}(f)\,\mathrm{d}f \tag{1.31}$$

This function converges to a constant value at a frequency which can be converted to an averaging period for flux measurements. Deviations up to 10% of the total are tolerated due to the variability of turbulent spectra. For micrometeorological scalar fluxes, averaging times of $t_0 = 20$–30 min are common using the ogive test (Foken and Wichura, 1996), in agreement with the method above. Momentum flux ogives were calculated for 2 h time periods on 6 August 2001, during the PROPHET 2001 field experiment (see Figure 1.18). The ogives approach a stable value at $f = 5.6 \times 10^{-4}$ Hz for all time periods, corresponding to an averaging time of $t_0 = 30$ min.

1.5.2. *Measurement and Site Requirements*

For eddy correlation measurements, the instrument response must be fast enough to cover the bandwidth of atmospheric fluctuations that make a significant contribution to the flux. Cospectra for sensible heat, water vapor, and CO_2 fluxes can be used to determine the cutoff frequency for the exchange of these scalars. Wesely and Hicks (1977) suggest that the bandwidth requirement is $10^{-3} \leq nz/\overline{u} \leq 10$, where n is the sampling frequency, $\overline{u}$ is the mean wind speed, and z is the height above the surface.

More recent data show that the cospectra of the turbulent fluxes peak at the nondimensional frequency $f = 0.03$, where $f = nz/\overline{u}$ (Businger, 1986). The cospectral energy decreases on both sides of the peak, from which the measurement bandwidth can be selected. Businger

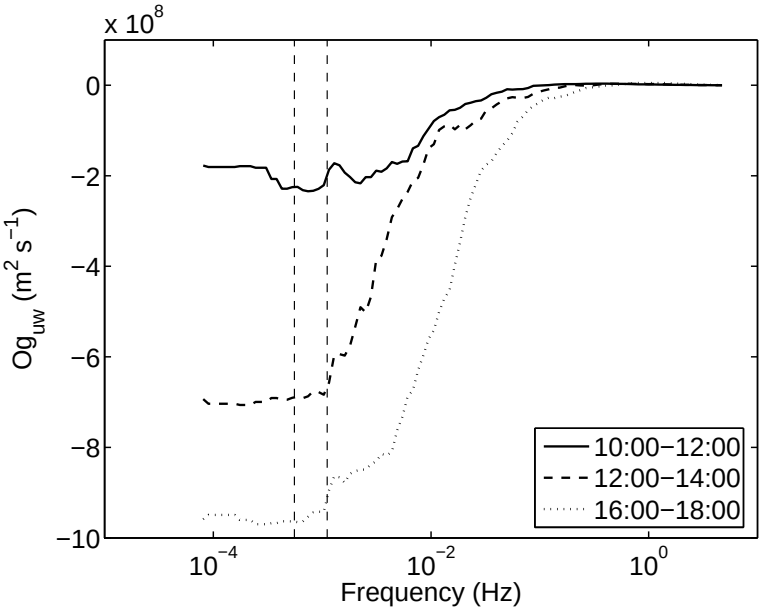

Figure 1.18: Momentum flux ogives on 4 August 2001. The vertical dashed lines at $f = 1.1 \times 10^{-3}$ and $f = 5.6 \times 10^{-4}$ Hz correspond to averaging periods of 15 and 30 minutes, respectively.

(1986) defined the range based on the -10 dB point (one-tenth below the peak value), resulting in $f = 0.001$ on the low frequency side and $f = 1.5$ and 3 for momentum and heat fluxes, respectively, on the high frequency side. The high frequency cutoff most commonly used is about $n = 2\overline{u}/z$, resulting in a minimum sampling frequency of 2 Hz for $\overline{u} = 5$ m s^{-1} and $z = 5$ m (Wesely and Hicks, 2000).

The measurement height for micrometeorological methods is dictated by the local terrain and the frequency response of the instruments. Sensors should be high enough so that instruments are not affected by individual roughness elements. Assuming a sufficiently homogeneous fetch to satisfy this condition, sensors must resolve $f = 3$ Hz corresponding to wavelengths as small as $z/3$. The spatial resolution should be smaller by a factor of 2π to avoid attenuation (loss) of the signal due to averaging (Businger, 1986). The minimum height can then be estimated as

$$z_{\min} = 6\pi d \tag{1.32}$$

where d is the spatial resolution of the instrument. Because the fetch size increases with height, the maximum height is constrained by the available homogeneous fetch. For an upwind fetch of 1 km in the direction of the dominant wind, the maximum measurement height, z_{max}, is about 10 m, which is low enough to be representative of the area being sampled (Businger, 1986).

1.5.3. *Instrumentation*

The variables of interest for flux measurements are wind speed, temperature, humidity, and species concentrations. Given sufficiently fast-response measurements, eddy fluxes can be calculated from the covariances (see Section 1.4). Although a large variety of sensors exist for atmospheric measurements, this discussion focuses on the most common instruments used for in situ eddy flux measurements.

Air velocity can be measured using a three-dimensional anemometer, such as a sonic anemometer. The operating principle of sonic anemometers is the accurate measurement of the speed of sound in air between two ultrasonic transducers. The transit time of an acoustic pulse between the two points is affected by the velocity of the air between them. With a fixed separation between the two points, d, and the measured transit time of two opposing pulses, t_1 and t_2, the velocity of the air is calculated as

$$v_{air} = \frac{d}{2}\left(\frac{1}{t_1} - \frac{1}{t_2}\right) \tag{1.33}$$

An array of opposing transducers facilitates measurement of three orthogonal axes (u, v, and w).

Temperature can also be measured using a sonic anemometer since the speed of sound in an ideal gas is

$$C_{air} = \left(\frac{\gamma RT}{M}\right)^{\frac{1}{2}}\left(1 + 0.32\frac{e}{p}\right) \tag{1.34}$$

where e is the water vapor pressure. The term, $(1 + 0.32e/p)$, represents the effect of humidity on the measured sonic temperature. This closely resembles the virtual temperature correction, $(1 + R/R_v\ q) \approx (1 + (R/R_v)^2 e/p)$, from Equation 1.5. The contribution e/p is small and usu-

ally neglected (Kaimal and Finnigan, 1994). Then the speed of sound in air is calculated from the average transit times of the acoustic pulses, and the sonic temperature

$$T = \left(\frac{\gamma R}{M}\right)^{-1} C_{\text{air}}^2 \tag{1.35}$$

estimates the virtual temperature, T_v, to ± 0.01 °C (Kaimal and Gaynor, 1991). In the surface layer $\theta_v \approx T_v$ and the sonic temperature can be used to estimate sensible heat fluxes.

Two techniques are commonly used for humidity measurements: ultraviolet absorption and infrared absorption (Kaimal and Finnigan, 1994). Ultraviolet hygrometers use an excited hydrogen source to produce ultraviolet radiation. Water vapor between the source and detector absorbs the UV emission proportional to concentration. Infrared hygrometers detect humidity through differential measurement of infrared transmittance at two wavelengths of high water vapor absorption and low water vapor absorption. Water vapor in the measurement path absorbs the infrared emission in proportion to the concentration.

Infrared absorption by trace gases occurs at different wavelengths than water vapor. This has led to the development of instruments capable of measuring CO_2 or CH_4 simultaneously with water vapor (Kaimal and Finnigan, 1994). Sensors for ozone, nitrogen dioxide, and other trace gases have also been developed using a variety of techniques. Improvement of trace gas flux estimates depends on advancements in trace gas sensor technologies suitable for eddy flux measurements (Wesely and Hicks, 2000).

Similarly, particle measurements are limited to techniques capable of fast-response measurements. Optical particle counters have been used extensively to estimate fluxes of particles as a function of size (Gallagher *et al.*, 1997; Vong *et al.*, 2004). Wesely *et al.* (1985) designed a flame photometric detector method to measure particulate sulfur concentrations for eddy flux measurements. Further details about particle flux measurements will be presented in the next section.

1.6. Particle Dry Deposition

Dry deposition is the transport of particles from the atmosphere to the surface in the absence of precipitation. The physical and chemical processes involved generally fall into three

categories that affect the overall transport process. A particle in the atmospheric surface layer, but away from the surface, will be transported vertically by turbulent mixing and gravitational settling. As it is transported closer to the surface, the effects of Brownian diffusion and inertial impaction are comparable to the diminishing effect of turbulent mixing. Eventually particles are transported close enough to the surface to adhere.

1.6.1. *Particle Transport in the Atmospheric Boundary Layer*

A mathematical description of the physical processes involved in particle transport is needed. From Equation 1.24 the dry deposition flux of a species is

$$F = \overline{w'c'} \tag{1.36}$$

and F is proportional to c (Equation 1.1). Combining Equations 1.36 and 1.1, the turbulent deposition velocity is defined as the normalized flux (Chamberlain, 1966), calculated as

$$v_d = -\frac{\overline{w'c'}}{c} \tag{1.37}$$

The deposition velocity, v_d, has units of length per time, and is positive for a downward flux ($F < 0$). This formulation is useful because all of the complexities of the turbulent dry deposition process are contained in a single parameter, analogous to a mass transfer coefficient.

An electrical resistance-in-series analogy lends itself well to the dry deposition process where the steps are modeled as three resistances in series: an aerodynamic resistance, r_a, a surface boundary layer resistance, r_b, and a canopy resistance, r_c (see Figure 1.19). The total resistance, r_t, is the sum of the individual resistances and is the inverse of the deposition velocity

$$v_d^{-1} = r_t = r_a + r_b + r_c \tag{1.38}$$

It is usually assumed that all particles adhere to the surface, so that the canopy resistance r_c = 0. The settling velocity is taken into account by including it in parallel with the resistances

$$v_d = \frac{1}{r_t} = \frac{1}{r_a + r_b + r_a r_b v_s} + v_s \tag{1.39}$$

where v_s is the settling velocity. Particles with diameter greater than a few microns have

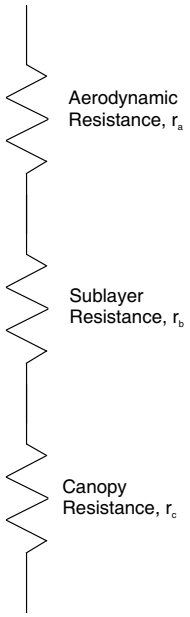

Figure 1.19: Electrical resistance-in-series analogy for dry deposition processes. Dry deposition is composed of a series of three steps: aerodynamic transport, boundary layer transport, and surface interaction, each with an analogous resistance. The inverse of the sum of the resistances is the deposition velocity.

significant settling velocities, calculated using Stokes Law

$$v_s = \frac{\rho_p D_p^2 g C_c}{18\mu} \tag{1.40}$$

where ρ_p is the particle density, g is the gravitational acceleration, μ is the viscosity of air and C_c is the slip correction factor

$$C_c = 1 + \frac{2\lambda}{D_p}\left[1.257 + 0.4\exp\left(-\frac{1.1 D_p}{2\lambda}\right)\right] \tag{1.41}$$

where λ is the mean free path of air molecules. Using this conceptualization of the dry deposition process, the individual steps can be described mathematically.

Aerodynamic transport carries particles from the boundary layer to the surface sublayer. This occurs by eddy diffusion and sedimentation, which vary in magnitude for different sized particles. Turbulent eddies move particles from areas of high concentration to areas of low concentration. The surface acts as a sink, removing particles from the atmosphere.

The aerodynamic component of the dry deposition process is based on gradient-transport

theory and mass/momentum or mass/heat transport similarity. Turbulent momentum transport is expressed in terms of a turbulent momentum diffusivity, K_M, multiplied by a vertical gradient

$$F_M = -K_M \frac{d}{dz}(\rho_{\text{air}} u) \tag{1.42}$$

where F_M is the flux of air momentum and the product, $\rho_{\text{air}} u$, is essentially the concentration of air momentum. Similarly,

$$F_T = -K_T \frac{d}{dz}(\rho_{\text{air}} \hat{c}_{\text{p,air}} T) \tag{1.43}$$

where F_T is the flux of sensible heat and K_T is the eddy heat diffusivity. The eddy diffusivities, found from dimensional analysis and micrometeorological measurements, can be expressed as (Seinfeld and Pandis, 1998)

$$K_M = \frac{k u_* z}{\phi_M(\zeta)} \tag{1.44}$$

and

$$K_T = \frac{k u_* z}{\phi_T(\zeta)} \tag{1.45}$$

where $\phi_M(\zeta)$ and $\phi_T(\zeta)$ are empirically determined functions of the stability (Equation 1.12) that represent the height dependence of mean velocity and temperature and their gradients. It is presumed that turbulent transport of particles occurs by mechanisms similar to those for momentum and heat. Thus, mass transport can be calculated using the diffusivities and scaling parameters.

The general form of the gradient turbulent transport

$$F_a = K \frac{dC}{dz} \tag{1.46}$$

can be integrated from the surface to the height of the constant flux surface layer

$$F_a = (C_3 - C_2) \left(\int_{z_2}^{z_3} \frac{\phi(\zeta)}{k u_* z} dz \right)^{-1} \tag{1.47}$$

where C_3 and C_2 are the concentrations at the top and bottom of the constant flux layer respectively and $\phi(\zeta)$ is the function for momentum or heat transport. The integral term in Equation 1.47 is now a stability-dependent diffusivity analogous to the vertical conductance of

particles. The aerodynamic resistance for Equation 1.39 is then the inverse of this term

$$r_a = \int_{z_2}^{z_3} \frac{\phi(\zeta)}{k u_* z} dz \tag{1.48}$$

Explicit expressions for $\phi(\zeta)$ are available, such as that of Businger *et al.* (1971)

$$\phi(\zeta) = \begin{cases} 1 + 4.7\zeta & \zeta > 0 \quad \text{stable} \\ 1 & \zeta = 0 \quad \text{neutral} \\ (1 - 15\zeta)^{-1/4} & \zeta < 0 \quad \text{unstable} \end{cases} \tag{1.49}$$

This is applicable only in the constant flux layer where the Brownian diffusivity is orders of magnitude smaller than the eddy diffusivity.

Particles are then transported across the surface boundary layer (sometimes referred to as the quasi-laminar layer or simply the surface layer) by diffusion, interception, inertial impaction, and sedimentation (Figure 1.6). The flux across the surface layer is

$$F_b = B u_* (C_2 - C_1) \tag{1.50}$$

where B is a transfer coefficient and C_2 and C_1 are the concentrations at the top of the surface layer and at the surface respectively and the transfer coefficient is scaled by u_*. The surface layer resistance is the inverse of the transfer coefficient

$$r_b = \frac{1}{B u_*} \tag{1.51}$$

The transfer coefficient must account for the effects of diffusion, interception, and inertial impaction. Electrostatic forces, thermophoresis, and diffusiophoresis may also contribute to deposition, but the magnitude is small compared to other mechanisms (Davidson and Wu, 1990).

Brownian motion transports particles based on the thermal energy of particles and the surrounding air. These processes are especially important for small particles that are not subject to inertial forces large enough to cause impaction (Davidson and Wu, 1990). Particle Brownian diffusivity is

$$\mathcal{D} = \frac{kTC_c}{3\pi\mu D_p} \tag{1.52}$$

As particle size decreases the diffusivity increases and resistance to transport is low. For particles larger than about 1 μm, particle inertia limits the ability of the particle to follow

changes in the direction of airflow. Thus, there is an increase in the surface layer resistance for particles in the range 0.1 μm to 1 μm. A minimum in the overall deposition velocity is evident in this size range from these size dependent effects.

The effect of diffusion on the surface layer resistance can be incorporated using the Schmidt number

$$\mathrm{Sc} = \frac{\nu}{\mathcal{D}} \tag{1.53}$$

where ν is the kinematic viscosity of air. The Schmidt number is a dimensionless number that accounts for the competing effects of momentum and diffusion transport.

Inertial impaction is also important for particles larger than 100 nm. When an object protrudes into the mean airflow, particles cannot follow the rapid change in direction of the airflow and their inertia carries them across the sublayer. Turbulent inertial deposition can also take place, where the inertial energy is derived from turbulent eddies near the surface providing sufficient energy to cross the surface layer (Davidson and Wu, 1990). Inertial impaction is parameterized using the Stokes number

$$\mathrm{St} = \frac{v_s u_*^2}{g\nu} \tag{1.54}$$

where v_s is given by Stokes Law (Equation 1.40).

Interception is included in the surface layer resistance for specific surfaces using measurements of the characteristic size of the surface elements. For example, the leaves, plant stalks, and tree needles can be measured to determine a characteristic size and the interception efficiency is

$$E_{IN} = \frac{1}{2}\left(\frac{D_p}{A}\right)^2 \tag{1.55}$$

where A is the characteristic radius of the collection surface (Slinn, 1982).

Various empirical formulas for the surface layer resistance equation have been offered with the general form

$$r_b = \frac{1}{f(u_*)(\mathrm{Sc}^{-n} + 10^{-m/\mathrm{St}})} \tag{1.56}$$

where $f(u_*)$ is some function of the friction velocity, and the constants, n and m, have been

empirically determined to include the surface layer deposition mechanisms described above, as will be discussed in the following sections.

The last step in the deposition process is interaction with the surface. While the removal of gases at the surface depends on the gas species and surface properties, particles are assumed to adhere to the surface (Davidson and Wu, 1990; Wesely and Hicks, 2000). Particle bounce off and resuspension are generally considered negligible for all particles and the canopy resistance, $r_c = 0$.

1.6.2. *Wind Tunnel Studies*

Early studies of particle deposition used wind tunnels, where known quantities of particles were released inside a wind tunnel, the floor of which was covered with real or artificial deposition surfaces (Chamberlain, 1966, 1967). Wind speed, friction velocity, and surface roughness were measured or estimated and used to parameterize particle deposition. For particles larger than about 1 μm, sedimentation was the dominant deposition mechanism. For particles in the size range 0.1 to 1 μm, particle deposition decreased due to the magnitude of surface layer transport. For particles smaller than about 0.1 μm, particle deposition increased due to Brownian diffusion.

Sehmel and Hodgson (1978) divided dry deposition into the three step process (see Figure 1.19) in order to develop a mechanistic model. Deposition velocities were measured for a broad range of particle sizes over surfaces with friction velocities in the range 0.1–1.5 m s^{-1}. The data were used to produce empirical relationships for the deposition velocity as a function of particle diameter, friction velocity, surface roughness, particle density, and atmospheric stability.

The results of wind tunnel studies were useful in determining the parameters that influence deposition velocity and providing direct measurements of deposition velocities. The application of the empirical results from wind tunnel studies to field conditions is based on assumptions that the wind tunnel surface roughness and the frequency scale of the turbulence generated above the wind tunnel floor represents that of real surfaces. The vertical concen-

tration profile above the wind tunnel floor is also assumed to represent that above a soil or vegetative canopy surface.

1.6.3. *Semiempirical Models*

Semiempirical relationships that incorporate micrometeorological and surface properties have been used to develop mechanistic deposition velocity models using Equation 1.39 (Slinn, 1982). The aerodynamic resistance was derived from the similarity of scalar fluxes in the atmospheric boundary layer and is calculated as

$$r_a = \frac{\ln(z/z_o) - \Psi_H}{k u_*} \tag{1.57}$$

where z_o is the aerodynamic roughness length and Ψ_H is the stability function. The aerodynamic roughness length is defined as the height above the surface at which the wind speed, U, vanishes (Kaimal and Finnigan, 1994). Under near-neutral stability ($|L| > 1000$ m), z_o for a given surface can be estimated from measurements of U and u_*. The stability function can be estimated from measurements of L (see Section 1.3.3).

Slinn (1982) used the wind tunnel data of Chamberlain (1966) to develop a semiempirical expression for the surface resistance of vegetative canopies

$$r_b = \frac{1}{u_*(\mathrm{Sc}^{-2/3} + 10^{-3/\mathrm{St}})} \tag{1.58}$$

Particle v_d as a function of particle size was then modeled for varying wind speed and canopy conditions. The roughness, turbulence, and plant surface properties of the vegetative canopy were characterized by an empirical constant, γ_s, with a value of ≈ 3 (Slinn, 1982). For low wind speeds, $U = 1$ m s^{-1}, this model predicted v_d in the ranges 0.1–1 cm s^{-1} for $D_p < 0.01$ μm, 0.005–0.5 cm s^{-1} for $D_p = 0.01$–10 μm, and 1–10 cm s^{-1} for $D_p > 10$ μm, with a minimum at $D_p \approx 0.2$ μm (see Figure 1.20). The v_d values increase by approximately one order of magnitude for an order of magnitude increase in U.

This framework has been used to develop regional scale air pollution models (Binkowski and Shankar, 1995; Binkowski, 1999; Zhang *et al.*, 2001). The model of Zhang *et al.* (2001) includes parameterization of particle v_d for several land-use categories (LUC) and seasonal

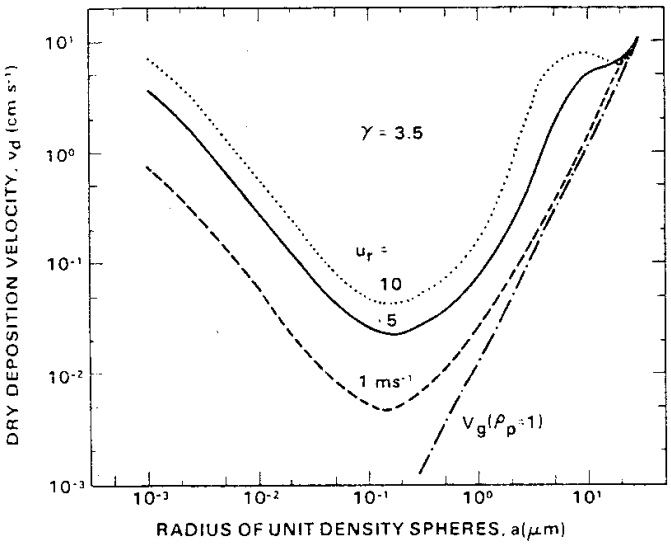

Figure 1.20: Predicted deposition velocities from a semiempirical model (Slinn, 1982). The model results show the particle size dependence of the deposition velocity to a Eucalyptus forest. Deposition also increases with increasing wind speed.

categories (SC) to represent the range of conditions necessary for a large spatial and temporal scale model. The aerodynamic resistance is calculated using Equation 1.57 by estimating Ψ_H from measurements of L.

The surface layer resistance is parameterized as

$$r_b = \frac{1}{u_* \left(E_B + E_{IM} + E_{IN}\right) R_1 \varepsilon_0} \tag{1.59}$$

where E_B, E_{IM}, and E_{IN} are collection efficiencies for Brownian diffusion, impaction, and interception, respectively; R_1 is the fraction of particles that stick to the surface without rebound; and ε_0 is an empirical constant with a value of 3 commonly used (Zhang *et al.*, 2001).

The diffusion collection efficiency has the form

$$E_B = \mathrm{Sc}^{-\gamma_s} \tag{1.60}$$

where $\mathrm{Sc} = \nu/\mathcal{D}$ is the particle Schmidt number, ν is the kinematic viscosity of air, $\mathcal{D}$ is the particle diffusivity, and γ_s is an empirical constant which varies with surface type. Slinn (1982) found $\gamma_s = 2/3$ for vegetated surfaces. Values of γ_s have been tabulated for different LUC

(Zhang *et al.*, 2001).

Several functional forms have been proposed for the impaction collection efficiency. Zhang *et al.* (2001) use the widely accepted form

$$E_{IM} = \left(\frac{\mathrm{St}}{\alpha + \mathrm{St}}\right)^{\beta} \tag{1.61}$$

where $\mathrm{St} = v_s u_*^2 / g\nu$ is the particle Stokes number, and α and β are empirical constants with values tabulated for different LUC.

From Equation 1.55, the interception collection efficiency is

$$E_{IN} = \frac{1}{2}\left(\frac{D_p}{A}\right)^2 \tag{1.62}$$

Estimates of A for "large" collectors (e.g. stalks, needles, etc.) and "small" collectors (e.g. vegetative hairs) have been tabulated for different LUC (Zhang *et al.*, 2001).

Particle rebound is possible for $D_p > 5$ μm, but theoretical and experimental predictions remain uncertain. Slinn (1982) and others suggest the fraction of particles that stick to the surface is

$$R_1 = \exp(-b\ \mathrm{St}^{1/2}) \tag{1.63}$$

where b is an empirical constant, often assumed to be 1 (Giorgi, 1988; Zhang *et al.*, 2001).

1.6.4. *Measurement Methods*

1.6.4.1. *Bulk Collection Methods*

Surface analysis methods quantify deposition fluxes by collecting materials that deposit on a surface. Surrogate surfaces, such as filter substrates, petri dishes, and buckets, have been widely used because they are inexpensive and easy to use. The flux over the exposure period is determined by washing the surface and analyzing the extract. Surrogate surfaces may not be representative of natural surfaces of interest (Wesely and Hicks, 2000). Natural surface analysis methods have been used to avoid this problem. Leaf washing, snow analysis, and throughfall collection are examples of methods that estimate fluxes from collection of deposited material on natural surfaces (Ammann *et al.*, 1995; Lovett and Lindberg, 1984). Extrapolations of these measurements to canopy scales is difficult because interactions

of deposited materials with the surfaces, such as absorption, are likely over the relatively long time scales (weeks to months) required to collect quantifiable amounts of material. Gas and particle deposition are indistinguishable from surface analysis methods.

1.6.4.2. *Indirect Methods*

The dry deposition flux can be inferred from measurement of the atmospheric concentration and calculated deposition velocity (Baldocchi *et al.*, 1988; Lovett, 1994). This method is known as the inferential method. Measurement techniques depend on the substance of interest; for most species, integrative measurements over 24 hours are necessary for quantification. Deposition velocities are modeled based on meteorological measurements and surface characteristics (see Section 1.6.3). This method is well suited for species that are routinely monitored. The validity of the fluxes depends on the accuracy and the temporal resolution of the meteorological measurements used to estimate average deposition velocities.

The gradient method estimates the flux using gradient transport theory, Equation 1.46, to calculate the deposition velocity (Lorenz and Murphy, 1989)

$$v_d = \frac{k u_* z}{\phi} \frac{1}{\overline{c}} \frac{\partial \overline{c}}{\partial z} \tag{1.64}$$

where $\overline{c}$ is the mean concentration measured at two (or more) vertically separated points and $\partial \overline{c}/\partial z$ is the vertical gradient approximated by $\Delta \overline{c}/\Delta z$. This method requires very accurate relative concentration measurements at multiple measurement points. The measured differences depend on the vertical separation since relative differences can be very small for small separations. Areas of low concentration may have small differences even at larger separation distances. The eddy diffusivity term must also be derived, usually from mass-momentum similarity theory, to estimate the deposition velocity. Although this method is theoretically simple, it may be impractical in many situations due to measurement limitations or insufficient homogeneity of sites (Wesely and Hicks, 2000).

1.6.4.3. *Direct Methods*

Direct micrometeorological methods involve measurements in the air above the deposition surface, such that spatial variability caused by the canopy do not affect deposition

measurements. These techniques have strict homogeneity requirements in order to determine fluxes from turbulent measurements. Micrometeorological methods are considered to be the best available for the species and sites for which the technique is applicable (Wesely and Hicks, 2000). Eddy accumulation, relaxed eddy accumulation, and eddy correlation are micrometeorological methods developed for atmospheric flux measurements.

In the eddy accumulation method, the difference in concentration between upward moving air and downward moving air is used to estimate the flux (Wesely and Hicks, 2000). Samples are collected on two vertically separated filters or containers. When the wind velocity is directed upwards, only the upper sampler operates; when the wind is downwards, only the lower sampler operates. Commonly, a fast response anemometer controls a valve to determine which sampler is turned on and the sampling flow rate is proportional to the magnitude of the vertical velocity (Baldocchi *et al.*, 1988). The flux is then calculated as the difference in concentrations between the two samplers

$$F = \beta \sigma_w \left(\overline{C}^+ - \overline{C}^- \right) \tag{1.65}$$

where β is an empirical constant with a parameterized value of 0.6, σ_w is the standard deviation of the vertical wind velocity, and $\overline{C}^+$ and $\overline{C}^-$ are the average concentrations in the $w > 0$ and $w < 0$ accumulated samples (Businger and Oncley, 1990). Similar to the gradient technique, accurate concentration measurements are required, especially for small concentration differences. Temporal resolution of the measurements also limit generalization of these results. Nevertheless, eddy accumulation is an attractive alternative when fast response sensors are not available for the species of interest.

Businger and Oncley (1990) proposed the relaxed eddy accumulation (REA) method, a more easily implemented eddy accumulation method, in which samples are collected at a constant flow rate for the upward and downward eddies. This method is otherwise identical to eddy accumulation, employing Equation 1.65 and retaining the limitations described above. The REA method has been tested and implemented for several gas species and in a few cases for particle deposition measurements (Wesely and Hicks, 2000; Schery *et al.*, 1998). For exam-

ple Schery *et al.* (1998) estimated particle deposition velocities for ultrafine particles ($\approx$ 1 nm in diameter) by using radioactive aerosol particles formed from the nucleation of gas phase radon and its decay products.

The eddy correlation method has been used extensively to measure particle dry deposition (Wesely *et al.*, 1977; Sievering, 1982; Wesely *et al.*, 1983, 1985; Gallagher *et al.*, 1997, 2002; Vong *et al.*, 2004). As described in Section 1.4, eddy correlation utilizes fast response measurements of surface layer wind velocities and scalar concentrations that can then be used to directly calculate the turbulent flux. Eddy correlation is considered the most reliable and direct measurement method to determine eddy fluxes (Businger, 1986; Wesely and Hicks, 2000). Thus, eddy correlation is the method commonly used to generalize flux measurements by direct measurement of v_d to evaluate and improve dry deposition models. The major limitation of this method is the availability of fast response detectors for the species of interest (Wesely and Hicks, 2000).

Wesely *et al.* (1977) used a particle charger to measure nonspeciated, small particle (D_p = 0.05–0.1 μm) deposition velocities of 0.12–1.2 cm s^{-1}. Wesely *et al.* (1983) and Wesely *et al.* (1985) measured particulate sulfur dry deposition velocities using a flame photometric detector (FPD). Average daily deposition velocities of 0.22 $\pm$ 0.06 cm s^{-1} were reported for particles in the size range 0.01 to 2 μm, with large run-to-run variability, attributed to noise in the FPD signal (Wesely *et al.*, 1985).

Wesely *et al.* (1985) evaluated the effect of stability on deposition velocity. Windy conditions resulted in increased deposition velocities. First, parameterization of v_d by u_*, which increases with wind speed and influences diffusion, impaction, and interception, produced the dimensionless variable v_d/u_*. This formulation was not sufficient to explain the variability in deposition velocity. The ratio v_d/u_* was shown to be independent of u_*, since variations in u_* alone do not correlate with increases in v_d/u_*. Segregation of v_d/u_* for different stability conditions showed an apparent correlation, with higher values associated with unstable conditions. Thus, a plot of v_d/u_* as a function of the inverse of the Obukhov length, L^{-1}, resulted

in low values under stable and neutral conditions and increasing values as an exponential function of L^{-1}.

Optical particle counters (OPCs) have been used to measure size-resolved particle v_d by eddy correlation (Sievering, 1982; Katen and Hubbe, 1985; Gallagher *et al.*, 1997; Buzorius *et al.*, 1998; Gallagher *et al.*, 2002; Vong *et al.*, 2004). In this method, sampled air is passed through a continuous wave laser. Particle size is determined from the amount of light scattered by calibration particles, usually polystyrene latex spheres. Since ambient aerosol particles are optically different from calibration particles, particle sizes determined from OPCs are approximate (Hering and McMurry, 1991). Particle size is also affected by water uptake at varying ambient humidity.

Measurements of v_d over short vegetation (z_o < 0.2 m) vary over an order of magnitude. Wesely *et al.* (1985) measured mean daily sulfate v_d over grass with z_o = 0.04 m in the range 0.05–0.21 cm s^{-1} for bulk aerosols with no size discrimination. Size-segregated measurements have resulted in $v_d \approx 0.07$ cm s^{-1} for D_p = 0.1–0.2 μm over heathland with z_o = 0.01 m (Nemitz *et al.*, 2004). During the same experiment Nemitz *et al.* (2004) measured v_d =0.05 cm s^{-1} at night and v_d =1.0 cm s^{-1} during the day for D_p = 0.1–0.5 μm. Using corrections for hygroscopic particle growth, Vong *et al.* (2004) measured v_d over grass in the ranges 0.5–0.7 cm s^{-1} for $D_p \approx 0.34$ μm, 0.4–0.5 cm s^{-1} for $D_p \approx 0.54$ μm, and 0.7–0.9 cm s^{-1} for $D_p \approx 0.84$ μm.

Deposition velocities of accumulation mode particles (D_p = 0.1–1.0 μm) measured over a forest show an order of magnitude uncertainty from throughfall, eddy correlation, and other measurements (Gallagher *et al.*, 1997) (see Figure 1.21). For example, measurements for particles with a diameter of 500 nm are in the range 0.3–5 cm s^{-1}. Existing deposition models predict deposition velocities for 500 nm particles in the range 0.04–0.1 cm s^{-1}, since gravitational settling and Brownian diffusion are less efficient and deposition is thought to be mostly due to turbulent transport. These results suggest that our current understanding of the physical and chemical mechanisms that contribute to dry deposition is insufficient to predict dry

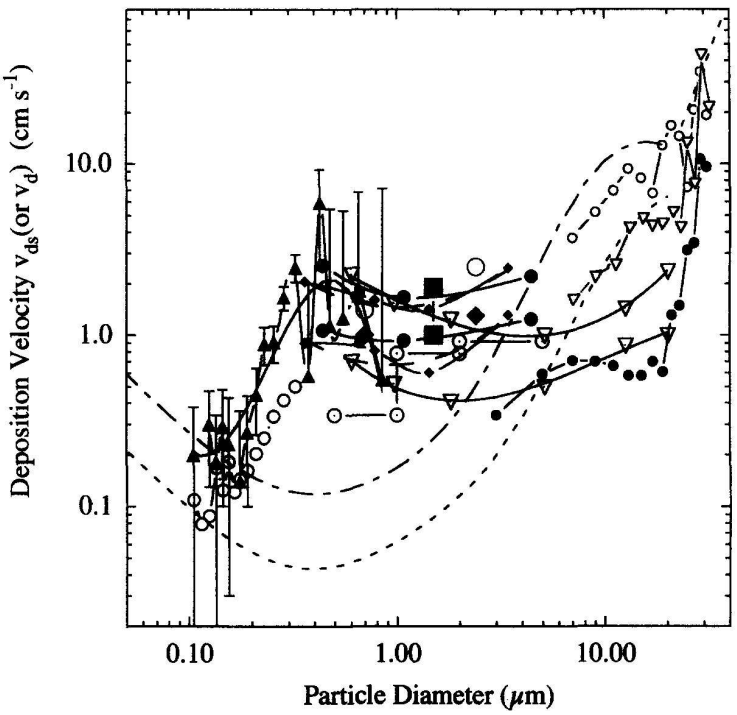

Figure 1.21: Particle deposition velocities to a forest canopy as a function of particle size (Gallagher *et al.*, 1997). The lines are model results from Slinn (1982) and the symbols are experimental results using different techniques.

deposition fluxes in atmospheric models (Wesely and Hicks, 2000; Gallagher *et al.*, 2002).

The chemical components associated with fine particles introduce toxic and nutrient materials to receptor ecosystems where they interact with water, soil, and plants. Atmospheric aerosols represent a vector for the transport of anthropogenic pollution downwind of their source. Thus, chemically speciated measurements of fine particle removal via dry deposition are necessary to inform air pollution models and determine environmental impacts. Speciated measurements of fine particle v_d have been limited by lack of aerosol instrumentation suitable for the eddy correlation method. Current methods for eddy correlation measurement of fine particle v_d rely on measurements of non-speciated particles using OPCs. These instruments measure particle volume to estimate mass concentrations. Under conditions of high humidity, particle volume is a non-conserved quantity due to water uptake by hygroscopic particles. Vong *et al.* (2004) estimated that hygroscopic growth accounted for approximately half of the

deposition flux measured using an OPC.

1.6.5. *Eddy Correlation Mass Spectrometry*

The eddy correlation mass spectrometry (ECMS) method uses an Aerodyne Quadrupole Aerosol Mass Spectrometer (Q-AMS) to save speciated fine particle concentration data. The Q-AMS has been used to characterize the composition and size distribution of ambient fine particles (e.g. Jayne *et al.*, 2000; Allan *et al.*, 2003b,a; Jimenez *et al.*, 2003; Canagaratna *et al.*, 2007). A new eddy correlation program (EC mode) was designed to collect concentration and time-of-flight data for one mass-to-charge ratio, m/z, characteristic of chemical species associated with fine particulate matter. The EC mode also generates an external square wave every 10 chopper cycles, $\approx$ 10 Hz, to trigger measurements with a colocated sonic anemometer. Using the eddy correlation equation, the deposition velocity, v_d, for particles is

$$v_d = \frac{-\overline{w'S'}}{\overline{S}} \tag{1.66}$$

where S is the Q-AMS signal, which is proportional to the concentration of the aerosol species monitored, and w is the vertical wind velocity measured by the sonic anemometer. Thus, the ECMS method can be used to measure speciated fine particle v_d. The v_d measured using ECMS is based on measurement of the concentration of chemical species in the sampled aerosol, a conserved quantity, and not the volume of the aerosol, which is not conserved due to water uptake (Vong *et al.*, 2004).

1.7. Dissertation Objectives

The primary objective of this research was to demonstrate eddy correlation mass spectrometry (ECMS) as a new method to measure speciated fine particle deposition velocities. The first part of this method development was to quantify the Q-AMS response in EC mode of the data acquisition software (Chapter 2). Laboratory experiments were conducted to simultaneously sample known mass loadings of calibration particles with the Q-AMS and a calibration instrument. A calibration curve was developed for the Q-AMS EC mode and compared to the data acquisition program used for ambient aerosol sampling.

The second part of this research was to address a common challenge of the eddy correlation technique. Atmospheric samples are commonly drawn through a sampling line to a concentration sensor for eddy correlation measurements. Isokinetic subsampling from the center of laminar flow is a widely-used technique to minimize loss of particles to sampling line walls. In this work, the attenuation of fine particle concentration fluctuations measured from isokinetically sampled laminar flow was measured for the first time (Chapter 2). The goal of this work was to demonstrate a method for sampling fine particles for eddy correlation measurements that maintains the temporal coherence of the aerosol with minimal particle loss. Theoretical predictions of attenuation of fine particle concentration fluctuations from isokinetically subsampled laminar flow were developed. The attenuation of fine particle concentration fluctuations using isokinetically sampled laminar flow was experimentally measured in the laboratory.

The third part of this research was to deploy the ECMS system to demonstrate the method in a field experiment (Chapter 3). A topographically simple agricultural site was chosen to measure speciated fine particle deposition velocities with the ECMS system. Standard eddy correlation criteria were used to segregate valid measurement periods. Deposition velocities were measured for fine particulate nitrate, organic, and sulfate aerosols.

The fourth part of this research was to measure gaseous and particulate nitrogen dry deposition fluxes at urban-influenced Sonoran sites in the Phoenix area (Chapter 4). Inferential measurements were used as a practical method to estimate fluxes over a widely distributed area. Denuder and filter samplers were used to measure atmospheric concentrations of gaseous and particulate nitrogen. Micrometeorological measurements were used to characterize the Sonoran desert atmospheric boundary layer. Meteorological measurements were used to calculate gas and particle deposition velocities for nitrogen flux calculations.

1.8. Nomenclature

Variables

A	characteristic radius
B	surface sublayer transfer coefficient
c	concentration
C_{air}	speed of sound in air
C_c	slip correction factor
Co	cospectrum
$\hat{c}_{\mathrm{p,air}}$	constant pressure heat capacity of air
$\hat{c}_{\mathrm{v,air}}$	constant volume heat capacity of air
d	instrument spatial resolution
$\mathcal{D}$	Brownian diffusivity
D_p	particle diameter
e	water vapor pressure
E_{B}	Brownian diffusion collection efficiency
E_{IM}	impaction collection efficiency
E_{IN}	interception collection efficiency
f	frequency
F	flux
F_a	aerodynamic layer flux
F_b	surface sublayer flux
F_M	momentum flux
g	gravitational constant
h	boundary layer height
k	von Karman constant
K_M	eddy momentum diffusivity
K_T	eddy heat diffusivity

l	eddy length scale
L	Obukhov length
L_v	latent heat of vaporization
m/z	mass-to-charge ratio
M	molecular weight
n	natural frequency
Og	ogive function
p	absolute pressure
p_0	surface pressure
Q_E	latent heat flux
Q_H	sensible heat flux
r_a	aerodynamic resistance
r_b	surface layer resistance
r_c	canopy resistance
r_t	total resistance
R	ideal gas constant
R_1	particle sticking coefficient
R_b	bulk Richardson number
R_i	Richardson number
R_v	water vapor ideal gas constant
S	Q-AMS signal
S_v	volumetric source/sink
Sc	Schmidt number, $\mu/\rho\mathcal{D}$
St	Stokes number, $v_s u_*^2/g\nu$
t	time
t_0	averaging time
t_i	integral time scale

T	temperature
T_v	virtual temperature
u	longitudinal wind velocity
u_*	friction velocity
U	mean wind speed
v	lateral wind velocity
v_{air}	air velocity
v_d	deposition velocity
v_s	gravitational settling velocity
w	vertical wind velocity
z	height above ground level
z_i	inversion layer height
z_{min}	minimum height
z_o	aerodynamic roughness length

Greek Symbols

α	empirical constant for impaction efficiency
β	empirical exponent for impaction efficiency
γ	heat capacity ratio (C_p/C_v)
γ_s	empirical constant for diffusion efficiency
Γ	dry adiabatic lapse rate
Δ	difference
ϵ	accuracy of a time average
ε_0	particle surface resistance constant
ζ	stability parameter
θ	potential temperature
θ_v	virtual potential temperature
λ	mean free path of air molecules

μ	viscosity of air
ν	kinematic viscosity of air
ρ_{air}	air density
ρ_p	particle density
σ	standard deviation of a variable
ϕ_M	momentum flux stability function
ϕ_T	heat flux stability function
Ψ_H	atmospheric stability function

Operators

$\overline{(\,)}$	mean
$(\,)'$	deviation from mean

2. ATTENUATION OF FINE PARTICLE CONCENTRATION FLUCTUATIONS IN ISOKINETICALLY SAMPLED LAMINAR FLOW

2.1. Introduction

Rapid measurement of gas and particulate concentrations have been used with synchronous wind velocity measurements to determine atmosphere-land fluxes using the eddy correlation method (Wesely *et al.*, 1983, 1985; Sievering, 1982; Gallagher *et al.*, 1997, 2002; Vong *et al.*, 2004; Pressley *et al.*, 2005; Velasco *et al.*, 2005). For valid flux calculations, the concentration measurements must be made with a frequency of 1 Hz or higher for the same air parcel as the wind measurements (Businger, 1986; Wesely and Hicks, 2000; Kaimal and Finnigan, 1994). Wind velocity measurements are usually made using a sonic anemometer mounted on a tower above the canopy. Many instruments used to measure gas and particulate concentrations cannot be mounted near sonic anemometers for practical reasons; for example the instrument may not be weatherproof, it may be too large for installation on a tower, it may require frequent maintenance and calibration, or it may cause distortions of wind at the anemometer. Therefore atmospheric samples are commonly drawn through a sampling line to a concentration sensor located at the base of the tower.

Sampling lines used for the eddy correlation method are designed to minimize both loss and frequency attenuation of the measured species. Isokinetic subsampling from the center of laminar flow is a widely-used technique to minimize loss of particles to sampling line walls (Brockman, 2001; Tyree and Allen, 2004). Particle diffusivities, $\mathcal{D}$, are orders of magnitude lower than gas molecules; for example, $\mathcal{D} = 5.5 \times 10^{-4}$ cm^2 s^{-1} for a spherical particle with diameter, D_p, 10 nm and density 1 g cm^{-3}. As a result, radial diffusion to the sampling line walls can be negligible. Transmission efficiencies for particles with $D_p > 10$ nm isokinetically sampled from a 1.1 cm inner diameter sampling line with length 10 m and Reynolds number 1300 (laminar flow) is > 99% (Tyree and Allen, 2004). Here frequency attenuation of particle sampling is evaluated for this design.

Concentration fluctuations are attenuated between the sampling line and instrument inlets as a result of differential axial velocities and radial transport. Predictions for dispersion

in laminar flows (Taylor, 1953) have been used to estimate attenuation of fluctuations for mixing-cup average concentration over the cross-section of a sampling line, $\langle C \rangle_{\text{main}}$ (Philip, 1963a,b,c; Leuning and Moncrieff, 1990; Lenschow and Raupach, 1991; Suyker and Verma, 1993). Taylor (1953) showed that the effective axial diffusion is

$$\frac{\partial \langle C \rangle_{\text{main}}}{\partial t} = \mathcal{D}_v \frac{\partial^2 \langle C \rangle_{\text{main}}}{\partial z^2} \tag{2.1}$$

where z is the axial direction. The virtual axial diffusion coefficient, $\mathcal{D}_v$, for laminar flows is approximately

$$\mathcal{D}_v \approx \frac{R\,U}{96}\,\text{Re}\,\text{Sc} \tag{2.2}$$

where R is the sampling line radius, U is the mean velocity in the sampling line, Re is the Reynolds number ($2\,\rho\,U\,R/\mu$), ρ is the density, μ is the viscosity, Sc is the Schmidt number ($\mu/\rho\,\mathcal{D}$), and $\mathcal{D}$ is the Brownian diffusion coefficient of the sampled species (Taylor, 1953). $\mathcal{D}_v$ incorporates attenuation due to differential axial advection and radial Brownian diffusion. Philip (1963a) showed that Equation 2.2 is valid for dimensionless frequency $\Omega < 10$ and $L/R \gg 0.05\,\text{Re}\,\text{Sc}$, where $\Omega = 2\,\pi\,f\,R^2/\mathcal{D}$, f is the frequency, and L is the length of the sampling line.

Predictions for dispersion in turbulent flows (Taylor, 1954) have also been used to estimate attenuation of $\langle C \rangle_{\text{main}}$ (Lenschow and Raupach, 1991; Massman, 1991). Taylor (1954) found the attenuation coefficient is approximately

$$\mathcal{D}_v \approx 2.02\,R\,U\,\text{Re}^{-1/8} \tag{2.3}$$

Attenuation is reduced compared to laminar flow because radial turbulent mixing is much larger than radial Brownian diffusion and the turbulent flow profile is approximately uniform (Taylor, 1953, 1954; Philip, 1963b). The resulting attenuation coefficients for $\langle C \rangle_{\text{main}}$ support the suggestion that turbulent flow sampling lines be used for eddy correlation flux measurements (Lenschow and Raupach, 1991).

Dispersion in laminar flow for species with large Péclet number, Pé $= RU/\mathcal{D} =$ ReSc, such as aerosol particles, can be divided into three regimes. For small times, symmetric ax-

ial dispersion results from diffusion-dominated transport and the Gaussian distribution is advected with the centerline velocity, $2U$. For large times, dispersion follows the convective-diffusion results of Taylor (1953) with radial and axial diffusion and advection at the mean velocity. In the intermediate time scale, "anomalous" dispersion is predicted with radial diffusion limited to the region near the centerline and radially-dependent axial spreading due to differential advection (Latini and Bernoff, 2001). The asymmetric distribution is advected at the centerline velocity in the intermediate dispersion regime.

Philip (1963a) developed a transfer function, Φ, for concentration fluctuations measured at the end of a sampling line

$$\frac{\langle C_{\text{out}}(\omega)\rangle_{\text{main}}}{\langle C_{\text{in}}(\omega)\rangle_{\text{main}}} = \Phi(\omega) = \mathrm{e}^{-\mathcal{D}_v \omega^2 L/U^3} \tag{2.4}$$

where $\langle C_{\text{out}}(\omega)\rangle_{\text{main}}$ and $\langle C_{\text{in}}(\omega)\rangle_{\text{main}}$ are the mixing-cup average concentrations at the sampling line outlet and inlet, respectively, and $\omega = 2\pi f$ is the frequency in radians per second. In principle, the transfer function can be used to recover the frequency spectrum of concentration fluctuations at the sampling line inlet from the spectrum measured at the outlet (Philip, 1963a). This technique has been used to correct frequency attenuation in eddy correlation flux measurements (Moore, 1986; Massman, 2000; Shimizu, 2007).

The attenuation and transfer function results for gases may not apply for aerosol particles because the transport properties of gases and particles are qualitatively different (Lenschow and Raupach, 1991). The Schmidt number for gases is on the order of 1; for example Sc = 0.595 for water vapor in air (Bird *et al.*, 2002). For particles Sc $\gg$ 1, for example Sc = 2.1×10^4 for a 100 nm particle (Hinds, 1999). Therefore, in the particle case $\Omega \gg 10$ and $L/R \ll 0.05\,\mathrm{Re}\,\mathrm{Sc}$, and Equation 2.2 does not apply. Kristensen derived the transfer function for a solute with infinite Schmidt number (Lenschow and Raupach, 1991, Appendix). The transfer function is found from the autocovariance of the concentration fluctuations at the outlet of the sampling line as a function of the corresponding fluctuations at the inlet. The square of the transfer function is

$$\Phi^2(\omega) = \left|\phi(\omega)\right|^2 \tag{2.5}$$

where

$$\phi(\omega) = \frac{L^2}{2U^2} \int_{\frac{L}{2U}}^{\infty} \frac{e^{i\omega t}}{t^3} dt \tag{2.6}$$

where the frequency response, ϕ, is for the mixing-cup average of the sampling line, integrated over the residence time of fluid parcels from the centerline to the tube wall. Lenschow and Raupach (1991) showed that attenuation of concentration fluctuations measured through a sampling line is greater for aerosol particles than that for gases because Brownian diffusion mitigates the effect of differential advection.

Isokinetic sampling is routinely used to collect representative particles by subsampling from the center of a laminar flow (Hinds, 1999). In this method, the subsample is extracted by matching the velocity in the probe with volumetric flow rate $\dot{V}_{\text{isok}}$ to the velocity in the central region of the main flow (see Figure 2.1). The gas velocity profile in the main flow is parabolic due interaction with the walls. The profile in the isokinetic region, however, has approximately plug flow behavior since flow in this region is close to the maximum velocity and axial dispersion is smaller in the intermediate dispersion regime than in the diffusion or Taylor regimes (Latini and Bernoff, 2001). Thus, for particles, attenuation of concentration fluctuations, averaged over the isokinetic region, $\langle C \rangle_{\text{isok}}$, is expected to be lower than attenuation of $\langle C \rangle_{\text{main}}$. For sufficiently long sampling lines, isokinetic sampling of gases is expected to produce results similar to the main flow since Brownian diffusion results in radial mixing of gas molecules between the centerline and the tube wall.

Here the attenuation of fine particle concentration fluctuations measured from isokinetically sampled laminar flow is measured for the first time. The goal of this work is to demonstrate a method for sampling fine particles for eddy correlation measurements that maintains the temporal coherence of the aerosol with minimal particle loss. Step changes in concentrations were introduced and the attenuation of isokinetically sampled laminar flow was measured. Fast response measurements of particle concentrations were made using a Quadrupole Aerosol Mass Spectrometer. An eddy correlation program for the Q-AMS software saves concentration data at $\approx$ 10 Hz. The experimental response times and transfer functions

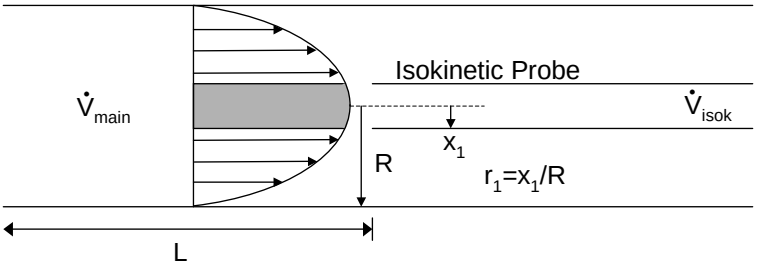

Figure 2.1: Schematic diagram of isokinetic sampling system where $\dot{V}_{\text{main}}$ is the volumetric flow rate in the main flow sampling line, $\dot{V}_{\text{isok}}$ is the flow rate of the isokinetic subsample, L is the length of the sampling line, R is the main flow sampling line radius, x_1 is the radius of the isokinetic probe, and r_1 is the dimensionless isokinetic radius. The shaded area indicates the central region of the main flow that is sampled isokinetically.

for $\langle C \rangle_{\text{isok}}$ were calculated and the results are compared with the transfer functions for $\langle C \rangle_{\text{main}}$ in laminar and turbulent flows. A theoretical transfer function for $\langle C \rangle_{\text{isok}}$, integrated over the isokinetic region, was developed to evaluate the experimental results.

2.2. Methods

Laboratory experiments were conducted to measure isokinetically sampled aerosols in a configuration designed for practical eddy correlation measurements using a Quadrupole Aerosol Mass Spectrometer (Q-AMS, Aerodyne Research Inc., Billerica, MA) (Jayne *et al.*, 2000; Canagaratna *et al.*, 2007). For field measurements of fine particle fluxes, ambient air is sampled using a size-selective cyclone to remove large particles. The air is then drawn through a sampling line under laminar conditions. For example, a flow rate of 10 l min^{-1} in a 0.5 inch outer diameter sampling line results in a Reynolds number of 1300. The flow into the aerosol particle sensor can be isokinetically subsampled from the centerline of the laminar flow. For a Q-AMS inlet flow rate of 1.5 $\text{cm}^3\,\text{s}^{-1}$, the ratio of the isokinetic probe radius to the sampling line radius, $r_1 = x_1/R$, is 0.06 to match the gas velocity in the probe to the velocity in the isokinetic region of the main flow.

Step changes in particle concentrations were pulsed through the sampling line to the Q-AMS in order to measure the response time for isokinetically sampled laminar flows. Aerosols

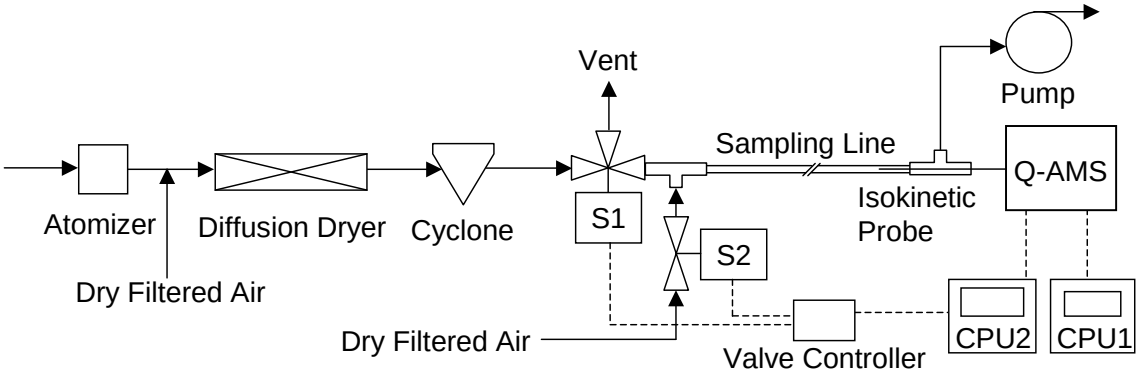

Figure 2.2: Schematic diagram of the pulsed aerosol laminar flow experimental apparatus. Polydisperse aerosols were generated using a Collison atomizer and diluted with dry, filtered air. The aerosol was passed through a diffusion dryer and cyclone. The aerosol was pulsed into the laminar flow sampling line using a three-way solenoid valve (S1), which was then isokinetically sampled into the Quadrupole Aerosol Mass Spectrometer (Q-AMS). A two-way solenoid valve (S2) was used to control dry filtered air flow into the sampling line when the aerosol did not flow into the sampling line. The solenoid valves were switched simultaneously with one valve controller. The solenoid control voltage and the Q-AMS trigger signal were recorded synchronously using a data acquisition system (CPU2). Aerosol composition data were recorded using CPU1.

were generated with a Collison atomizer using compressed air filtered through a high efficiency particulate air (HEPA) filter and an aqueous solution of NH_4NO_3 (see Figure 2.2). The aerosols were then diluted with dry, HEPA-filtered air at ambient pressure to provide a total sample flow of 9.9 l min^{-1}. The aerosols were dried using a silica gel diffusion dryer (Model 3062, TSI, Shoreview, MN). Large particles were removed from the aerosol using a size-selective cyclone (Model 2000-30EN, URG, Chapel Hill, NC) with a 50% cutpoint diameter of 2.5 μm.

Aerosol flow was pulsed into the apparatus using a three-way solenoid valve (Model 009-0143-900, Parker Hannifin, Fairfield, NJ). Dry, filtered air was alternately introduced into the apparatus using a two-way solenoid valve (Model 009-0339-900, Parker Hannifin). The solenoid valves had a response time of 0.005 s and were simultaneously actuated using a single control channel on an electronic valve controller (Valve Driver II, Parker Hannifin). Switching

of the solenoid valves was manually controlled to generate step changes of 60 s duration, alternated with 120 s of dry, filtered air. The apparatus was designed to maintain constant pressure and laminar flow profile in the sampling line when the solenoid valves were switched. The valve connections were configured so that laminar flow was uninterrupted for particle concentration pulses. Cross flow of the filtered air input through the tee fitting produced radial mixing for step decreases in particle concentration.

The laminar aerosol flow was sampled through cleaned copper sampling lines with inner radius of 0.55 cm to determine $\langle C_{\mathrm{out}}(\omega)\rangle_{\mathrm{isok}}$. Laminar flow in the sampling line was maintained by drawing a constant volumetric flow rate, $\dot{V}_{\mathrm{main}} = 9.9 \pm 0.1\ \mathrm{l\,min^{-1}}$, controlled by a 0.045 cm diameter critical orifice at the sampling line outlet. The vent flow from solenoid valve S1 was drawn at $\dot{V} = \approx 9.9\ \mathrm{l\,min^{-1}}$ through a copper tube with inner radius of 0.55 cm to maintain constant aerosol flow and equalize pressure at both outlets of the solenoid valve. Experiments were conducted using a sampling line made up of four sections of straight tubing, each with a length of 1.83 m joined with Ultra-Torr vacuum fittings, and a 1 m section at the inlet. Ultra-Torr fittings were used so that the inner diameter of the tubes were not affected by the connectors, as is the case for compression fittings. Experiments were conducted using the same sampling line with the cyclone attached directly to the sampling line to investigate the effect of the cyclone usually used in field sampling experiments. Experiments were also conducted with the inlet only (no sampling line) to determine $\langle C_{\mathrm{in}}(\omega)\rangle_{\mathrm{isok}}$ for isokinetically sampled aerosols.

The aerosol flow was isokinetically sampled into the Q-AMS using a tube with 0.3175 cm outer diameter and 0.069 cm inner diameter, which was machined to a knife edge ($r_1 = 0.062$, see Figure 2.1). The Q-AMS inlet flow rate was 1.5 $\mathrm{cm^3\,s^{-1}}$, resulting in a Reynolds number of 160 in the isokinetic probe. The Q-AMS was operated in eddy correlation mode (see below) monitoring the abundance of $m/z = 30$ ions, characteristic of NO^+ from nitrate.

In some experiments, the aerosol flow was mixed near the sampling line outlet so that the sampled aerosol represented the mixing-cup average concentration. A cylindrical baffle

with an outer diameter of 0.6 cm was positioned ≈ 5 cm upstream of the isokinetic probe in the sampling line. This baffle induced radial mixing of the aerosol so that the subsampled aerosol was effectively averaged over the entire radius of the sampling line. Flow around the baffle was turbulent with a Reynolds number of 2600 at the constriction.

Particle concentrations in the isokinetic subsample were measured using the Q-AMS (Jayne *et al.*, 2000; Jimenez *et al.*, 2003; Canagaratna *et al.*, 2007). Particles were focused by an aerodynamic lens, the aerosol was expanded supersonically through an orifice, and the resulting particle beam was modulated by a chopper wheel, rotated at ≈ 100 Hz. The size-dependent particle time-of-flight through a 0.39 m vacuum chamber was used to measure the vacuum aerodynamic diameter, D_{va}. The aerosol was directed onto a resistively heated surface and the nonrefractory (NR) components of the aerosol were vaporized at ≈ 600 °C. The vapor was then ionized by electron impact using an ionizer filament, positioned along one edge of the ionization region housing, which also provided radiative heating. Ions were filtered by a quadrupole mass spectrometer which output a signal proportional to the concentration of ions at specified mass-to-charge ratios.

The Q-AMS was operated in two data acquisition program modes: particle time-of-flight (PToF) mode and eddy correlation (EC) mode. In PToF mode five minute averages of particle time-of-flight data were saved (Jimenez *et al.*, 2003; Canagaratna *et al.*, 2007). The Q-AMS was calibrated in PToF mode using published procedures (Jayne *et al.*, 2000; Allan *et al.*, 2003b). The quadrupole filter and the gain of the electron multiplier were calibrated for optimum instrument response. The ionization efficiency of nitrate was also measured to determine the instrument response to a known input.

The new EC mode program was designed to collect concentration and time-of-flight data for one mass-to-charge ratio (or chemical species) and generate an external square wave trigger every 10 chopper cycles, ≈ 10 Hz. In this program, the raw quadrupole and chopper signals were acquired at a rate of 1 MHz. This is equivalent to ≈ 10^4 data points per chopper cycle which was subsequently reduced to 10^3 data points per chopper cycle in the data acqui-

sition program. Quadrupole data were then synchronized with the chopper open signal and 10 sequential chopper cycles were averaged. The EC mode program was designed to record the quadrupole measurements in approximately 200 time-of-flight (ToF) bins at ≈ 10 Hz. An incremental counter was recorded for each trigger pulse which was later used to synchronize the Q-AMS signal with the trigger signal. Each 30 minute period of the 10 Hz averaged signal was saved to a Hierarchical Data Format (HDF 4) file (NCSA, 2000).

The square wave trigger signal from the Q-AMS, operating in EC mode, and the solenoid actuation voltage were recorded using a custom Java data acquisition system and a 200 kHz data acquisition board (Model PCI-6024E, National Instruments, Austin, TX). Since each square wave trigger pulse corresponds to one 10 Hz average time-of-flight spectrum saved by the Q-AMS, the trigger signal was used to synchronize the Q-AMS measurements with the solenoid actuation voltage. The lag between the time when the solenoid was switched and the time when particles were first detected by the Q-AMS was calculated for each aerosol step input. Particle transit times for each sampling line were calculated as the mean of the measured lag times.

Laboratory experiments were also conducted to measure the response of the Q-AMS operating in EC mode. Aerosols were generated using a Collison atomizer with aqueous NH_4NO_3 solutions to produce polydisperse calibration aerosols. These aerosols were then size selected with a dynamic mobility analyzer (DMA, Model 3081, TSI) to produce particles with mobility diameters of 200, 350, 450, and 550 nm in concentrations from 0.1 μg m^{-3} to 4 μg m^{-3}. The monodisperse aerosols were then isokinetically sampled into the Q-AMS, operated in EC mode. The main aerosol flow was simultaneously counted with a condensation particle counter (CPC, Model 3025, TSI). Filtered air was sampled between experiments to measure the background signal. The experiments were repeated in PToF mode to compare the instrument response in EC and PToF modes.

2.3. Results

2.3.1. *Eddy Correlation Mode Calibration*

The Q-AMS PToF mode signal was recorded relative to a baseline which was determined using the data acquisition software. Approximately 3×10^7 data points were averaged in PToF mode for each five minute period. A velocity calibration of this Q-AMS instrument showed that the times-of-flight, ToF, were 3.1 ms, 4.5 ms, and 6.8 ms for 30 nm, 300 nm, and 3000 nm particles, respectively. Gas molecules had a time-of-flight of $\approx$ 1.2 ms. The mean signal in two user-defined "DC [drift chamber] regions" (typically 0.5 < ToF < 1.5 ms and 7.0 < ToF < 9.0 ms, where no particles are expected) was used to calculate the zero signal baseline level (Allan *et al.*, 2003b; Canagaratna *et al.*, 2007). In EC mode, approximately 10^4 data points were averaged in 0.1 s. Single particles and electronic noise produced signal spikes in the DC regions over this shorter averaging period (see Figure 2.3). Thus, the EC mode required a new technique to determine the zero signal baseline in the time-of-flight spectrum. The median of the raw signal was less sensitive to signal spikes. Random electronic noise would result in a normal distribution of signal median values; single particles would result in a negatively skewed distribution since such spikes would be large and positive. Typically, the raw signal distribution was negatively skewed with approximately 33% of the ToF spectra affected by single particle events (see Figure 2.3). The median was subtracted from each $\approx$ 10 Hz ToF spectrum to re-baseline the Q-AMS data collected in EC mode. The re-baselined signal was then used for all subsequent calculations.

Signal peaks were clearly resolved in the time-of-flight data collected with the Q-AMS in PToF mode. For example, 350 nm NH_4NO_3 particles produced a peak at ToF = 4.8 ms (see Figure 2.4). A small signal was also observed soon after the chopper wheel was opened at the start of the time-of-flight measurement cycle (ToF < 0.5 ms in Figure 2.4). This signal matched the timing and duration of the chopper wheel opening which lasted for 3.5×10^{-2} ms for the chopper duty of 3.5%. The opening was detected using measurements from an infrared photo-diode detector pair. These data were saved to the same data acquisition board as the

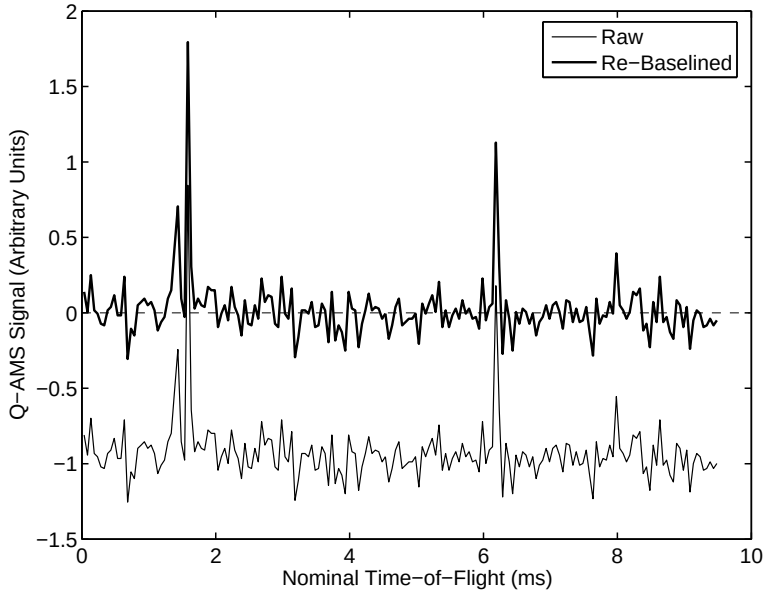

Figure 2.3: An example of the re-baselining method for a time-of-flight spectrum measured by the Q-AMS eddy correlation (EC) mode. The re-baselined signal was calculated as the raw signal minus the median of the raw signal for each 10 Hz time-of-flight spectrum.

Q-AMS concentration signal. The peak observed at the start of the time-of-flight cycle was likely crosstalk between the photo-diode and the electron multiplier.

No peak was observed in the EC mode signal for 350 nm NH_4NO_3 particles at ToF = 4.8 ms, where 350 nm particles are expected (see Figure 2.4). At all ToF < 2.5 ms the EC mode signal was above the baseline, including an order of magnitude increase in the range 1.5–2.5 ms. Note that negligible particle signal was expected in this time range which corresponds to D_{va} < 6 nm. For comparison, the PToF mode data scaled in ToF time by a factor of 10 matched the EC mode. Thus, the EC mode data appeared to have been truncated to include only ToF = 0–1 ms, not averaged to include ToF = 0–10 ms as is done for PToF mode data.

Despite erroneous data acquisition, the signal in EC mode consistently increased with mass loading of NH_4NO_3 particles (see Figure 2.5). This observation is consistent with delayed vaporization of some of the calibration aerosol which produced ion signal after the end of one ≈ 10 ms chopper cycle; and this signal was recorded in the beginning 1 ms of the next chopper cycle (“wrap around” signal). The half width of the ion pulse from single particle

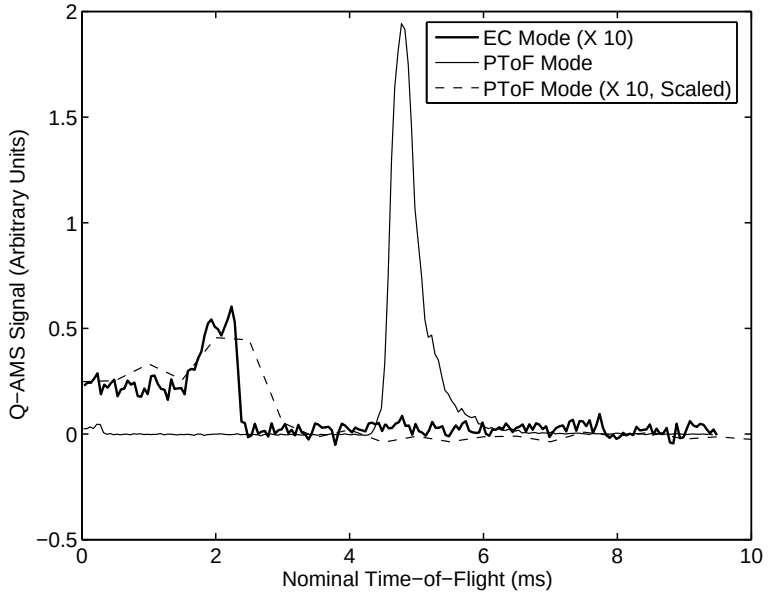

Figure 2.4: Five minute averaged Q-AMS signal versus time-of-flight for 350 nm NH_4NO_3 aerosols (data for $m/z = 30$ only) in particle time-of-flight (PToF) mode and eddy correlation (EC) mode. Particles were clearly resolved in PToF mode at ≈ 4.8 ms. No signal was observed at the same time-of-flight in EC mode. At time-of-flight less than ≈ 3 ms, the signal measured in PToF mode scaled by a factor of 10 in time-of-flight space matched the signal measured in EC mode.

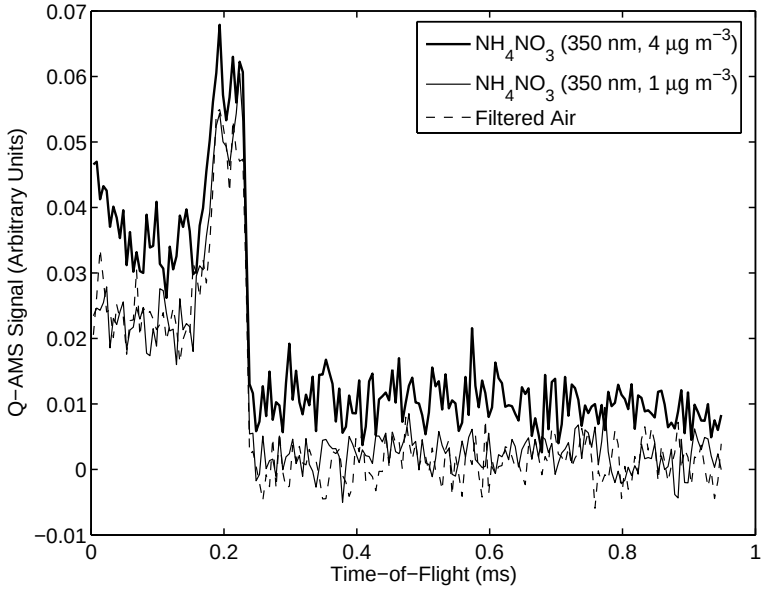

Figure 2.5: Five-minute averaged Q-AMS signal versus time-of-flight for two concentrations of 350 nm NH_4NO_3 aerosols and filtered air in the eddy correlation program (EC mode data for $m/z = 30$ only).

flash vaporization was $\approx 30\ \mu s$ (Jayne *et al.*, 2000); however, temperature gradients in the vaporization chamber likely caused condensation of a fraction of the aerosol on cooler surfaces followed by slow vaporization. This is likely for semivolatile NH_4NO_3 aerosol introduced at relatively high concentrations used for the Q-AMS calibration.

Response curves were calculated for the EC and PToF modes using the Q-AMS signal summed over the measured time-of-flight range. The average signal was 0.5 ± 0.1 Hz for filtered air sampled in PToF mode. A linear fit to the PToF mode measurements yielded a detection efficiency (slope of the line) of ≈ 20 Hz/(μg m^{-3}) for 350 nm particles (see Figure 2.6). Thus, the limit of detection for nitrate in PToF mode was $\approx 0.05\ \mu$g m^{-3}, in the range of the reported detection limits for the Q-AMS (Canagaratna *et al.*, 2007). In the EC mode, the average signal was 1.4 ± 0.2 Hz for filtered air. The detection efficiency was ≈ 0.6 Hz/(μg m^{-3}) for 350 nm particles, or less than 3% of the PToF mode detection efficiency. The EC mode signal response was linear with a limit of detection of $\approx 0.33\ \mu$g m^{-3}. The Q-AMS detection efficiency in both EC and PToF modes decreased for 450 and 550 nm particles due to transmission losses

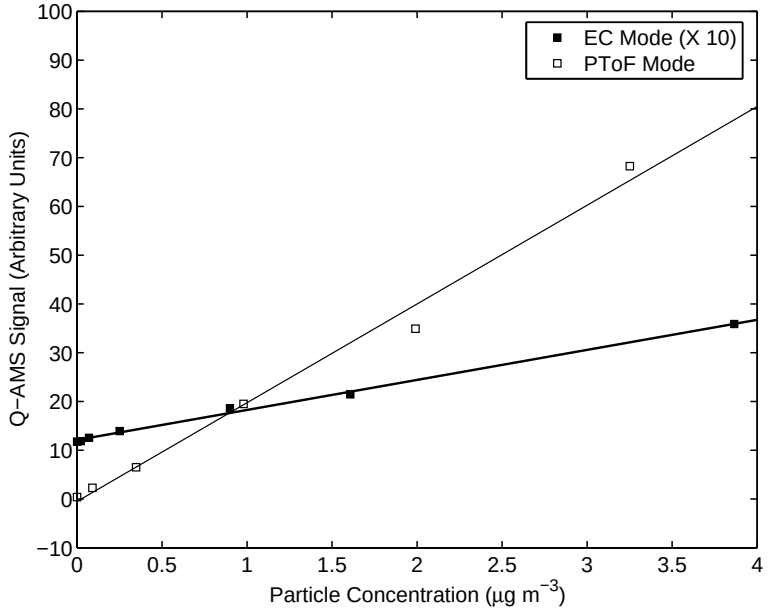

Figure 2.6: Q-AMS response to varying concentrations of 350 nm NH_4NO_3 aerosols in the eddy correlation (EC) mode and particle time-of-flight (PToF) modes. The lines show linear regressions of the experimental data. The limit of detection for the EC mode (0.33 μg m^{-3}) is approximately seven times lower than the PToF mode (0.05 μg m^{-3}).

in the aerodynamic lens (Jayne *et al.*, 2000).

2.3.2. *Laminar Flow Sampling*

Transit times of fluid parcels along the centerline in the sampling line of the experimental apparatus can be calculated for comparison with experimental results. The entrance length required for fully-developed laminar flow is $L_e \approx D(0.055\mathrm{Re} + 0.26)$, where D is the sampling line diameter (Perry and Green, 1997). Fluid flow in the entrance region was assumed to follow a plug flow profile and the velocity is equal to the flow-averaged velocity, U. The flow was assumed to be fully-developed laminar flow through the remaining length of the sampling line, $L > L_e$. The velocity at r is

$$u(r) = 2U\left(1 - r^2\right) \tag{2.7}$$

and the centerline velocity is $2U$. The total transit time along the centerline is then $\Delta t_{\mathrm{line}} \approx (L + L_e)/2U$. Transit times in the isokinetic probe and the Q-AMS inlet fittings were also

calculated, assuming plug flow, using $\Delta t_{inlet} \approx V_{inlet}/\dot{V}_{isok}$, where V_{inlet} is the volume of the probe and fittings and $\dot{V}_{isok}$ is the Q-AMS flow rate of 1.5 $cm^3\,s^{-1}$. The total particle transit time is $\Delta t = \Delta t_{line} + \Delta t_{inlet}$ (see Table 2.1). The calculated inlet residence time was 0.5 s for all experiments and the cyclone residence time was approximately 0.2 s. The uncertainty for the calculated total transit times was ≈ 0.1 s, mainly due to the uncertainty in the estimate of V_{inlet}. Transit time in the Q-AMS is small (≈ 10 ms) and was ignored for these calculations.

Table 2.1: Transit Times, Δt, for Laminar Flow Sampling Lines with Length, L, and Entrance Region Length, L_e, for Development of Laminar Flow.

Experiment	# of Runs	L_e (m)	$\Delta t_{calculated}$ (s)	$\Delta t_{measured}$ (s)
Inlet Section (No Sampling Line)	9	0	0.5 ± 0.1	0.2 ± 0.1
Straight Line (L = 8.3 m, r_1 = 0.06)	10	0.8	3.1 ± 0.1	3.1 ± 0.1
Straight Line with Cyclone (L = 8.3 m, r_1 = 0.06)	10	0.8	3.3 ± 0.1	3.1 ± 0.1
Straight Line (L = 8.3 m, r_1 = 1.0)	8	0.8	3.1 ± 0.1	3.3 ± 0.2

Transit times were measured for each experimental run. The start of each step input was defined as the time when the solenoid valve was opened, t_0. Each ≈ 60 s step input was then separately normalized such that the mean signal was zero for filtered air sampling and scaled to one for calibration particle sampling. The particle detection time, t_p, of the step input was identified as the time when the normalized signal, N, was greater than 3 times the standard deviation of N during filtered air sampling (see Figure 2.7). The transit time, Δt, was calculated as $t_p - t_0$. For each experiment, the standard deviation of the transit times was 0.1 s, calculated from 8–10 aerosol step input pulses. The mean transit time in the inlet was lower than the calculated value (see Table 2.1), likely due to uncertainty of the inlet dimension estimates. The mean transit times for the 8.3 m sampling line agree with the calculated values. The cyclone residence time was less than the 0.1 s resolution of the measurements, determined by the difference between the transit times from the sampling line experiments with and without the cyclone. These results indicated that the radial profile in the sampling line was parabolic and the isokinetic probe was aligned near the centerline of the

main flow.

2.3.3. *Laminar Flow Concentration Attenuation*

Attenuation time constants, τ, of the sampling system were determined for each sampling line by fitting the mean of the normalized step change experimental runs to an exponential equation

$$N = 1 - e^{(-(t-t_p)/\tau)} \tag{2.8}$$

using a nonlinear least squares regression. Except for the inlet section, fit of Equation 2.8 to the individual step changes for each experiment, rather than the mean, resulted in mean values of τ within 0.01 s of the results presented here. For the inlet section $\tau = 4.5 \times 10^{-7}$ s was found by fitting the mean of all nine runs and a mean value of $\tau = 0.03$ s was found by fitting each run individually. Results from the first method are reported here since the mean of multiple experimental runs removed noise in the Q-AMS signal. The data were also fit to a two-component exponential function, $N = 1 - (e^{(-(t-t_p)/\tau)} + N_2 e(-(t - t_p)/\tau_2))$. The two-component equation yielded no improvement to the fit and $N_2 < 0.1$ for all experiments; therefore Equation 2.8 was used.

Error in the measured value was estimated from the root mean squared error using the residuals from the nonlinear regression. The precision of τ was better than the Q-AMS measurement precision since τ was calculated from repeated experiments in which the timing of the solenoid valves and the Q-AMS averaging period were not synchronized. Thus, the resolution along the exponential growth curve could be improved using additional repeated experiments.

Regression of the experiment data resulted in τ for each of the sampling line step input experiments (see Figures 2.8 and Table 2.2). Attenuation in the inlet section accounts for temporal spreading in the isokinetic probe and Q-AMS inlet fittings. This minimum attenuation can then be compared with attenuation in the sampling line. Attenuation in the straight line was apparent in the exponential fit compared to the inlet section (see Figures 2.8a & b). The τ for the straight sampling line with the cyclone was 0.2 ± 0.08 s compared to 0.1 ± 0.12 s with-

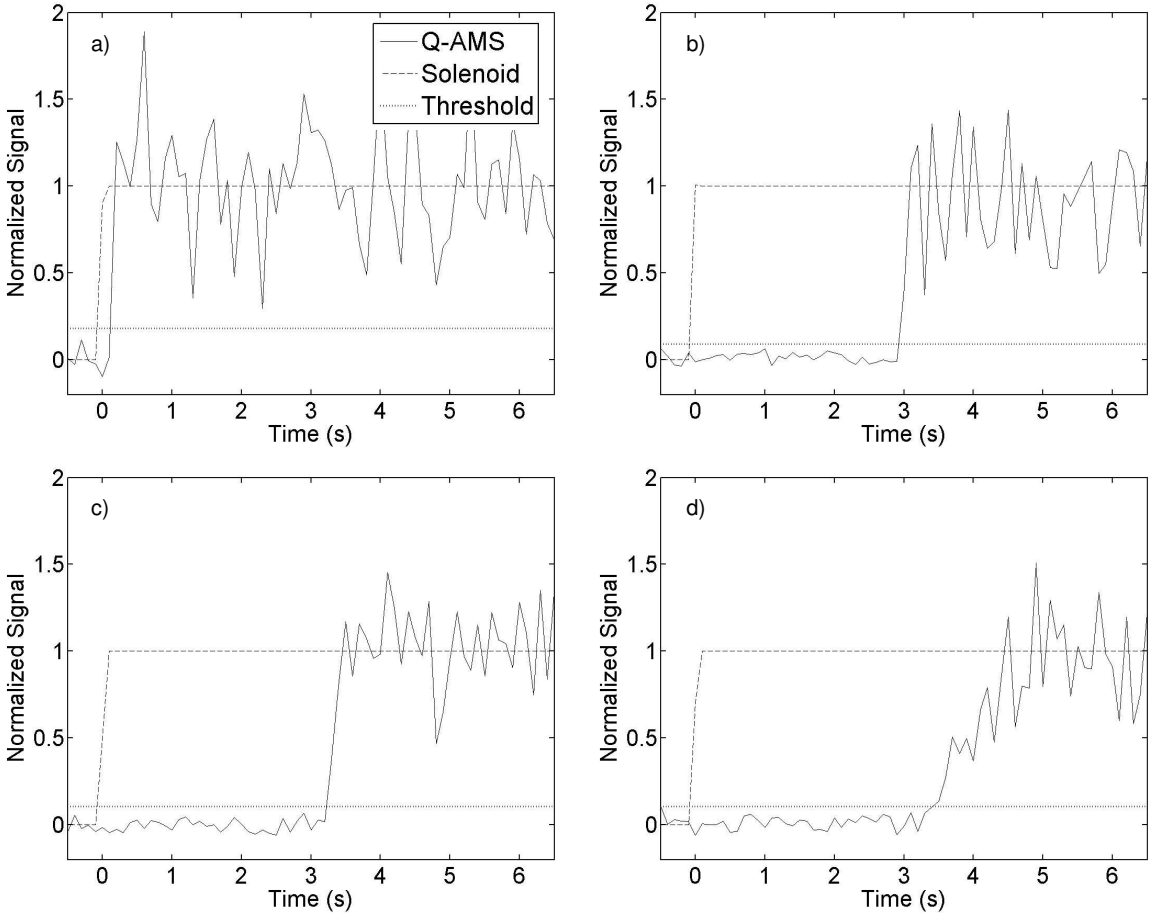

Figure 2.7: Normalized Q-AMS signal measured for pulsed aerosol laminar flow experiments through a) inlet section (no sampling line), b) straight line with isokinetic sampling (L = 8.3 m, r_1 = 0.06), c) straight sampling line using a size-selective cyclone with isokinetic sampling (L = 8.3 m, r_1 = 0.06), and d) straight sampling line with nonisokinetic sampling (L = 8.3 m, r_1 = 1). The time difference between the solenoid voltage change at t = 0 and the Q-AMS signal increase above the threshold represents the transit time in the sampling lines.

out the cyclone, indicating that a size-selective cyclone does not greatly reduce the frequency response of the system. Nonisokinetic sampling from the straight sampling line resulted in significant attenuation, evidenced by a gradual increase in the normalized signal after t_p.

Table 2.2: Attenuation Time Constants, τ, and Spreading Times, δ, Measured in Laminar Flow Sampling Lines.

Experiment	τ (s)	δ (s)
Inlet Section (No Sampling Line)	$4.5\times10^{-7} \pm 0.12$	0
Straight Line (L = 8.3 m, r_1 = 0.06)	0.10 ± 0.12	4.4×10^{-3}
Straight Line (L = 8.3 m, r_1 = 0.06) with Cyclone	0.15 ± 0.08	—
Straight Line (L = 8.3 m, r_1 = 1.0 [a])	0.67 ± 0.07	2.4

[a] Simulated using a cylindrical baffle.

2.3.4. *Laminar Flow Particle Spreading*

The velocity profile in the main flow is parabolic, resulting in radially differential advection of particles through the sampling line. Temporal spreading of particles is apparent when sampling across a finite radius which includes particles with different residence times. This temporal spreading can be estimated as the difference between the average transit times of particles from the centerline of the flow to dimensionless radius r and those at the centerline $r = 0$. The average residence time of particles from the centerline to r is

$$\overline{t_r} = \frac{\int t_r 2\pi r u \, \mathrm{d}r}{\int 2\pi r u \, \mathrm{d}r} \tag{2.9}$$

where $t_r = L/u$ is the transit time for particles with velocity u. The spreading time is $\delta = \overline{t_r} - t_c$ where t_c is the transit time at the centerline of the flow. Then the area averaged δ is

$$\delta = \frac{L}{2U}\left(\frac{1}{1-\frac{r^2}{2}} - 1\right) \tag{2.10}$$

Temporal spreading was negligible in the inlet section since the velocity profile is approximately uniform. In the sampling line, temporal spreading was calculated to be 4.4×10^{-3} s and 2.4 s for the isokinetic and nonisokinetic laminar flow experiments, respectively (see Table 2.2).

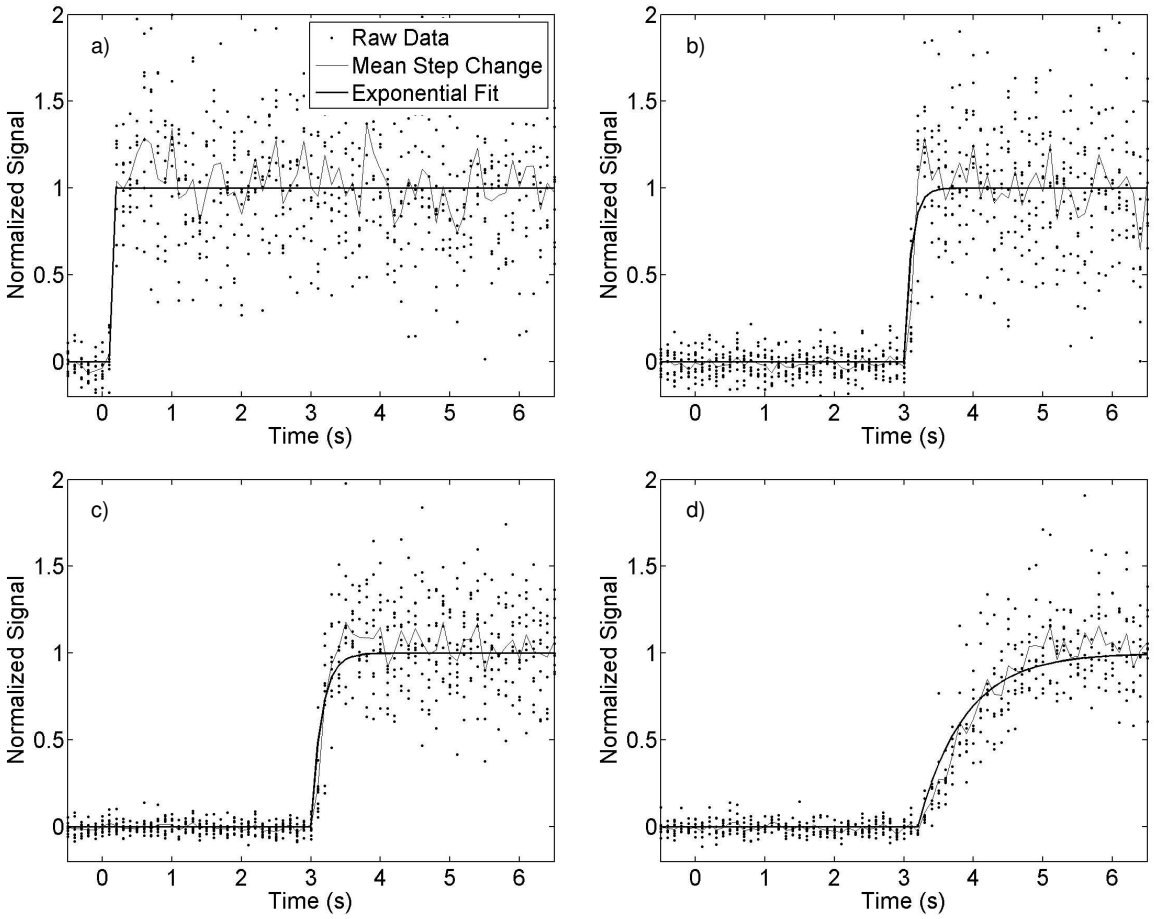

Figure 2.8: Normalized Q-AMS signals in response to pulsed aerosol in laminar flow sampling lines with fitted exponential growth curves for experiments a) inlet section (no sampling line), b) straight line with isokinetic sampling (L = 8.3 m, r_1 = 0.06), c) straight line using a size-selective cyclone with isokinetic sampling (L = 8.3 m, r_1 = 0.06), and d) straight line with nonisokinetic sampling (L = 8.3 m, r_1 = 1). The mean of all 8–10 runs was used to determine the fit using a nonlinear least squares regression of the data for signal measured after particle detection time, t_p.

Methods to estimate temporal spreading in the cyclone are not readily available. The flow profile in cyclones is not well understood (Darby, 2001) and mixing in the cyclone is expected to complicate estimates based on an assumed flow. In these experiments, the residence time in the cyclone was below the measurement precision of the sampling system and much less than the residence time in the sampling line. Here temporal spreading in the experiment with the cyclone was assumed to be negligible compared to the sampling line spreading.

2.3.5. *Prediction of Isokinetic Sampling Concentration Transfer Function*

Kristensen's transfer function for laminar flow with Sc → ∞ (Equation 2.6) accounts for differential advection of aerosol sampled from the entire main flow (Lenschow and Raupach, 1991, Appendix). For isokinetically subsampled laminar flow, only particles in the isokinetic region, where differential advection is small, are sampled (see Figure 2.1). Theoretical prediction of τ for $\langle C \rangle_{\text{isok}}$ in these experiments was calculated using

$$\phi_{\text{isok}}(\omega) = \frac{L^2}{2U^2} \int_{t_c}^{t_r} \frac{e^{i\omega t}}{t^3} dt \tag{2.11}$$

which is analogous to Equation 2.6 with integration limited to the subsampled region. In the limit $r_1 \to 1$, Equation 2.11 is equivalent to Equation 2.6. Equation 2.11 was integrated numerically for dimensionless radii in the range $r_1 = 0.01$–0.99 using the sampling line dimensions and flow rates of the experiments above: $R = 1.1$ cm, $U = 1.7$ m s^{-1}, and $L = 8.3$ m. The resulting Φ^2 was plotted versus dimensionless frequency, $n = f/f_0$, where $f_0 = U/L$ is the flow frequency (see Figure 2.9). Some rippling was apparent in the stopband region, the band of frequencies at which $\Phi^2 \to 0$. This type of out-of-band rippling can be neglected since the stopband has no effect on the applied transfer function (Lyons, 2001).

The dimensionless half-power frequency, $n_{0.5}$ at which $\Phi^2(n) = 0.5$, was determined from the transfer function for each dimensionless radius to estimate the attenuation characteristics predicted by Equation 2.11. This frequency corresponds to the cutoff frequency determined by the 3 dB power loss point of a digital signal filter (Lyons, 2001). In the range of dimensionless radii $r_1 = 0.01$–0.99 the range of $n_{0.5}$ was 0.0088–0.40, more than four orders of magnitude. For the dimensionless isokinetic radius used here, $r_1 = 0.06$, $n_{0.5} = 2.5 \times 10^2$

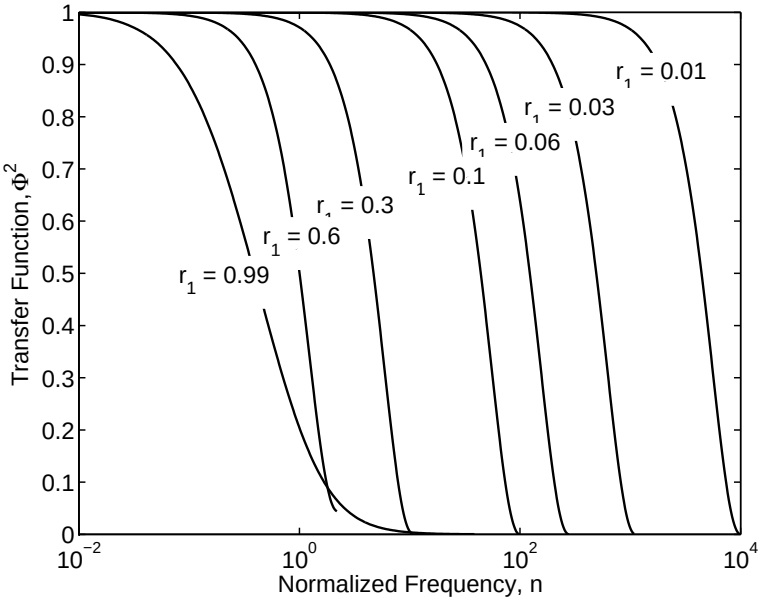

Figure 2.9: Squared transfer function for isokinetic sampling of a solute with Sc → ∞ for a range of dimensionless radii, r_1. For clarity, the plotted transfer function is truncated at the zero-power frequency.

and for nonisokinetic sampling, $r_1 = 1$, $n_{0.5} = 0.40$.

The sharpness of the transfer function can be described by the frequency roll-off of the transition region, the frequency range over which Φ^2 decreased from 0.5 (3 dB power loss) to 0.01 (20 dB power loss). The roll-off, w, is defined as the magnitude of the signal power lost in the transition region for every octave (doubling of the frequency) and is calculated as

$$w = \frac{P}{\frac{1}{2}\left(\frac{n_{0.01}}{n_{0.5}}\right)} \tag{2.12}$$

where P is the magnitude of the power loss (17 dB), $n_{0.01}$ is the dimensionless frequency at which $\Phi^2(n) = 0.01$ and w has units of dB octave^{-1} (Lyons, 2001). For $0.01 \le r_1 \le 0.3$, the roll-off of the transition region was $w \approx 17$ dB octave^{-1} and for $0.4 \le r_1 \le 0.7$, $w \approx 15$ dB octave^{-1}. This w indicates a sharp decrease in signal below the half-power frequency. The w values for $r_1 = 0.8$, 0.9, and 0.99 were 6.1, 2.2, and 2.2 dB octave^{-1}, respectively. In these cases, slow roll-off results from reduced frequency response compared to smaller dimensionless radii since the sample includes concentration fluctuations averaged across the sampling line radius. For

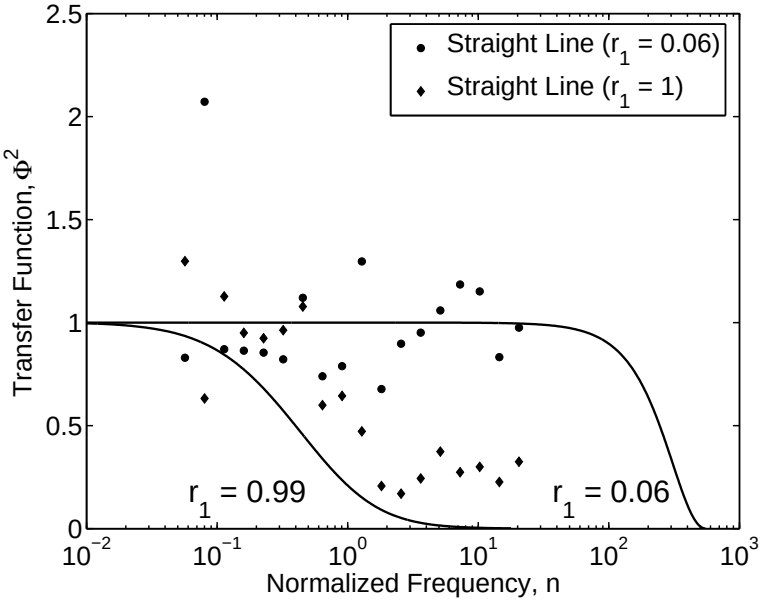

Figure 2.10: Comparison of measured and predicted isokinetic sampling transfer function. The measured transfer function is the ratio of the power spectra for the straight sampling line to the inlet section spectra. The transfer function is near one for the range of dimensionless frequencies measured, $n < 24$. Nonisokinetic sampling results in frequency response less than 50% at $n > 1$.

the dimensionless isokinetic radius used here, $r_1 = 0.06$, $w = 17$.

2.3.6. *Measured Isokinetic Sampling Concentration Transfer Function*

The power spectra was calculated using the fast Fourier transform (FFT) for the mean of each step input experiment. Transfer functions for each sampling line were then calculated from the ratio of the power spectra to that in the inlet section (see Figure 2.10) (Lenschow and Raupach, 1991). Using isokinetic sampling, $\Phi^2 \approx 1$ up to the Nyquist frequency, $f_N = f_s/2$, where f_s is the 10 Hz averaging frequency of the Q-AMS, corresponding to $n = 24$. Nonisokinetic sampling resulted in $\Phi^2 \approx 1$ for $n < 0.5$ and $\Phi^2 < 0.5$ for $n > 1$. The large magnitude values of Φ^2 observed at $n = 0.088$ were caused by the 60 s length of the step input pulses, consistent for all experiments.

The measured transfer functions are near those predicted for isokinetic and nonisokinetic sampling. Comparison of Φ^2 for $r_1 = 0.06$ shows good agreement up to the Nyquist

frequency of the Q-AMS averaging period. Nonisokinetic sampling showed good agreement with the predicted loss in frequency response due to cup-mixed sampling of the aerosol with a parabolic residence time distribution. At $n > 1$, $\Phi^2 > 0$ was likely due to turbulent mixing around the cylindrical baffle at the Q-AMS inlet.

2.4. Discussion

Particle transmission efficiencies for particles with D_p = 0.01–0.5 μm were estimated for the sampling line geometry used in the experiments above. For the isokinetically subsampled aerosol, particle transmission was > 99% through the sampling line using an analytical solution for the isokinetic region of the laminar flow (Tyree and Allen, 2004). Particle transmission for this size range was > 80 to > 99% in the isokinetic probe (Gormley and Kennedy, 1949). For comparison, particle transmission efficiency in the main flow (r_1 = 1) of a laminar sampling line is ≈ 90% for 10 nm particles and > 99% for 500 nm particles (Brockman, 2001). Transmission efficiency for diffusion losses in a turbulent flow sampling line with Re = 10000 is ≈ 75% for 10 nm particles and > 99% for 500 nm particles. Transmission efficiency for turbulent inertial losses is ≈ 94% for 500 nm particles and ≈ 94% for 10 nm particles.

The transfer function and roll-off for isokinetic sampling of a solute with Sc → ∞ was calculated for the sampling line dimensions and flow rate of the experiments above. Using the same sampling line geometry, these results can be compared with those for different designs: nonisokinetic sampling of particles and gases from laminar flow (r_1 = 1) and sampling from turbulent flow.

The transfer function for $\langle C \rangle_{\text{main}}$ of a solute with Sc → ∞, given by Equations 2.5 and 2.6, was calculated for nonisokinetic sampling from laminar flows (see Figure 2.11). The normalized half-power frequency was 0.397 and the w of the transition region was 2.1 dB octave^{-1}, which matched the results from Equations 2.11 and 2.12 for r_1 = 0.99.

The transfer functions for $\langle C \rangle_{\text{main}}$ of a solute with Sc ≈ 1 was calculated for laminar flows using Equations 2.2 and 2.4 (see Figure 2.11). The normalized half-power frequency was 1.28 and the w of the transition region was 13 dB octave^{-1}. Attenuation of $\langle C \rangle_{\text{main}}$ for solutes

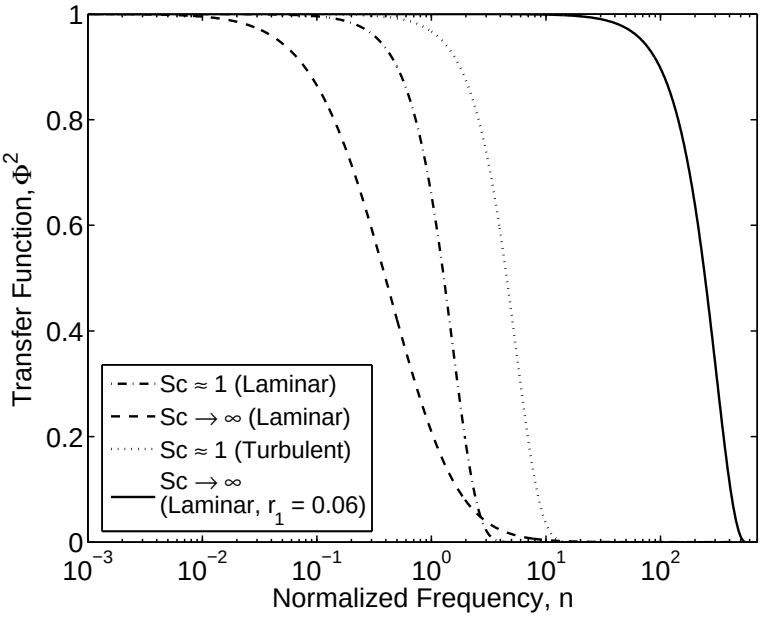

Figure 2.11: Squared transfer functions for the main flow of Sc → ∞ in laminar flow, Sc ≈ 1 in laminar flow, Sc ≈ 1 in turbulent flow, and for Sc → ∞ in the isokinetic region of a laminar flow ($r_1 = 0.06$; far right curve) versus dimensionless frequency, $n = f/f_0$.

with Sc ≈ 1 is less than that for solutes with Sc → ∞ since diffusion mitigates the effect of differential advection across the tube radius (Lenschow and Raupach, 1991). For comparison, the transfer function for $\langle C \rangle_{\text{main}}$ in turbulent flows was calculated using Equation 2.3 and the same sampling line geometry as above but using a flow rate of 78 l min^{-1}, corresponding to Re = 10000. For this design $n_{0.5} = 4.5$ and $w = 13$ dB octave^{-1}. Turbulent mixing also mitigates the effect of differential advection so that attenuation of $\langle C \rangle_{\text{main}}$ is less than that for a solute with Sc → ∞ in laminar flows.

The transfer function for $\langle C \rangle_{\text{isok}}$ for a solute with Sc → ∞ in laminar flow has improved frequency response compared to those for $\langle C \rangle_{\text{main}}$. The half-power frequency predicted for the dimensionless isokinetic radius used here, $r_1 = 0.06$, was 2.5×10^2. This result is more than 2.5 orders of magnitude higher than the half-power frequency for nonisokinetic sampling and more than 1.5 orders of magnitude higher than the result for turbulent flow given above. The frequency roll-off for $r_1 = 0.06$ is 87% steeper than that for nonisokinetic sampling and 21%

steeper than that for turbulent flow. Isokinetic subsampling reduces the effect of attenuation caused by differential advection since the velocity profile in the isokinetic region resembles plug flow. These results indicate that isokinetic subsampling from laminar flows is desirable for solutes with $Sc \rightarrow \infty$, such as aerosol particles.

2.5. Conclusions

The attenuation of particle concentration fluctuations from isokinetically sampled laminar flow was experimentally measured using the EC mode of the Q-AMS. Truncation of the Q-AMS signal by the data acquisition program in EC mode resulted in loss of particle size data and a factor of approximately 30 decreased sensitivity to NH_4NO_3 aerosol mass. The EC mode signal likely resulted from indirect observation of semivolatile aerosol condensation and revolatilization. In EC mode the signal response increased linearly with NH_4NO_3 aerosol mass and had a limit of detection of $\approx 0.33\ \mu g\ m^{-3}$. The mechanism of mass detection in the EC mode suggests that similar behavior may be observed for other semivolatile aerosol species, including organic carbon.

Step changes in particle concentration were introduced to laminar flow sampling lines in order to measure the attenuation of concentration fluctuations in isokinetically sampled flow. The measured transit times for particles in the isokinetic region agree with the calculated values, indicating that the laminar flow was fully developed and that the isokinetic probe was aligned near the centerline.

Attenuation time constants, τ, were measured to be $\tau = 4.5 \times 10^{-7} \pm 0.12$ s for the inlet section, $\tau = 0.10 \pm 0.12$ s for the straight line, and $\tau = 0.15 \pm 0.08$ s for the straight line with a size-selective cyclone. The τ for the straight line with the cyclone corresponds to a dimensionless half-power frequency $n_{0.5} = 24$. This exceeds the recommended frequency response of ≈ 10 Hz for turbulent flux measurements using the eddy correlation method. Nonisokinetic sampling from the 8.3 m sampling line, simulated using a cylindrical baffle 5 cm upstream of the isokinetic probe, resulted in $\tau = 0.67 \pm 0.07$ s.

A transfer function for $\langle C \rangle_{isok}$, applicable to the isokinetic region of a subsampled

laminar flow was calculated by numerically integrating the transfer function for particles with $Sc \rightarrow \infty$ in laminar flow (Lenschow and Raupach, 1991). The solution matches the main flow conditions for $r_1 = 1$. Attenuation of concentration fluctuations is smaller in the isokinetic region than in the main flow. A frequency response of 50 Hz was theoretically predicted for isokinetic sampling from the sampling line used here. The frequency response of the isokinetically sampled aerosol was predicted to be three orders of magnitude higher than the main flow values. The isokinetic transfer function can also be used to evaluate the frequency response of isokinetic systems designed for eddy correlation measurements.

The measured transfer functions were calculated from the ratio of the power spectrum of the Q-AMS signal measured for each experiment to that of the inlet section. The frequency response of isokinetically sampled laminar flow was measured to be an order of magnitude greater than the main flow averaged value. This result is limited by the averaging period of the Q-AMS and higher frequency response was predicted.

From the experimental measurements, it is possible to speculate about humidity conditioning of isokinetically sampled particles from laminar flows. Gaseous species, such as water vapor, have $Sc \sim 1$, several orders of magnitude smaller than Sc for particles. The increased diffusivity mitigates the effect of differential advection. Thus, attenuation of gas concentration fluctuations measured in the main flow has been predicted and measured to be an order of magnitude lower than attenuation of particle concentration fluctuation (Lenschow and Raupach, 1991; Massman, 1991). In the isokinetic region, $r_1 = 0.06$, the attenuation time constant is four orders of magnitude larger than in the main flow, $r_1 = 1$ (see Figure 2.11). Using isokinetic sampling for eddy correlation aerosol flux measurements, water vapor concentration fluctuations are sufficiently damped relative to the particles so that the aerosol is conditioned to a nearly constant relative humidity as it passes through a sampling line. This result has a practical application since the eddy flux correction for water vapor concentration fluctuations (Vong *et al.*, 2004) can be ignored.

Isokinetic sampling of laminar flow is a significant improvement for aerosol eddy cor-

relation measurements. This setup reduces inertial particle losses by maintaining a laminar flow profile and reduces diffusional losses by subsampling from the centerline of the main flow. Isokinetic sampling of laminar flow provides a method for measurement of particulate concentrations with sufficient frequency response to determine atmosphere-land fluxes from eddy correlation measurements.

2.6. Nomenclature

Variables

C	concentration
D	diameter of the main flow tube
D_p	particle diameter
D_{va}	particle vacuum aerodynamic diameter
$\mathcal{D}$	diffusion coefficient
$\mathcal{D}_v$	virtual axial diffusion coefficient
f	frequency
f_0	flow frequency, U/L
f_N	Nyquist frequency
f_s	sampling frequency
i	imaginary unit
L	length of sampling tube to isokinetic inlet
L_e	length of the entrance region for laminar flow
m/z	mass-to-charge ratio
n	dimensionless frequency
$n_{0.5}$	dimensionless half-power frequency
N	normalized signal
P	magnitude of signal power loss
Pé	Péclet number, $RU/\mathcal{D}$ = ReSc
r	dimensionless radial position, x/R
r_1	dimensionless radius of isokinetic sampling probe, x_1/R
R	radius of the main flow tube
Re	Reynolds number, $2\,\rho\,U\,R/\mu$
S	Q-AMS signal
Sc	Schmidt number, $\mu/\rho\mathcal{D}$

t	time
t_c	centerline transit time
t_0	solenoid opening time
t_p	particle detection time
t_r	transit time at r
ToF	time-of-flight
$u(r)$	gas velocity as a function of radial position
U	average gas velocity of the bulk flow
$\dot{V}$	volumetric flow rate
w	roll-off of the transition region
x	radial position
x_1	radius of isokinetic sampling probe
z	axial direction

Subscripts

in	inlet value
isok	isokinetic region value
main	main flow value
out	outlet value

Greek Symbols

δ	particle spreading time
Δt	transit time
μ	viscosity
ρ	density
τ	attenuation time constant
ϕ	frequency response
Φ^2	concentration transfer function
ω	frequency in radians per second

Ω dimensionless frequency

Operators

$< >$ mixing-cup average

$\overline{( )}$ mean

3. MEASUREMENT OF SPECIATED FINE PARTICLE DEPOSITION USING EDDY CORRELATION MASS SPECTROMETRY

3.1. Introduction

Dry deposition is a mechanism for the removal of fine particles from the atmosphere. From a simple mass balance perspective, the concentration of particles in the atmosphere is the integrated difference between the rate of input into the system and the rate of removal from the system. The atmospheric lifetime of fine aerosol particles is on the order of days to weeks (Seinfeld and Pandis, 1998). Eventually, particles are removed from the atmosphere by deposition to the earth's surface. The chemical components associated with fine particles introduce toxic and nutrient materials to receptor ecosystems where they interact with water, soil, and plants. Atmospheric aerosols represent a vector for the transport of anthropogenic pollution downwind of their source. Thus, chemically speciated measurements of fine particle removal via dry deposition are necessary to inform air pollution models and determine environmental impacts.

The dry deposition flux is usually assumed to be proportional to the concentration

$$F = -v_d c \tag{3.1}$$

where v_d is known as the deposition velocity (Chamberlain and Chadwick, 1953; Sehmel, 1980). By convention the deposition velocity is positive for a downward flux ($F < 0$). The deposition velocity represents the cumulative effect of the physical processes responsible for dry deposition including turbulent transport, Brownian diffusion, and surface interaction (Slinn, 1982). Particle deposition velocities are then implicitly dependent on the atmospheric conditions and the particle diameter, D_p. Model predictions for particle v_d are $\approx$ 0.08–0.3 cm s^{-1} for 0.1 μm particles and $\approx$ 0.2–0.4 cm s^{-1} for 1.0 μm particles, where the range of estimates reflects the effect of surface roughness (Sehmel, 1980).

The micrometeorology-based eddy correlation method is one approach to measure v_d directly using fast-response sensors. Turbulent fluid motion transports energy, gases, and particulate matter, so that the turbulent fluctuations of the vertical wind velocity, w, and the scalar quantity, c, measured above the surface are used to calculate the eddy flux as the

covariance

$$F = \overline{w'c'} \tag{3.2}$$

where primes denote deviation from the mean and the overbar denotes a mean over an averaging period (Wesely *et al.*, 1977; Sievering, 1982; Wesely *et al.*, 1985; Gallagher *et al.*, 1997, 2002; Vong *et al.*, 2004). Application of the eddy correlation method is limited to situations of stationary, homogeneous turbulence, mass conservation, and dynamically stable conditions in the boundary layer (Kaimal and Finnigan, 1994; Foken and Wichura, 1996). This method has been widely used to measure momentum (Reynolds stress), sensible heat, latent heat, and trace gas fluxes (Dyer and Pruitt, 1962; Hicks, 1970; Grimmond *et al.*, 1996; Schmid *et al.*, 2000, 2003). Fine particle deposition velocity is defined as the normalized aerosol dry deposition flux

$$v_d = \frac{-\overline{w'c'}}{\overline{c}} \tag{3.3}$$

The deposition velocity measured using the eddy correlation method includes the turbulent transport and diffusion components of dry deposition, but excludes gravitational settling (Gallagher *et al.*, 2002).

Experimental measurements of particle deposition velocities have been made using the eddy correlation method. Wesely *et al.* (1977) used a particle charger to measure nonspeciated, small particle (D_p = 0.05–0.1 μm) deposition velocities of 0.12–1.2 cm s^{-1}. Wesely *et al.* (1983) and Wesely *et al.* (1985) measured particulate sulfur dry deposition velocities using a flame photometric detector (FPD). Average daily deposition velocities of 0.22 ± 0.06 cm s^{-1} were reported for particles in the size range 0.01 to 2 μm, with large run-to-run variability, attributed to noise in the FPD signal (Wesely *et al.*, 1985).

Optical particle counters (OPCs) have been used to measure size-resolved particle deposition by eddy correlation (Sievering, 1982; Katen and Hubbe, 1985; Gallagher *et al.*, 1997; Buzorius *et al.*, 1998; Gallagher *et al.*, 2002; Vong *et al.*, 2004). In this method, sampled air is passed through a continuous wave laser. Particle size is determined from the amount of light scattered by calibration particles, usually polystyrene latex spheres. Since ambient aerosol particles are optically different from calibration particles, particle sizes determined from OPCs

are approximate (Hering and McMurry, 1991). Particle size is also affected by water uptake at varying ambient humidity. Vong *et al.* (2004) estimated that hygroscopic growth accounted for approximately half of the deposition flux measured using an OPC.

Deposition velocities of accumulation mode particles (D_p = 0.1–1.0 μm) measured over a forest show an order of magnitude uncertainty from throughfall, eddy correlation, and other measurements Gallagher *et al.* (1997). For example, measurements for particles with a diameter of 500 nm are in the range 0.3–5 cm s^{-1}. Existing deposition models predict deposition velocities for 500 nm particles in the range 0.04–0.1 cm s^{-1}, since gravitational settling and Brownian diffusion are less efficient and deposition is thought to be mostly due to turbulent transport. These results suggest that our current understanding of the physical and chemical mechanisms that contribute to dry deposition is insufficient to predict dry deposition fluxes in atmospheric models (Wesely and Hicks, 2000; Gallagher *et al.*, 2002).

Here we demonstrate a new method, eddy correlation mass spectrometry (ECMS), to measure speciated fine particle deposition velocities. The eddy correlation technique was coupled with fast response measurements of aerosol composition using an Aerodyne Quadrupole Aerosol Mass Spectrometer (Q-AMS) (Jayne *et al.*, 2000) in order to directly measure chemically speciated fine particle deposition velocities. The Q-AMS measures the concentration of non-refractory chemical species in ambient aerosols. An eddy correlation program for the Q-AMS software was used to save aerosol concentration data at ≈ 10 Hz. Measurements of speciated fine particle deposition velocities over an agricultural field using the ECMS approach are presented.

3.2. Methods

3.2.1. *Site Description*

A field experiment was conducted on the Salt River Pima-Maricopa Indian Community (SRPMIC) immediately adjacent to the Phoenix, Arizona, metropolitan area. The Salt River site (33°32’ N, 111°49’ W, elevation 414 m) was situated in an agricultural area, which is gently sloped for irrigation. Broccoli was cultivated during the experiment (16 January to 4 February

2005) and had grown to a mean height of 0.5 m. The usual direction of daytime wind flow is from the south to southwest. A 5 m instrument tower was located at the north east corner of the field adjacent to a single-family house, accessible by a dirt road to the east of the agricultural field (see Figure 3.1). The house was approximately 9×18 m and approximately 10 m from the instrument tower. Several mature trees, with height of $\approx$ 5–10 m, surrounded the house, including one approximately half way between the house and the instrument tower. Irrigation canals bordered the field to the north and east with open desert beyond the canals and access road. The quadrant southwest of the sampling point consisted of mature broccoli over a 500×700 m area with crops beyond this in the usual wind direction. Minor dirt roads, used ocassionally by agricultural workers, are located along the edges of this area. The main public road for the site is 1.5 km to the south. Major freeways, which separate the rural landscape that dominates the SRPMIC from the metropolitan area, are 5.6 km and 8.1 km to the west and south, respectively.

Synoptic weather conditions during the study were mostly clear and sunny. Trace amounts of rain were measured at a weather station 6.4 km southwest of the experiment site in the early morning of 24 January. Cloudy skies were prevalent and rain was recorded during the day on 26, 27, and 29 January. All periods of precipitation were excluded from subsequent data analysis. Flood irrigation was used on 19 January, beginning at 17:00 and ending later that night. The soil underneath the crop canopy remained wet during sampling on 20 January. Sections of the broccoli crop were hand harvested (flower heads only) on 26–30 January. Sunrise and sunset were approximately 0730 and 1800, respectively, during the experiment.

3.2.2. *Tower Instrumentation*

A 3-D sonic anemometer (SATI-3K, Applied Technologies, Inc., Longmont, Colorado) was used to measure air flow above the field (see Figure 3.2). The “K” style sonic anemometer was designed to minimize probe-induced flow distortion errors (Kaimal *et al.*, 1990). The sonic anemometer has a path length of 15 cm, and reported 10 Hz mean measurements of the three

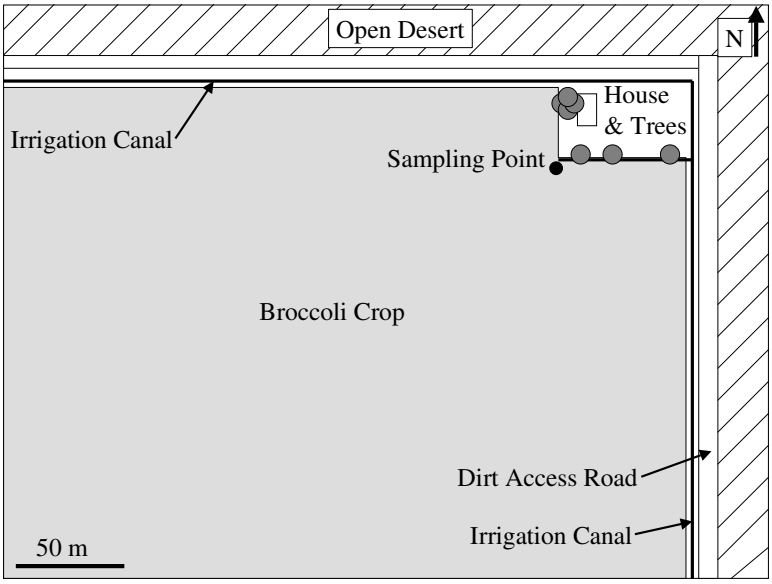

Figure 3.1: Aerial schematic of the Salt River experiment site. The instrument tower was located near the corner of a 500 x 700 m broccoli field, adjacent to a single-family home with trees. Access to the area was by dirt road along the eastern edge of the field. Irrigation canals bordered the field to the north and east. The agricultural area was surrounded by open desert to the north and east.

Figure 3.2: Photo, facing west, of the eddy correlation equipment at the Salt River experiment site. The sonic anemometer was mounted at a height of 4.7 m above the field on a 2 m boom. The infrared gas analyzer (IRGA) was mounted approximately 0.2 m behind and at the same height as the sonic anemometer. Air was sampled through a size-selective cyclone mounted next to the IRGA.

wind components (u, v, and w) with a resolution of ± 0.03 m s^{-1} and sonic temperature, T, with a resolution of ± 0.1°C. The anemometer was calibrated immediately before use to zero the probe sensors according to the manufacturer's instructions.

An open path infrared gas analyzer (IRGA) (LI-7500, Li-Cor, Inc., Lincoln, Nebraska) was used to measure gas phase CO_2 and H_2O concentrations (see Figure 3.2). The IRGA has a 12.5 cm path length and updates the analog output at 300 Hz with a 16 bit resolution for each channel. The IRGA output was recorded at 100 Hz using a 200 kHz data acquisition board (Model PCI-6024E, National Instruments, Austin, TX) and a custom Java data acquisition system. A two-point calibration of the IRGA was performed before use according to the manufacturer's instructions. Ultra-high purity nitrogen was used to zero the instrument for CO_2 and H_2O. A certified calibration mixture of CO_2 in air was used to determine the calibration slope for CO_2. Filtered air, at a known relative humidity, was used to determine the calibration

slope for H_2O. The calibration was checked after the end of the experiment and no change to the calibration was needed.

Air was sampled through a size-selective cyclone (Model 2000-30EN, URG, Chapel Hill, NC) connected to an insulated copper sampling line with inner diameter 1.1 cm (see Figure 3.2). The volumetric flow rate through the sampling line was measured to be $\dot{V} = 10.8$ l min^{-1} using a calibrated glass tube rotameter. A constant volumetric flow rate was maintained using a 0.045 cm diameter critical orifice at the sampling line outlet. The cyclone had a design 50% cutpoint diameter of 2.2 μm at this flow rate. The Reynolds number, $\mathrm{Re} = D_{\mathrm{tube}} v_{\mathrm{air}} / \nu_{\mathrm{air}}$, in the sampling line was 1400. Laminar flow was chosen to reduce inertial wall losses and allow for isokinetic sampling of the aerosol. This design reduced diffusional particle losses (Tyree and Allen, 2004) and reduced attenuation of particle concentration fluctuations (see Chapter 2).

Instrumentation was mounted near the top of the instrument tower. The sonic anemometer was mounted at a height of 4.7 m on a 2 m boom oriented toward the south. The IRGA was mounted on a separate boom approximately 0.2 m behind and at the same height as the sonic anemometer. The aerosol inlet was mounted 0.2 m behind and slightly below the vertical wind velocity probes of the sonic anemometer.

3.2.3. *Quadrupole Aerosol Mass Spectrometer (Q-AMS)*

The aerosol flow was isokinetically sampled into the Q-AMS using a probe with an inner diameter of 0.068 cm. The isokinetic sub-sample included aerosol from the centerline of the main sampling line flow to the dimensionless radius $r = 0.06$, where $r = x/R$, x is the radius of the isokinetic probe, and R is the radius of the main sampling line. The design Q-AMS inlet flow rate was 1.5 cm^3 s^{-1}, resulting in a Reynolds number of 160 in the isokinetic probe. In the Q-AMS aerosol particles were focused by an aerodynamic lens and the particle beam was modulated by a chopper wheel, which rotated at $\approx$ 100 Hz (Jayne *et al.*, 2000; Jimenez *et al.*, 2003; Canagaratna *et al.*, 2007). The particle time-of-flight through a 0.39 m vacuum chamber was used to measure the vacuum aerodynamic diameter, D_{va}. The aerosol was directed onto a resistively heated surface and the non-refractory (NR) components of the

aerosol were vaporized at ≈ 450 °C. The vapor was then ionized by electron impact using an ionizer filament, positioned along one edge of the ionization region housing, which also provided radiative heating. Molecular ions were filtered by a quadrupole mass spectrometer which output a signal proportional to the concentration of ions at specified mass-to-charge ratios, m/z.

The Q-AMS was operated in two programs: ambient composition and eddy correlation sampling. During ambient composition sampling, the Q-AMS was operated in the alternating mode in which five minute averages of mass spectrum (MS) and particle time-of-flight (PToF) data were saved. This sampling program is commonly used to characterize the composition and size distribution of ambient fine particles (e.g. Jimenez *et al.*, 2003; Canagaratna *et al.*, 2007).

The Q-AMS was calibrated before the start of the experiment using the ambient sampling program and published procedures (Jayne *et al.*, 2000; Allan *et al.*, 2003b). The quadrupole filter and the gain of the electron multiplier were calibrated to optimize instrument response. The electron multiplier was re-calibrated approximately every 5 days during the experiment. The ionization efficiency of nitrate was measured before and approximately every 5 days during the experiment to determine the instrument response to a known input. The time-of-flight calibration curve for the Q-AMS was measured in the laboratory using five sizes (46±2 nm, 102±3 nm, 299±6 nm, 499±5 nm, and 903±9 nm) of calibrated polystyrene latex (PSL) spheres (Duke Scientific Corp.). The particle velocity curve for this Q-AMS instrument has a lower slope, thus a reduced particle size resolution, compared to the original design for the Q-AMS.

The new eddy correlation program (EC mode) was designed to collect concentration and time-of-flight data for one m/z and generate an external square wave trigger every 10 chopper cycles, ≈ 10 Hz. The EC mode data acquisition program erroneously truncated the nominal time-of-flight scale, which excluded PToF times less than 1 ms (see Chapter 2). The EC mode instead recorded indirect signal from condensation and revolatilization of material in the Q-AMS vaporization region. Despite erroneous data acquisition, the EC mode demonstrated a

linear response to mass loading of NH_4NO_3 particles used for calibration. For calibration particles (350 nm) the ratio of the EC mode sensitivity to that of the PToF mode was 0.03. The limit of detection was ≈ 0.33 μg m^{-3} compared to ≈ 0.05 μg m^{-3} for PToF data. Because the Q-AMS signal is not size-resolved in EC mode the sum of the EC mode signal over the recorded time-of-flight range was used in all subsequent data analysis. The consequences of these limitations for deposition velocity measurements using the Q-AMS EC mode will be addressed below.

In EC mode the Q-AMS software was synchronized with the sonic anemometer using the square wave trigger signal. Serial data from the sonic anemometer were saved to the Q-AMS data acquisition computer at the same rate as the aerosol concentration data. The square wave trigger signal was saved with the IRGA concentration data using the Java data acquisition system. Since each square wave trigger pulse corresponds to one 10 Hz average time-of-flight spectrum saved by the Q-AMS, the trigger signal was used to synchronize the Q-AMS and IRGA measurements with the sonic anemometer measurements.

The Q-AMS operating schedule was to measure the ambient aerosol each morning for 30 minutes at approximately 0800 using the ambient composition program. Eddy correlation data were then collected from approximately 0900 to 1400, followed by 30 minutes of ambient aerosol sampling. After another period of eddy correlation sampling from approximately 1500 to 1800, 30 minutes of ambient aerosol data were collected. Then the Q-AMS was calibrated (only on the dates noted above) and Q-AMS sampling was suspended overnight. Sonic anemometer and IRGA data were collected continuously, including overnight.

3.2.4. *Eddy Correlation Data Analysis*

Calculation of turbulent fluxes requires measurement of signals over 15–30 minutes to fulfill the statistical requirements for time series analysis (Foken and Wichura, 1996). The averaging period for eddy correlation calculations was determined using an ogive function (cumulative integral of the cospectrum) (Oncley *et al.*, 1990; Foken and Wichura, 1996). This function converges to a constant value at a frequency which can be converted to an averaging

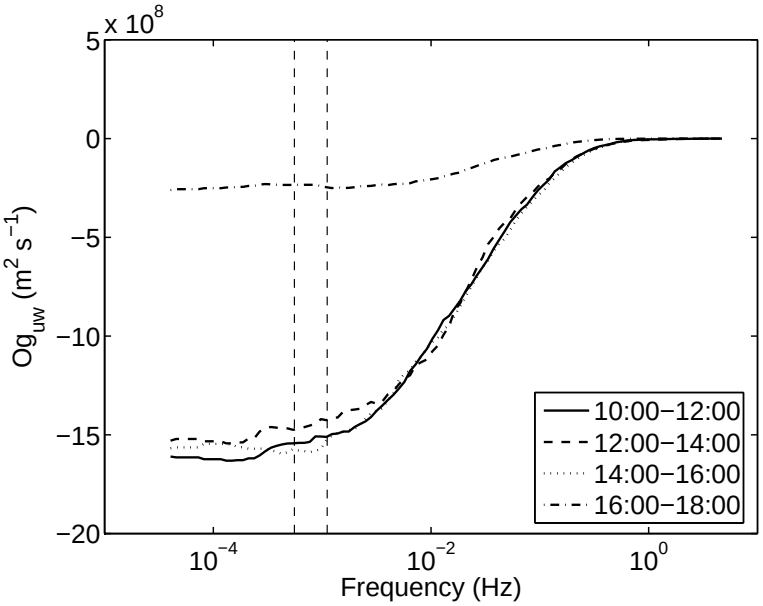

Figure 3.3: Momentum flux ogives (cumulative integral of the cospectrum) measured at the Salt River experimental site on 27 January 2005. Each line represents a 2 h period of measurements. The vertical dashed lines at $f = 1.1 \times 10^{-3}$ and $f = 5.6 \times 10^{-4}$ Hz correspond to averaging periods of 15 and 30 minutes, respectively.

period for flux measurements. Deviations up to 10% of the total are tolerated due to the variability of turbulent spectra.

Momentum flux ogives, Co_{uw}, were calculated for 2 h subsets of daily data to determine the averaging period. The ogives typically converge to 90% of the total between $f = 1.1 \times 10^{-3}$ and $f = 6 \times 10^{-4}$ Hz, corresponding to averaging periods of 15 and 30 minutes, respectively. For example, the momentum ogive for 1600–1800 on 27 January was constant for frequencies less than $f \approx 1 \times 10^{-3}$, corresponding to an averaging period of 15 minutes, (see Figure 3.3). In other cases, the ogive converges at $f \approx 6 \times 10^{-4}$, corresponding to an averaging period of 30 minutes (1400-1600). In general for this experiment, the eddy correlation results calculated using 15 and 30 minute averaging periods are within the 10% tolerance of spectra variability. An averaging period of 15 minutes was used here to increase the fraction of available data for analysis and improve the statistical validity of the results.

The raw data were corrected for orientation and leveling of the sonic anemometer using

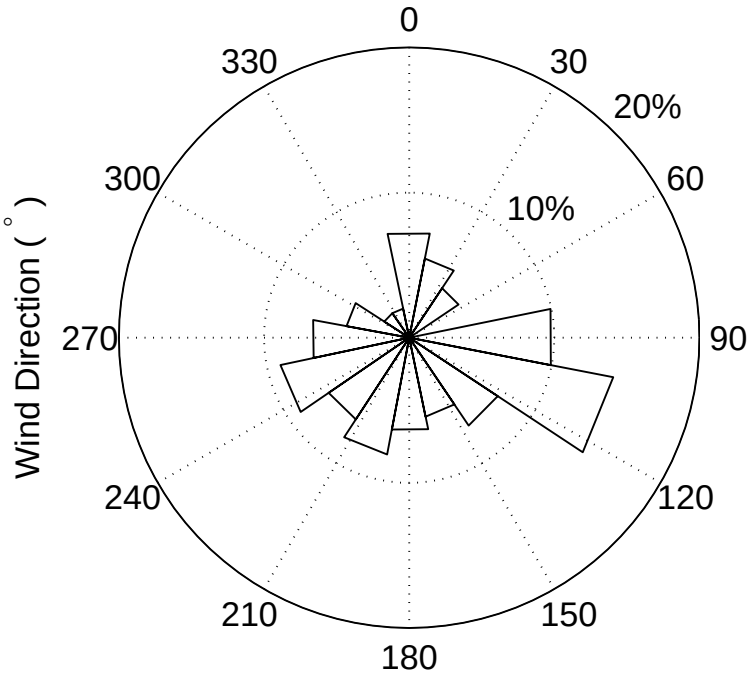

Figure 3.4: Wind rose showing fraction of 15 minute period wind direction during EC mode sampling at the Salt River site. Air flowed over the crop from the southwest quadrant during approximately 25% of the measurement periods.

a coordinate rotation of the three-dimensional wind velocity measurements (McMillen, 1988). The coordinate rotation is done such that $\overline{v} = 0$, aligning u with the mean horizontal wind vector, and $\overline{w} = 0$. This rotation procedure resulted in a coordinate system aligned with the mean wind vector and perpendicular to the underlying surface for each averaging period. Air flowed over the crop from the southwest quadruant during approximately 25% of the EC mode sampling periods (see Figure 3.4). The data were segregated by wind direction and only EC mode data collected during air flow over the field from the southwest quadrant (175–250°) were subsequently analyzed. This procedure excluded periods of air flow from the north and east, which were likely disturbed by the house and trees near the instrument tower. The homogeneous fetch-to-height ratio was > 100 for the retained sampling periods.

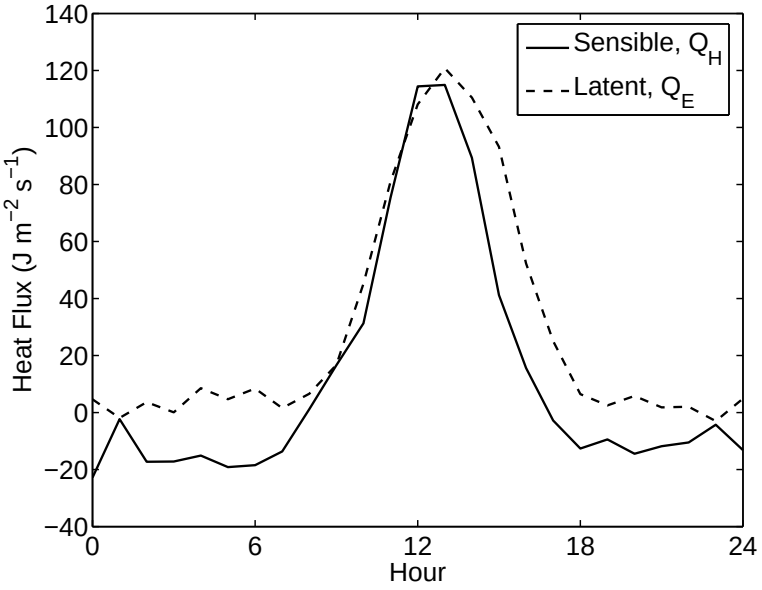

Figure 3.5: Hourly average sensible (Q_H) and latent (Q_E) heat fluxes for the entire study. During the day most of the energy is used for evaporation of water ($Q_E > Q_H$); at night sensible heat is lost to the surface ($Q_H < 0$) and little energy is available for evaporation ($Q_E \approx 0$).

3.3. Results

3.3.1. *Micrometeorological Characterization of the Experimental Site*

Sensible heat fluxes, Q_H, were calculated using standard eddy correlation equations for 15 minute averaging periods from rotated wind vectors and measured sonic temperatures (Stull, 1988; Kaimal and Finnigan, 1994). The hourly average sensible heat fluxes for the entire study exhibit the expected diurnal pattern (see Figure 3.5). Heat was lost to the surface ($Q_H < 0$) between sunset and sunrise, followed by increasing upward heating to a peak of about 115 J m^{-2} s^{-1} at midday and a return to negative heat fluxes at night.

Latent heat fluxes, Q_E, were calculated using standard eddy correlation equations for 15 minute averaging periods from the vertical wind velocity and IRGA measurements of the specific humidity. The lag time between these data streams is expected to be ≈ 0.23 s, due to a fixed throughput delay in the IRGA software and negligible lag time due to instrument separation. The mean delay time, calculated from a lagged correlation analysis to be 0.2 s, was

used. The latent heat flux was near zero during early morning and nighttime hours and peaked at about 120 J m^{-2} s^{-1}at midday. The Bowen ratio ($\beta = Q_H/Q_E$) was < 1 during the day, since most of the solar energy was used for evaporation above the irrigated crop. At night, sensible heat was lost to the surface ($Q_H < 0$) and very little energy was available for evaporation ($Q_E \approx 0$). These results provide confirmation that the site is suitable for flux measurements.

Eddy correlation results were screened for nonstationary periods by comparing F_M and Q_H calculated for each averaging period to the fluxes calculated for six sub-periods. Nonstationary periods were identified if the mean momentum or sensible heat flux of the six subperiods differed from the 15 minute calculated flux by more than 30% (Foken and Wichura, 1996). Stationary turbulence was measured during approximately 33% of the data averaging periods during this study.

Friction velocities, u_*, and Obukhov lengths, L, were calculated from the micrometeorological measurements (Stull, 1988; Kaimal and Finnigan, 1994). The roughness length was predicted using measurements of wind speed and friction velocity made during neutral stability ($|L| > 1000$ m) with wind speeds greater than 2 m s^{-1} (see Chapter 1) (Stull, 1988; Schmid *et al.*, 2000). The mean value was $z_o = 0.10 \pm 0.03$ m for measurements of air flow over the field. This estimate is in agreement with suggestions that $z_o \approx 0.3h$, where $h \approx 0.5$ m is the height of the vegetative canopy (Kaimal and Finnigan, 1994).

Under near-neutral stability, the logarithmic wind profile predicts that the friction velocity increases linearly with wind speed with a slope $\approx k \ln(z/z_o)^{-1}$, where $k = 0.4$ is the von Karman constant. Using the value $z_o = 0.10$ predicted for the Salt River site, the log wind profile gives

$$u_* = 0.10U \tag{3.4}$$

where U is the mean wind speed. A linear regression of the friction velocity and wind speed measurements yielded $u_* = 0.10U + 0.01$, in good agreement with the log wind relationship (see Figure 3.6).

Averaged data were segregated by atmospheric stability class using the stability pa-

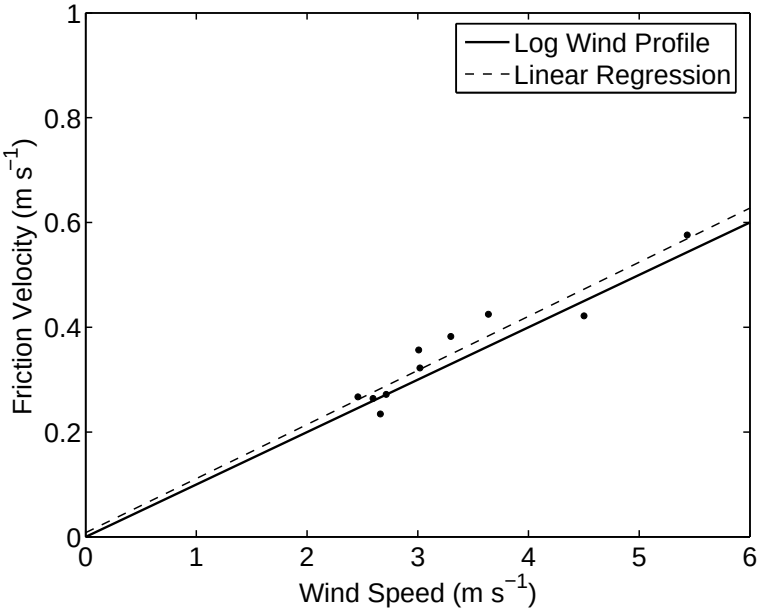

Figure 3.6: Measurements of friction velocity and wind speed under near-neutral conditions.

rameter, L^{-1}. Stable or near neutral conditions, $L^{-1} \geq 0$, predominated from sunset to sunrise when buoyancy is negative. For example, the atmosphere was stable from midnight to approximately 0730 on 30 January (see Figure 3.7). Positive buoyancy during the day resulted in unstable conditions, $L^{-1} < 0$. On 30 January, the atmosphere began to stabilize at approximately 1800. Approximately 80% of the daytime eddy correlation sampling periods, typically 0800–1800, were during unstable atmospheric conditions.

3.3.2. *Sampling Line Lag Time*

Ambient air samples were drawn from the cyclone inlet through the sampling line into the Q-AMS. Aerosol transit times in a laminar flow sampling line were measured in the laboratory by introducing step changes of concentrations into the sampling line and measuring the aerosol arrival time (see Chapter 2). The transit time for the sampling line used in this experiment was measured in the laboratory to be 4.5 ± 0.2 s.

The lag between the aerosol signal measurements and the sonic anemometer measurements was verified by calculating the covariance of the vertical wind velocity, w, and the sum of the Q-AMS signal over the recorded time-of-flight range, S, for lag times between 3.0–5.0 s

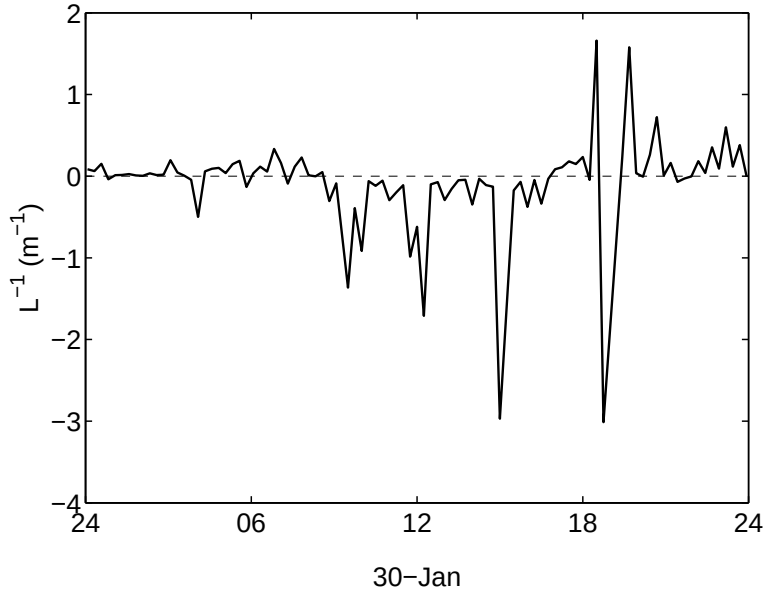

Figure 3.7: Atmospheric stability, L^{-1}, measured on 30 January 2005. The atmosphere was unstable, $L^{-1} < 0$, during daytime aerosol measurement periods. Starting after sunset, stable or near neutral $L^{-1} \geq 0$, atmospheric conditions were typical through the night.

in 0.1 s time steps (Fan *et al.*, 1992; Munger *et al.*, 1996). For each 15 minute averaging period, a minimum in the covariance was found at a lag time corresponding to the aerosol transit time (see Figure 3.8). The lagged correlation analysis resulted in a mean transit time of 4.2 s, however, the range of values was large (≈1 s) and the magnitude of the covariance minimum was often small compared to the mean of the covariance values. Thus, the transit time of 4.5 s measured in the laboratory was used here. This transit time was accounted for in subsequent data analysis by shifting the aerosol signal time series measurements with respect to the sonic anemometer measurements.

3.3.3. *Spectral Characteristics*

Cospectra of the vertical wind velocity and air temperature were calculated for periods of continuous mesurements (Stull, 1988). The cospectra indicates that most of the sensible heat flux was carried by eddies with frequencies in the range 0.01–0.1 Hz (see Figure 3.9). At frequencies of 0.1–5 Hz, in the inertial subrange, the cospectra decayed at a constant rate of $f^{-7/3}$. The cospectra of w and S showed similar characteristics (see Figure 3.9). There

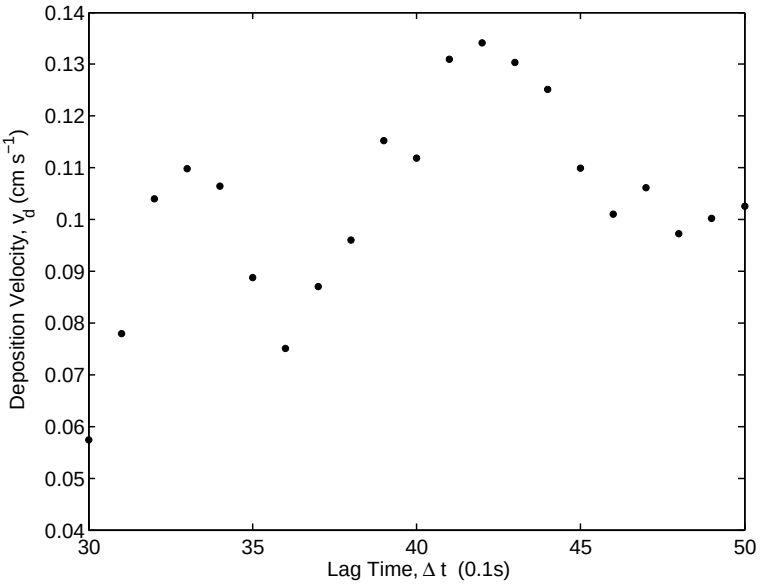

Figure 3.8: Lagged correlation analysis for a 15 minute period on 30 January 2005. The covariance of vertical wind velocity, w, and Q-AMS signal, S, peaked at a lag time of 4.2 s, corresponding to the transit time of particles in the sampling line.

was minimal loss of $< w, S >$ cospectral energy at high frequencies compared to $< w, T >$. Methods for correcting attenuation of high frequency losses have been used for trace gas flux measurements (Moore, 1986; Horst, 1997; Massman, 2000; Massman and Lee, 2002; Shimizu, 2007). These correction algorithms are not generally applicable to aerosol flux measurements since the attenuation of concentration fluctuations measured over the entire sampling line radius increases with decreasing diffusivity and fine particle diffusivities can be more than four magnitudes smaller than gas diffusivities (Lenschow and Raupach, 1991; Buzorius *et al.*, 1998). The aerosol was isokinetically sub-sampled from the centerline of the main sampling line flow to the dimensionless radius $r = 0.06$, which mitigates temporal spreading as a result of differential advection. This technique reduced attenuation of fine particle concentration fluctuations to less than 1% at 5 Hz (see Chapter 2). Thus, no correction for attenuation of high frequency components of the flux was applied here.

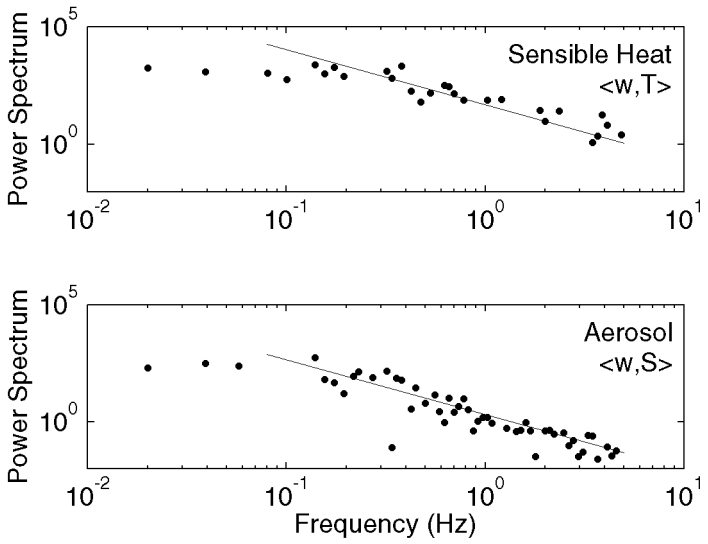

Figure 3.9: Cospectra of sensible heat (top) and aerosol flux (bottom) on 30 January 2005. The spectra peak at about 0.1 Hz for both scalars, indicating the sampling of the aerosol eddy flux scale by the ECMS system. The lines are the -7/3 power law expected for scalar flux cospectra.

3.3.4. *Fine Particle Deposition Velocities*

Synchronized sonic anemometer and Q-AMS eddy correlation mode data were collected during thirteen days of the Salt River experiment (see Table 3.1). The molecular ions monitored by the Q-AMS, m/z = 30, 43, and 64, were representative ion fragments of non-refractory nitrate (NO^+), organic ($C_3H_7^+$ or $C_2H_3O^+$), and sulfate (SO_2^+) aerosols, respectively. The ion fragments were selected based on the chemical composition of typical urban aerosols and the environmental relevance of these aerosol species (see Chapter 1).

Time series measurements of w and S were shifted to account for the lag time of the aerosol in the sampling line. Covariances, $\overline{w'S'}$, and means of the Q-AMS signal, $\overline{S}$, were then calculated for 15 minute averaging periods. The $\overline{S}$ typically increased throughout the morning and peaked near midday.

Deposition velocities were calculated for 15 minute averaging periods using Equation 3.3, where S represents the concentration of the aerosol species monitored. Application of wind direction and stationary criteria resulted in 16 periods for which measurement con-

Table 3.1: Eddy Correlation Data Collected During the Salt River Experiment.

Date	Start Time	End Time	m/z (Ion fragment)	Aerosol Species
18 Jan	1030	1800	30 (NO^+)	NR Nitrate
19 Jan	1215	1745	30 (NO^+)	NR Nitrate
20 Jan	0945	1815	30 (NO^+)	NR Nitrate
21 Jan	0915	1745	30 (NO^+)	NR Nitrate
22 Jan	1200	1530	30 (NO^+)	NR Nitrate
23 Jan	1500	1730	30 (NO^+)	NR Nitrate
24 Jan	1230	1830	30 (NO^+)	NR Nitrate
29 Jan	0930	1145	43 ($C_3H_7^+$)	NR Organic
30 Jan	0930	1900	43 ($C_3H_7^+$)	NR Organic
31 Jan	1000	1800	43 ($C_3H_7^+$)	NR Organic
01 Feb	0745	1845	30 (NO^+)	NR Nitrate
03 Feb	0730	1800	64 (SO_2^+)	NR Sulfate
04 Feb	0945	1215	30 (NO^+)	NR Nitrate

ditions were considered valid. Nine measurements of nitrate aerosol v_d during the first week of the experiment were in the range -0.21 to 0.24 cm s^{-1}, with a mean of 0.04 cm s^{-1}. One measurement on the morning of 04 February resulted in v_d = -0.61 cm s^{-1}. Three measurements of organic aerosol v_d were available from 30 January. These were in the range -0.05 to 0.20 cm s^{-1}, with a mean of 0.05 cm s^{-1}. Three measurements of sulfate v_d on 03 February were in the range -0.45 to 0.63 cm s^{-1}, with a mean of -0.01 cm s^{-1}. The v_d measured on the last two days of the study had magnitudes approximately twice that of the earlier measurements. In general the deposition velocities were small, with a range of -0.61 to 0.63 cm s^{-1} (see Figure 3.10). Measurements over similar vegetative canopies (z_o = 0.01–0.12 m) have resulted in a similar range of deposition velocities (Wesely *et al.*, 1985; Nemitz *et al.*, 2002, 2004).

3.4. Discussion

3.4.1. *Deposition Velocities in Near-Neutral Atmospheric Conditions*

Morning and evening measurement periods resulted in large magnitude negative and positive deposition velocities. These periods were typically characterized by near-neutral atmospheric conditions (see Figure 3.11). This sharp increase in the magnitude of eddy correlation deposition velocities near the neutral to unstable transition has been observed over grass (Wesely *et al.*, 1985) and forests (Gallagher *et al.*, 1997). The reason for this behavior is unclear.

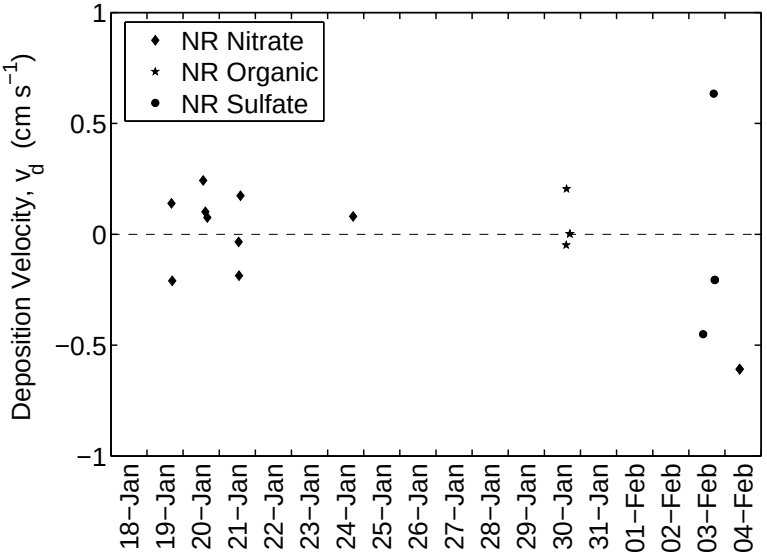

Figure 3.10: Dry deposition velocities for non-refractory (NR) nitrate (m/z = 30), organic (m/z = 43), and sulfate (m/z = 64) aerosol fine particles (0.07 μm < D_{va} < 0.5 μm) measured using eddy correlation mass spectrometry.

Wesely *et al.* (1985) suggested that very windy conditions ($U \approx 4$ m s^{-1}) coincided with these observations. The mean wind speed for the v_d measurements presented here was 0.5 m s^{-1}, with a maximum of 1.6 m s^{-1}. Near-neutral stability typically occurred during morning or evening stability transition periods. Measurements under these conditions may be affected by stagnation of air (Stull, 1988), resulting in unreliable measurement conditions.

3.4.2. *Deposition Velocities in Unstable Atmospheric Conditions*

For highly unstable conditions, L^{-1} < -0.1 m^{-1}, the measured deposition velocities were more erratic. Positive and negative values were observed for nitrate and organic aerosols measured during these periods. Negative deposition velocities have been interpreted as "emission" velocities (Gallagher *et al.*, 1997). Gas-particle interaction within the sampled fetch could result in apparent emission fluxes (Nemitz *et al.*, 2004), although no sources of nitrate or organic materials were present. The signal-to-noise ratio of the Q-AMS eddy correlation program caused non-zero concentration measurements during periods of low aerosol concentrations (see Chapter 2). Thus, it is likely that noise in the signal was correlated with the vertical wind

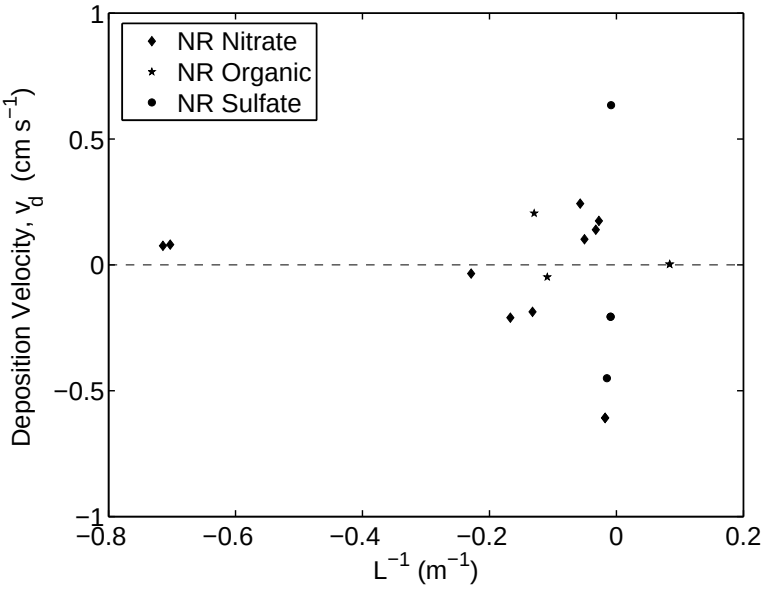

Figure 3.11: Deposition velocities measured during unstable and near-neutral atmospheric conditions.

velocity during some periods, resulting in spurious correlations, $\overline{w'S'}$.

Measurements in moderately unstable conditions, L^{-1} > -0.1 m, resulted in a mean value of v_d = 0.05 cm s^{-1}. Wesely *et al.* (1985) measured mean daily sulfate v_d over grass with z_o = 0.04 m in the range 0.05–0.21 cm s^{-1} for bulk aerosols with no size discrimination, similar to the measurements here. Size-segregated measurements have resulted in $v_d \approx$ 0.07 cm s^{-1} for D_p = 0.1–0.2 μm over heathland with z_o = 0.01 m (Nemitz *et al.*, 2004). Using corrections for hygroscopic particle growth, Vong *et al.* (2004) measured v_d over grass in the ranges 0.5–0.7 cm s^{-1} for $D_p \approx$ 0.34 μm, 0.4–0.5 cm s^{-1} for $D_p \approx$ 0.54 μm, and 0.7–0.9 cm s^{-1} for $D_p \approx$ 0.84 μm.

3.4.3. *Normalized Deposition Velocities*

Particle deposition velocity has been observed to be highly correlated with friction velocity, u_* (Wesely *et al.*, 1985; Gallagher *et al.*, 1997, 2002). Measured deposition velocities increase from near zero for $u_* \approx$ 0.05 m s^{-1} to v_d = 0.6 cm s^{-1} for u_* = 0.3 m s^{-1} (see Figure 3.12). This trend is still apparent if the near-neutral results are excluded (circled points in Figure 3.12). A linear regression of the deposition velocity as a function of friction velocity,

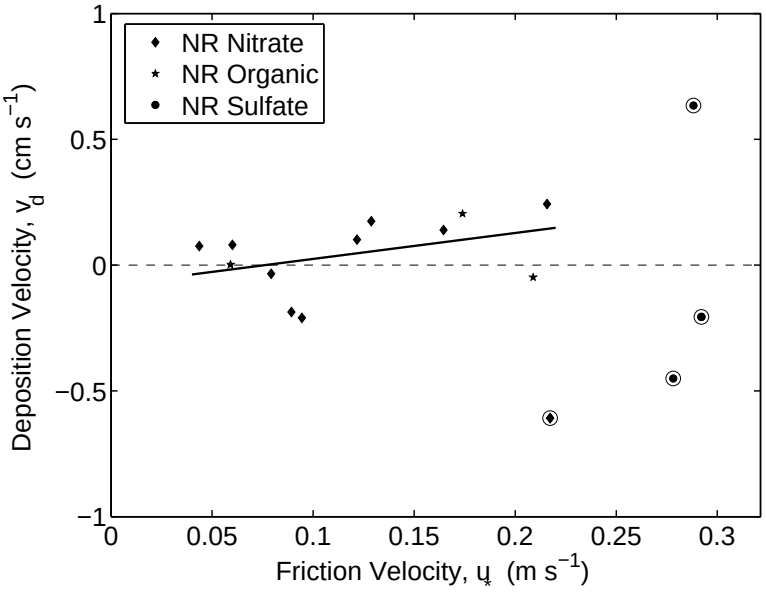

Figure 3.12: Deposition velocities measured as a function of friction velocity. The line is a linear regression of the data, excluding near-neutral conditions (circled points).

excluding near-neutral measurements, yielded a simple parameterization of the results. Prediction errors from this regression are large (± 0.3 cm s^{-1}), likely due to the size-integrated aerosol measurements. This parameterization demonstrates the expected increase in deposition velocity with friction velocity as turbulent mixing and impaction become more important (Gallagher *et al.*, 1997).

Deposition velocities normalized by the friction velocity, v_d/u_*, were calculated for each measurement period. Positive values can be parameterized as a function of stability for unstable atmospheric conditions, $L^{-1} < 0$, using

$$\frac{v_d}{u_*} = a_1 \left(1 + \left(\frac{-a_2}{L}\right)^{2/3}\right) \tag{3.5}$$

where a_1 and a_2 are constants (Wesely *et al.*, 1985). This equation has been suggested to account for increased mixing in unstable conditions. Wesely *et al.* (1985) found a range of a_1 = 0.0015–0.0025 and a_2 = 300 provided a good fit for measurements over grass and Nemitz *et al.* (2004) found a value of a_1 = 0.001 for moorland vegetation. Under unstable conditions, L^{-1} < -0.02 m^{-1}, v_d/u_* were near the parameterization of Wesely *et al.* (1985)

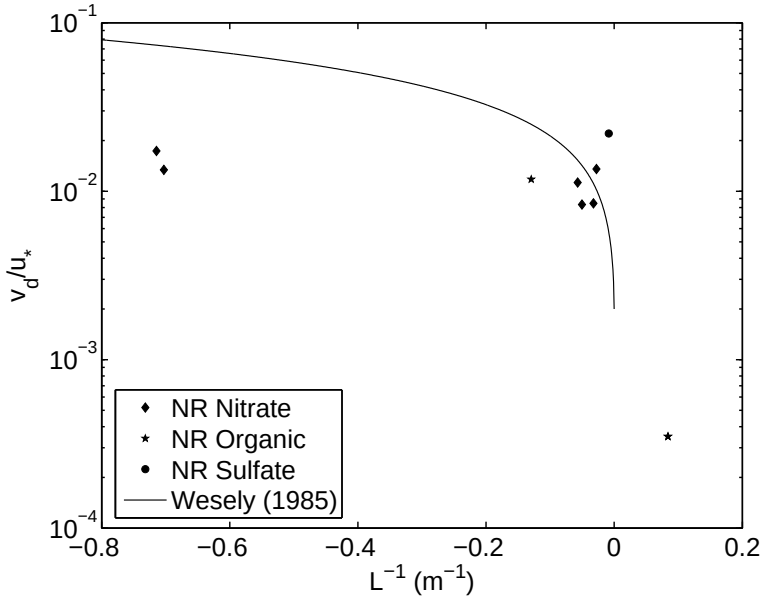

Figure 3.13: Deposition velocities measured as a function of atmospheric stability, L^{-1}. The line is the regression of (Wesely *et al.*, 1985) for unstable conditions.

for similar surface roughness (see Figure 3.13). Near-neutral conditions deviated from the parameterization line, similar to the results of Wesely *et al.* (1985) and Gallagher *et al.* (1997). For highly unstable conditions, L^{-1} < -0.1 m^{-1}, measurements have been made in the range $v_d/u_* = 0.0324 \pm 0.0082$ (Wesely *et al.*, 1985). Two values of nitrate v_d were measured in highly unstable conditions with a mean of $v_d/u_* = 0.015$.

No significant difference was found between aerosol deposition velocities during measurements of nitrate, organic, and sulfate aerosol species. Large sulfate deposition velocities measured during near-neutral conditions cannot necessarily be interpreted as increased sulfate aerosol deposition relative to nitrate and organic aerosols due to the uncertainty of measurements near the stability transition.

3.5. Conclusions

A new eddy correlation mass spectrometry (ECMS) method was developed to measure speciated fine particle deposition velocities. An eddy correlation program for the Aerodyne Quadrupole Aerosol Mass Spectrometer was used to measure v_d over an agricultural field. Deposition velocities for non-refractory nitrate, organic, and sulfate aerosol components

were small in the range -0.6 to 0.6 cm s^{-1} for 16 measurement periods. A mean value of v_d = 0.05 cm s^{-1} was measured during moderately unstable atmospheric conditions, which provide the most reliable estimates of v_d. These results are for the integrated aerosol sampled, thus some variability is due to changes in the particle size distribution. The estimated v_d values are in agreement with the range of particle deposition velocities measured over similar aerodynamic roughness canopies (Wesely *et al.*, 1985; Nemitz *et al.*, 2002, 2004).

The EC mode data acquisition program erroneously truncated the nominal time-of-flight scale, which excluded PToF times less than 1 ms (see Chapter 2). The EC mode demonstrated a linear response to mass loading of NH_4NO_3 calibration particles with a factor of seven decrease in sensitivity compared to the ambient sampling program. This suggests that correction of the EC mode program could significantly improve the accuracy of v_d measured using the ECMS method.

3.6. Nomenclature

Variables

a_1	parameterization of normalized deposition velocities under stable conditions
a_2	parameterization of normalized deposition velocities under unstable conditions
c	concentration
Co	cospectrum
D_p	particle diameter
D_{tube}	tube diameter
D_{va}	particle vacuum aerodynamic diameter
f	frequency
F	flux
F_M	momentum flux
k	von Karman constant (0.4)
L	Obukhov length
m/z	mass-to-charge ratio
Q_E	latent heat flux
Q_H	sensible heat flux
r	dimensionless radius
R	sampling line inner radius
Re	Reynolds number, $2\,\rho\,U\,R/\mu$
S	Q-AMS signal
t	time
T	temperature
u	longitudinal wind velocity
u_*	friction velocity
U	mean wind speed
v	lateral wind velocity

v_{air} average sampling velocity

v_d deposition velocity

$\dot{V}$ volumetric flow rate

w vertical wind velocity

x isokinetic probe inner radius

z height above ground level

z_o aerodynamic roughness length

Greek Symbols

β Bowen ratio

ν_{air} kinematic viscosity of air

ρ density of air

Operators

$\overline{(\,)}$ mean

$(\,)'$ deviation from mean

4. ATMOSPHERIC DRY DEPOSITION OF GASEOUS AND PARTICULATE NITROGEN TO URBAN-INFLUENCED SONORAN DESERT SITES

4.1. Introduction

Atmospheric deposition is an important vector for the transfer of anthropogenic nutrients to terrestrial ecosystems (Lovett, 1994). In arid regions, such as the western United States, dry deposition is the dominant mechanism for pollutant deposition (Fenn *et al.*, 2003). Urbanization in this region magnifies the impact of atmosphere-land exchange by increasing the emissions of nitrogen pollutants (Lovett *et al.*, 2000; Fenn *et al.*, 2003). This additional atmospheric N is eventually deposited to the biosphere where it may affect receptor ecosystems. Deposition monitoring programs measure wet and dry deposition on national or regional scales, focusing on non-urban areas to avoid local influences (Lovett *et al.*, 2000). Urban air quality monitoring is generally focused on health-related pollutants, such as ozone and particulate mass, rather than nutrient species. Thus, measurements of deposition in highly impacted urban areas are relatively sparse (Gregg *et al.*, 2003).

The Phoenix, Arizona, metropolitan area is an example of an arid region with significant atmospheric pollution that is expected to result in increased deposition in and around the city. Modeled estimates of nitrogen dry deposition are about 7.5, 13.5, and 15.0 kg N ha^{-1} y^{-1} for the upwind desert, urban core, and downwind desert, respectively (Fenn *et al.*, 2003). The average deposition was 12 kg N ha^{-1} y^{-1} for the entire modeled area with a maximum of 28.0–29.0 kg N ha^{-1} y^{-1}. For comparison, total nitrogen wet deposition averaged over the Phoenix area was estimated to be 2.4 kg N ha^{-1} y^{-1} (Baker *et al.*, 2001). Most of the nitrogen deposition in the model was from oxidized forms of nitrogen which are byproducts of combustion emissions. Deposition of reduced nitrogen was estimated to be 3.5 kg N ha^{-1} y^{-1} (Baker *et al.*, 2001; Fenn *et al.*, 2003).

Measurements of dry deposition fluxes have been made using bulk deposition collectors, a simple and inexpensive collection technique (Lovett, 1994). However, bulk collection is inadequate to measure true deposition fluxes to natural surfaces due to inclusion of extraneous materials and evaporative losses of collected gases and volatile aerosol components

(Wesely and Hicks, 2000), especially in arid regions where dry deposition may be significant. For example, estimates of nitrogen dry deposition in the Phoenix area using bulk collection measurements are 2.3–7.0 kg N ha^{-1} y^{-1} (Lohse, 2007). These flux estimates are considerably lower than model estimates and can be considered a minimum estimate of dry deposition. Bulk collectors tend to overestimate the fraction of the flux due to wet deposition (Lovett, 1994). Bulk collectors with automated precipitation sensors have been used to estimate wet deposition nitrogen fluxes of 1–3 kg N ha^{-1} y^{-1} in the Phoenix area (Lohse, 2007).

Another technique to measure deposition is to infer fluxes from measurements of atmospheric concentrations and estimates of the atmosphere-surface exchange rate (Hicks *et al.*, 1991; Meyers *et al.*, 1991; Lovett, 1994; Wesely and Hicks, 2000). The dry deposition flux, F, is calculated as

$$F = -v_d c \tag{4.1}$$

where v_d is the deposition velocity and c is the concentration. By convention the deposition velocity is positive for a downward flux ($F < 0$). The deposition velocity represents the cumulative effect of the physical processes responsible for dry deposition including turbulent transport, Brownian diffusion, and surface interaction (Slinn, 1982).

The inferential method has been used to estimate dry deposition using measurements of gas and particle concentrations collected on filters (Hicks *et al.*, 1991; Meyers *et al.*, 1991; Ollinger *et al.*, 1993; Clarke *et al.*, 1997; Meyers *et al.*, 1998; Baumgardner *et al.*, 2002). Fluxes were then calculated using deposition velocities developed from parameterizations for different land use types and seasonal conditions (Hicks *et al.*, 1987; Wesely *et al.*, 1989; Walmsley and Wesely, 1996; Meyers *et al.*, 1998; Zhang *et al.*, 2001, 2003). Hicks *et al.* (1987) suggest direct measurements of atmospheric boundary layer variables using micrometeorological methods to obtain more precise estimates of the atmospheric components of deposition velocities. However, most long-term deposition studies use measurements of meteorological variables, including temperature, solar radiation, wind speed, and standard deviation of the wind direction (Ollinger *et al.*, 1993; Clarke *et al.*, 1997; Baumgardner *et al.*, 2002). Model development

studies have used micrometeorological measurements of eddy fluxes for evaluation purposes (Meyers *et al.*, 1998).

Dry deposition fluxes of gaseous and particulate nitrogen in the Phoenix area were measured here using the inferential method. The goal of this work was to apply the inferential method to measure nitrogen dry deposition fluxes and examine patterns of nitrogen deposition at urban-influenced Sonoran desert sites. Gas and particle concentrations were measured using a denuder and filter sampler system at three Sonoran desert sites located upwind, within, and downwind of the Phoenix urban core. Meteorological data were collected using meteorological towers at the same locations. Micrometeorological measurements were made at one Sonoran desert site to estimate atmospheric boundary layer characteristics for all three sampling sites. The boundary layer data were then parameterized using meteorological data for use with measurements from each site. Modeled deposition velocities were then used to calculate dry deposition fluxes.

4.2. Methods

4.2.1. *Measurement Sites*

Three sites were chosen along the prevalent wind direction (west to east) in the Central Arizona-Phoenix area, which includes the Phoenix metropolitan area and the surrounding agricultural and Sonoran desert area (see Figure 4.1). The upwind site was at the White Tank Mountain Regional Park (WTM), approximately 30 km west of Glendale, Arizona, surrounded by mountainous desert terrain to the west and bordered by desert, agricultural, and residential land to the east. The core site was at the Desert Botanical Garden (DBG), approximately 10 km east of downtown Phoenix, within the city of Phoenix and surrounded by urban industrial, residential, and recreational land. The downwind site was at the Lost Dutchman State Park (LDP), approximately 25 km east of Mesa, Arizona, at the base of the Superstition Mountains to the north and east, and bordered by desert and low density residential land to the south and west.

The local terrain at all three measurement sites was flat or gently sloped Sonoran desert (see Figures 4.2, 4.3, and 4.4). The vegetation canopy was similar at all three sites, consisting

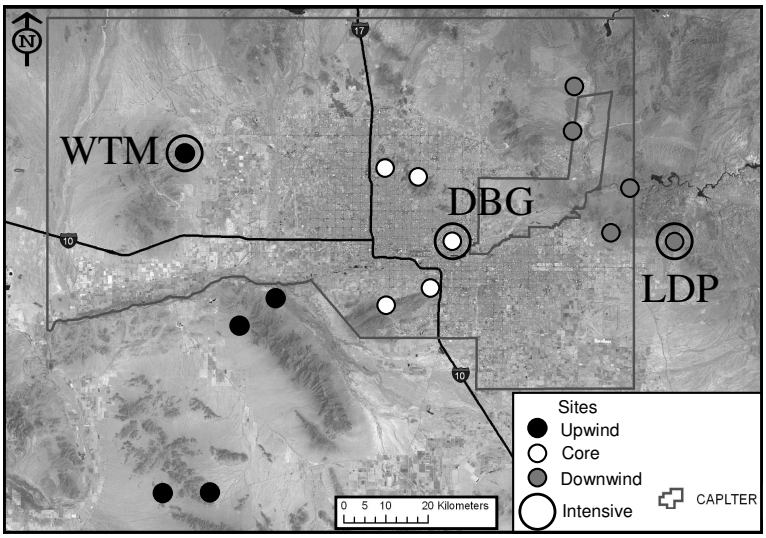

Figure 4.1: Map of the measurement study area. Intensive measurement sites for inferential flux measurements are circled.

of patchy coverage of desert shrubs and trees. The major vegetation species were bursage (*Ambrosia deltoidea*) and creosote bush (*Larrea tridentata*) and minor species were palo verde (*Cercidium microphyllum*) and saguaro cactus (*Carnegiea gigantea*).

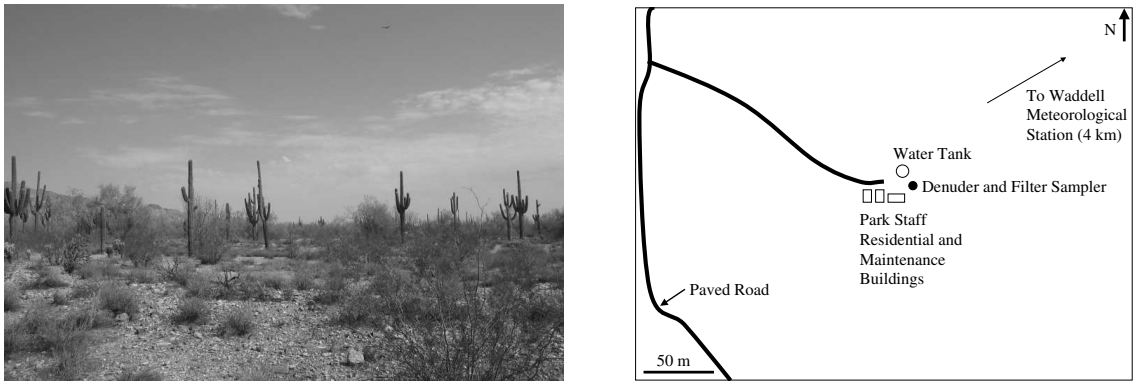

Figure 4.2: Photo, facing north, and schematic from an aerial photo of the White Tank Mountain (WTM) site.

4.2.2. *Atmospheric Concentration Measurement*

Atmospheric samples were collected for 24 hours following the U.S. Environmental Protection Agency (EPA) six-day monitoring schedule during two measurement periods: January and May 2007. Samples were collected using a denuder and filter sampler (DFS) consisting

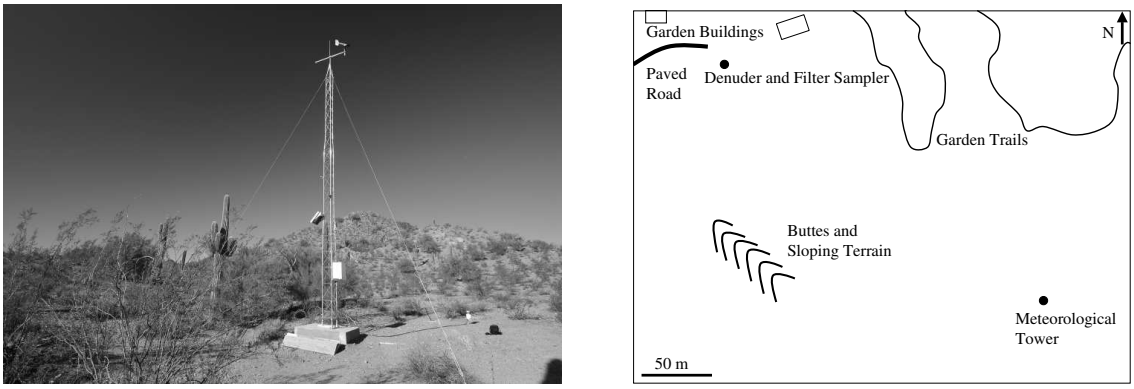

Figure 4.3: Photo, facing west, and schematic from an aerial photo of the Desert Botanical Garden (DBG) site.

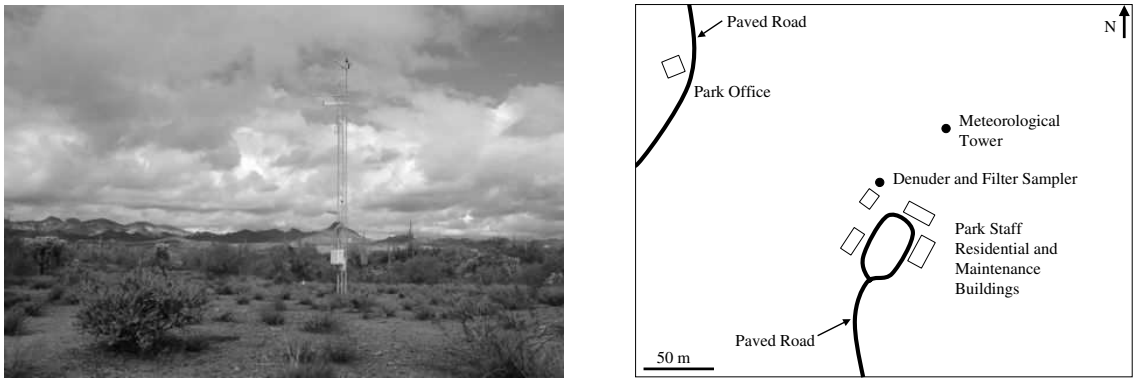

Figure 4.4: Photo, facing north, and schematic from an aerial photo of the Lost Dutchman State Park (LDP) site.

of two sampling trains, each with a size-selective cyclone inlet, two annular denuders and a three-stage filter pack. The cyclone inlets had a 50% cutpoint diameters of 2.5 μm and 10 μm, to facilitate calculation of fine (D_p < 2.5 μm) and coarse (D_p 2.5–10 μm) particulate nitrogen concentrations. Air then flowed through the annular denuders in series: the first was coated with citric acid to collect ammonia gas (NH_3) and the second was coated with sodium carbonate (Na_2CO_3) to collect nitric acid vapor (HNO_3) (Possanzini *et al.*, 1983; Allegrini *et al.*, 1987). Air then flowed into the filter pack, which contained three filters: Teflon filter for particulate nitrate (NO_3^-) and ammonium (NH_4^+), nylon filter for volatilized particulate HNO_3, and citric-acid-impregnated Teflon filter for volatilized particulate NH_3 (Allegrini *et al.*, 1987). Collection of gas phase HNO_3 and NH_3 using denuders and afterfilters was designed to reduce bias due to volatilization of particulate NH_4NO_3 from Teflon filters (Hering and Cass, 1999). Particulate NH_4NO_3 volatilization increases with increasing temperature (Russell *et al.*, 1983). Starting in May 2007, quartz fiber filters (pre-baked at 600 °C for 12 hours) were used in place of Teflon filters so that aerosol carbon could also be measured.

The designed flow through the DFS assemblies was 16.7 l min^{-1}, controlled using a vacuum pump and a critical orifice. The flow rate for each DFS sampling train was measured before and after the start of the sampling period using a calibrated rotameter to be within 10% of the design flow rate. The flow rate for each sample was taken to be the average of the flows measured before and after each sampling period. The DFS was mounted in a weather-proof wooden box with access holes for the size-selective cyclones and two cooling fans. An automatic timer was used to control sample duration and an hour counter was used to measure the actual sample duration to within 0.1 h.

Annular denuder and filter samples were extracted within 48 hours of collection. Each annular denuder was extracted with two sequential washings with 5 ml of nanopure water. Filters were extracted by sonication in 10 ml of nanopure water. Sample extracts were then analyzed for NO_3^- and HNO_3 (as nitrate) using automated colorimetry on a flow injection analyzer (QC 8000, Lachat Instruments, Loveland, CO) and for NH_4^+ and NH_3 (as ammonium) using the

indophenol method on an autoanalyzer (TrAAcs 800, Bran-Luebbe, Inc., Delavan, WI) (Allegrini *et al.*, 1987; Chow, 1995). Quartz fiber filters were first cut in half: one half was extracted as above and the other half was analyzed for total carbon using flash combustion elemental analysis (PE 2400, Perkin-Elmer, Inc., Waltham, MA). The extracts from the citric-acid-coated annular denuder and citric-acid-impregnated filter were neutralized to pH $\approx$ 7 using concentrated NaOH. All samples were stored at $\approx$ 4 °C between collection and analysis.

Method blanks were prepared for each sampling date during the study. Method blanks were collected by coating clean denuders with the same solution used for that sample date and loading new filters in a filter pack. The denuders and filters were then extracted using the same procedure as normal samples. Method blank extracts were handled, stored, and analyzed in the same manner as normal samples.

Atmospheric concentrations of HNO_3, NH_3, and particulate NH_4NO_3 were calculated from the filter and denuder extract concentrations. The mean of the concentrations measured for the fine and coarse size samples from the sodium-carbonate-coated and citric-acid-coated denuders were used to estimate the concentrations of HNO_3 and NH_3, respectively. Concentrations of particulate NH_4^+ were calculated as the sum of the concentrations from Teflon (or quartz fiber) and citric-acid-impregnated filters. Concentrations of particulate NO_3^- were calculated as the sum of the concentrations from Teflon (or quartz fiber) and nylon filters. Method blanks were subtracted from all samples. Sample concentrations less than the atmospheric detection limit were reported as 0 μg N m^{-3}.

4.2.3. *Meteorological Data*

Meteorological variables were also measured at each site for dry deposition calculations. Meteorological measurements for WTM were obtained from the Waddell, Arizona, meteorological station approximately 4 km northeast of the WTM site. These data were retrieved from the Arizona Meteorological Network website (`http://ag.arizona.edu/azmet/`). Wind speed, U, and direction, θ, at 10 m, air temperature, T, relative humidity, RH, and solar radiation, Q_*, at DBG and LDP were measured continuously and recorded as ten-minute averages

(see Figures 4.3 and 4.4). Total precipitation was recorded for each ten-minute period. The Waddell meteorological station was located in an agricultural area, with several buildings approximately 50 m to the south and a residential area approximately 250 m to the east. At the DBG site, several buttes were located approximately 200 m to the west of the measurement tower. At the LDP site, four residential and maintenance buildings used by the park staff were located approximately 50 m to the south-southwest and downslope of the measurement tower. No precipitation was measured at any site on the dates when filter and denuder samples were collected.

4.2.4. *Micrometeorological Measurement Instrumentation*

Eddy correlation measurements were made at the LDP site from 28 February to 31 May 2007 in order to characterize surface exchange for the Sonoran desert landscapes. This site was chosen because the surrounding terrain was relatively homogeneous and air flow to the measurement tower was unobstructed, excluding the sector from the park buildings (see Figure 4.4). The LDP site was assumed to represent typical atmospheric boundary layer characteristics at all three measurement sites since the vegetation and terrain were similar.

A 3-D sonic anemometer (SATI-3K, Applied Technologies, Inc., Longmont, Colorado) was mounted at 8.5 m to measure air flow above the site. The "K" style sonic anemometer was designed to minimize probe-induced flow distortion errors (Kaimal *et al.*, 1990). The sonic anemometer had a path length of 15 cm, and reported 10 Hz mean measurements of the three wind components (u, v, and w) with a resolution of ± 0.03 m s^{-1} and sonic temperature, T, with a resolution of ± 0.1°C. The anemometer was calibrated immediately before use and was mounted on a 2 m boom, oriented toward the south-west, the direction of the prevalent wind (see Figure 4.5).

An open path infrared gas analyzer (IRGA) (LI-7500, Li-Cor, Inc., Lincoln, Nebraska) was used to measure gas phase CO_2 and H_2O concentrations. The IRGA had a 12.5 cm path length and updated the analog output at 300 Hz with a 16 bit resolution for each channel. The IRGA was calibrated before use, and was mounted approximately 0.2 m behind and at the same

Figure 4.5: Eddy correlation equipment at the Lost Dutchman State Park (LDP) site. The sonic anemometer and infrared hygrometer booms extend to the left from the tower. The propeller anemometer is at the top of the tower.

height as the sonic anemometer (see Figure 4.5). Data from the sonic anemometer and IRGA were recorded at 10 Hz using a data logger with a serial interface (CR1000, Campbell Scientific, Inc., Logan, UT).

4.2.5. *Eddy Correlation Data Analysis*

Calculation of turbulent fluxes requires measurement of signals over 15–30 minutes to fulfill the statistical requirements for time series analysis (Foken and Wichura, 1996). The averaging period for eddy correlation calculations was determined using an ogive function (cumulative integral of the cospectrum) (Oncley *et al.*, 1990; Foken and Wichura, 1996). This function converges to a constant value at a frequency that can be converted to an averaging period for flux measurements. Deviations up to 10% of the total are tolerated due to the variability of turbulent spectra.

Momentum flux ogives, Co_{uw}, were calculated for $\approx$ 2 h subsets of daily data to determine the averaging time (see Figure 4.6). The ogives typically converge to 90% of the total between $f \approx 1 \times 10^{-3}$ and $\approx 6 \times 10^{-4}$ Hz, corresponding to averaging times of 15 and 30 min-

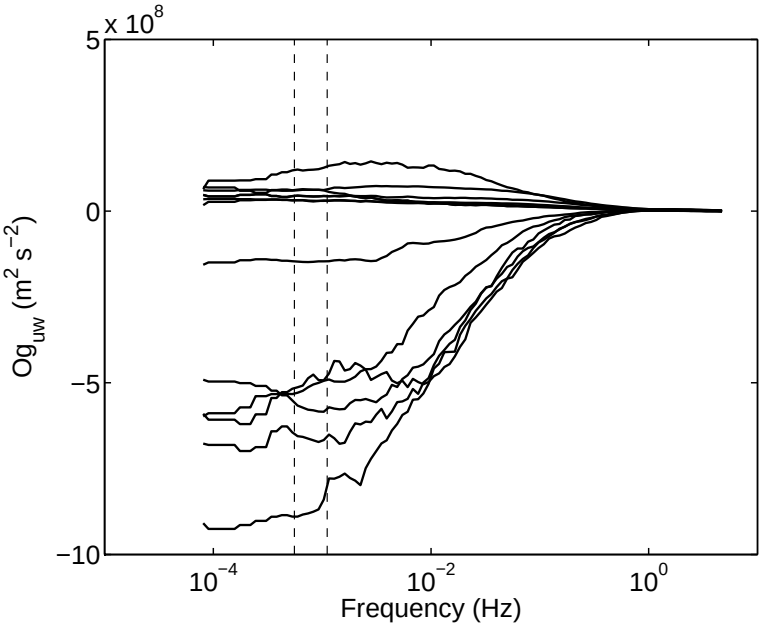

Figure 4.6: Example of the ogive function (cumulative integral of the cospectrum) for momentum flux measured at the Lost Dutchman State Park (LDP) site on 6 May 2007. Each line represents a 2 h period of 10 Hz measurements. The vertical dashed lines at $f \approx 1 \times 10^{-3}$ and $\approx 6 \times 10^{-4}$ Hz correspond to averaging periods of 15 and 30 minutes, respectively.

utes, respectively. For example, the momentum ogives for 6 May 2007, are nearly constant for averaging times longer than approximately 30 minutes. Occasionally, a minimum in the ogive is apparent, indicating that non-steady state conditions reduce the flux measurement for longer averaging times (Foken *et al.*, 2006). The ogives generally converge to within the 10% tolerance of spectra variability for averaging times of 15–30 minutes. Thus, an averaging time of 30 minutes was used here.

The raw data were corrected for orientation and leveling of the sonic anemometer using a coordinate rotation on the three-dimensional wind velocity measurements (McMillen, 1988). The coordinate rotation was done such that $\overline{v} = 0$ and $\overline{w} = 0$, aligning u with the mean horizontal wind vector and perpendicular to the underlying surface for each averaging period. Data were then segregated by wind direction to include only that collected from the dominant daytime wind direction, 150–270° (see Figure 4.7 and 4.4). The resulting homogeneous fetch-

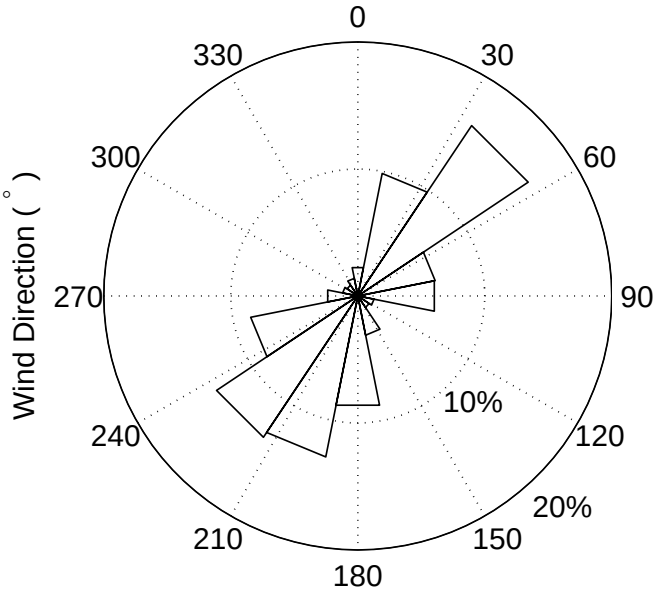

Figure 4.7: Wind rose showing the fraction of 30 minute average wind direction during micrometeorological measurements at the Lost Dutchman State Park (LDP) site. Winds were predominantly from the south-southwest during the day (≈ 0800–1900) and from the northeast overnight.

to-height ratio of > 100 for the retained sampling periods meets the suggested measurement criteria (Businger, 1986; Wesely and Hicks, 2000).

4.3. Results and Discussion

4.3.1. *Atmospheric Nitrogen Concentrations*

Volatilized material collected on the nylon and citric-acid-impregnated backup filters accounted for approximately 0–50% of the total NO_3^- mass and 0–60% of the total NH_4^+ mass, respectively, during this study. This range is in agreement with predictions of NH_4NO_3 gas-particle equilibrium (Russell *et al.*, 1983). For the temperature range -8 to 25 °C (mean ≈ 10 °C) measured during January, the equilibrium shifts toward the particle phase. For the temperature range 10–39 °C (mean ≈ 27 °C) measured during May, the equilibrium shifts toward the gas phase.

Atmospheric nitrogen concentrations were measured at the WTM, DBG, and LDP sites (see Figure 4.8 and Table 4.1). Data were missing for some sampling dates due to power

loss at the collection site or other collection issues. The dominant species at all sites was NH_3, typically accounting for 50% or more of the total N. Gas-phase nitrogen concentrations at the DBG and LDP sites in May were more than double the values in January. Previous measurements of gaseous nitrogen in downtown Phoenix, within the urban core, during winter were in the range ≈ 0–2 μg N m^{-3} with a mean of 0.6 μg N m^{-3} for HNO_3 and ≈ 0–29 μg N m^{-3} with a mean of 7.6 μg N m^{-3} for NH_3 (Watson *et al.*, 1994).

Table 4.1: Mean Monthly Nitrogen Concentrations (μg N m^{-3}) Measured During January and May 2007.

Month	Site	HNO_3	NH_3	NO_3^- (fine)	NH_4^+ (fine)	NO_3^- (coarse)	NH_4^+ (coarse)	Total
January								
	WTM	0.29	0.39	0.12	0.13	0.01	0.00	0.94
	DBG	0.29	0.48	0.09	0.05	0.05	0.01	0.97
	LDP	0.13	0.18	0.08	0.04	0.02	0.00	0.45
May								
	WTM	0.21	0.69	0.03	0.14	0.04	0.03	1.14
	DBG	0.53	1.98	0.12	0.41	0.04	0.03	3.11
	LDP	0.22	0.88	0.07	0.24	0.02	0.01	1.44

Particulate N was relatively low for all measurement periods; fine and coarse particles accounted for nearly equivalent mass of particulate N. Mean monthly fine particulate NO_3^- concentrations at each site were approximatlely equal during the two months. The mean monthly concentration of fine particulate NH_4^+ at the WTM site was approximately equal from January to May. Mean monthly fine particulate NH_4^+ concentrations in May at the DBG and LDP sites were approximately three times those in January. The mean monthly concentrations of coarse particulate NO_3^- and NH_4^+ were not significantly different for all sites in January and May. Similar to measurements of gaseous nitrogen, fine particulate nitrogen concentrations were lower than previous measurements in Phoenix. Fine particulate NO_3^- has been measured in the range 0.02–3.1 μg N m^{-3} with a mean of ≈ 0.2–1.0 μg N m^{-3} (Watson *et al.*, 1994; Tolocka *et al.*, 2001; Brown *et al.*, 2007). Fine particulate NH_4^+ has been measured in the range 0.1–5.0 μg N m^{-3} with a mean of ≈ 0.9–1.2 μg N m^{-3} (Watson *et al.*, 1994; Tolocka *et al.*, 2001).

In general, the total N concentrations at the DBG site were higher than at the WTM or

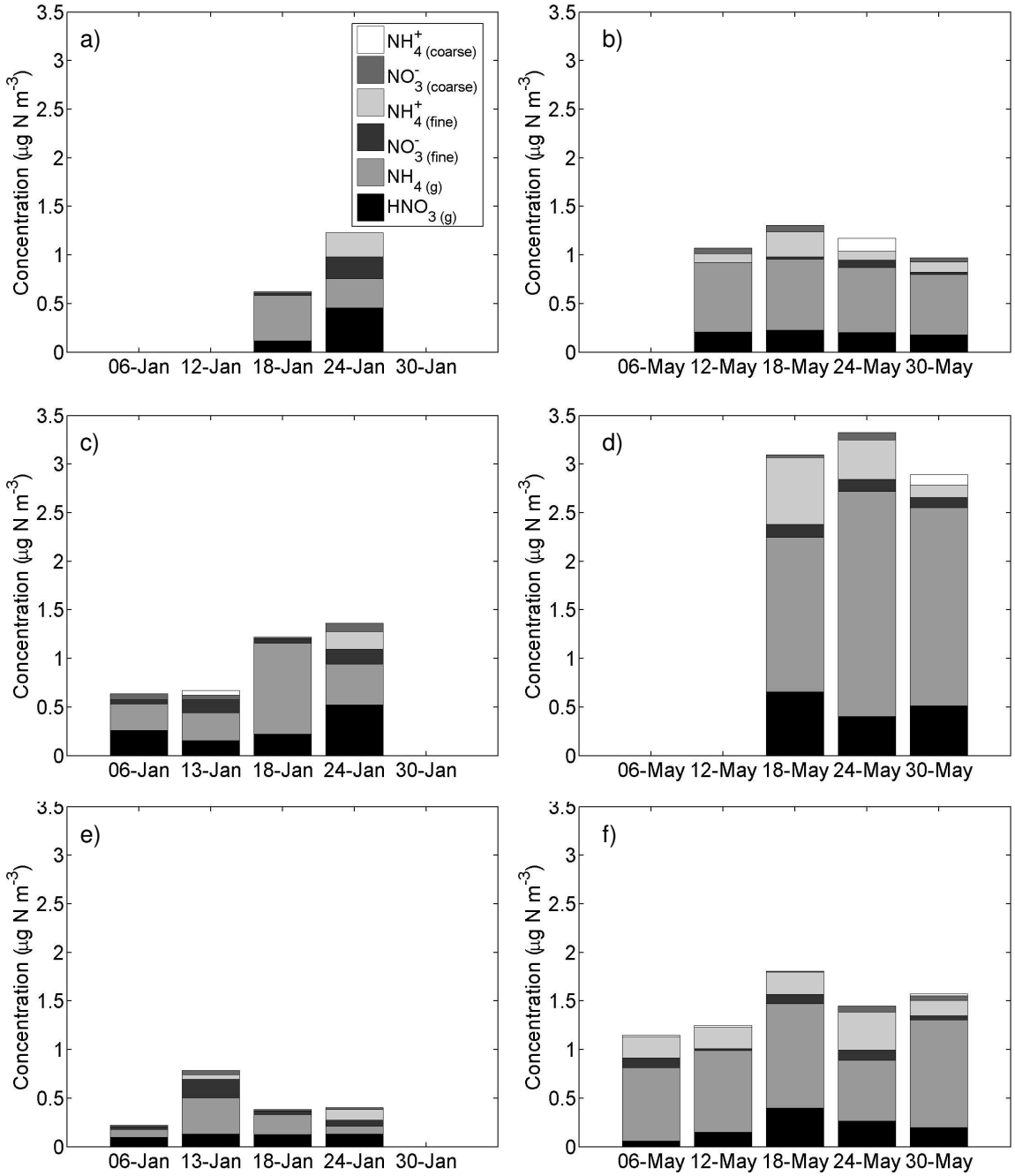

Figure 4.8: Atmospheric concentrations during January (left column) and May (right column) 2007 using denuder and filter samplers: a,b) White Tank Mountain (WTM); c,d) Desert Botanical Garden (DBG); and e,f) Lost Dutchman State Park (DBG) sites.

LDP sites for the same sampling dates. Total concentrations in January were similar at all three sites, with a mean of 0.79 μg N m^{-3}. January concentrations were highest at the DBG site, with a mean of 0.97 μg N m^{-3}. In May, the average total N concentration were 1.14 μg N m^{-3} at the WTM site, 3.11 μg N m^{-3} at the DBG site, and 1.44 μg N m^{-3} at the LDP site.

4.3.2. *Micrometeorological Characterization of a Sonoran Desert Site*

Atmospheric boundary layer parameters necessary for calculation of gas and particle deposition velocities were estimated from micrometeorological measurements at the LDP site. Atmospheric turbulence and turbulent transport of materials is driven by air-surface exchange of energy and momentum. Sensible heat flux, Q_H, was calculated as

$$Q_H = \rho_{\text{air}}\, \hat{c}_{\text{p,air}}\, \overline{w'\theta_v'} \tag{4.2}$$

where ρ_{air} is the density of air, $\hat{c}_{\text{p,air}}$ is the specific heat of air, and θ_v is the virtual potential temperature, which is approximately equal to the sonic temperature (Stull, 1988; Kaimal and Gaynor, 1991). Latent heat flux, Q_E, was calculated as

$$Q_E = L_v\, \overline{w'q'} \tag{4.3}$$

where L_v is the latent heat of vaporization of water and q is the specific humidity measured using the IRGA.

Measurements of Q_H on a typical day during the eddy correlation experiment showed the expected diurnal cycle with heat lost to the surface at night ($\approx$ 2100–0600) and heat release to the atmosphere during the day (see Figure 4.9). The maximum Q_H during the experiment was in the range 250–500 J m^{-2} s^{-1}. During most of the study, very little atmospheric water vapor was available ($q \approx 2.5$ g$_{\text{water}}$ kg$_{\text{air}}^{-1}$) since the site was not irrigated and rain was infrequent. The Q_E was correspondingly low with maximum values in the range 20–30 J m^{-2} s^{-1}. After rain events Q_E increased to $\approx$ 100–200 J m^{-2} s^{-1} for several days (see Figure 4.10).

Friction velocity, u_*, values were calculated using the micrometeorological measurements as

$$u_* = \left[\overline{u'w'}^2 + \overline{v'w'}^2\right]^{1/4} \tag{4.4}$$

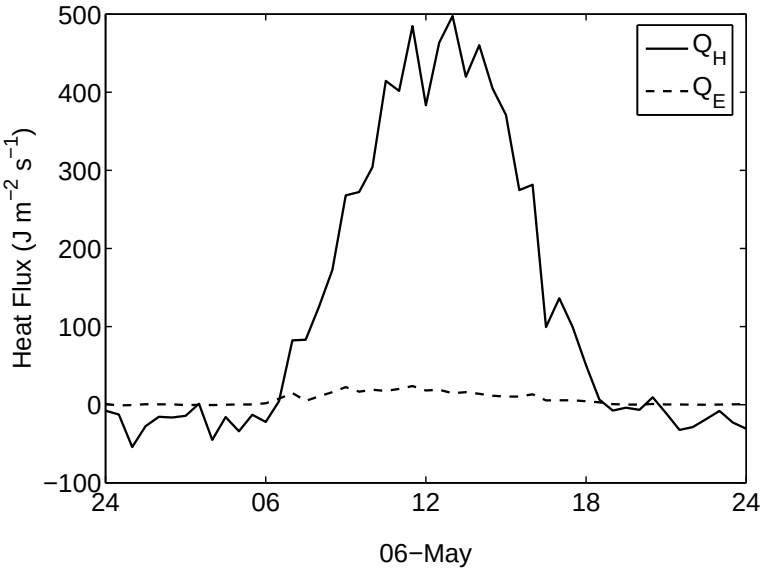

Figure 4.9: Sensible, Q_H, and latent, Q_E, heat fluxes at the Lost Dutchman State Park (LDP) site. Sensible heat is lost to the surface at night ($\approx$ 2100–0600) and released to the atmosphere during the day, with a maximum of ≈ 500 J m^{-2} s^{-1} around noon. Latent heat is generally low, with a maximum of ≈ 20 J m^{-2} s^{-1} around noon.

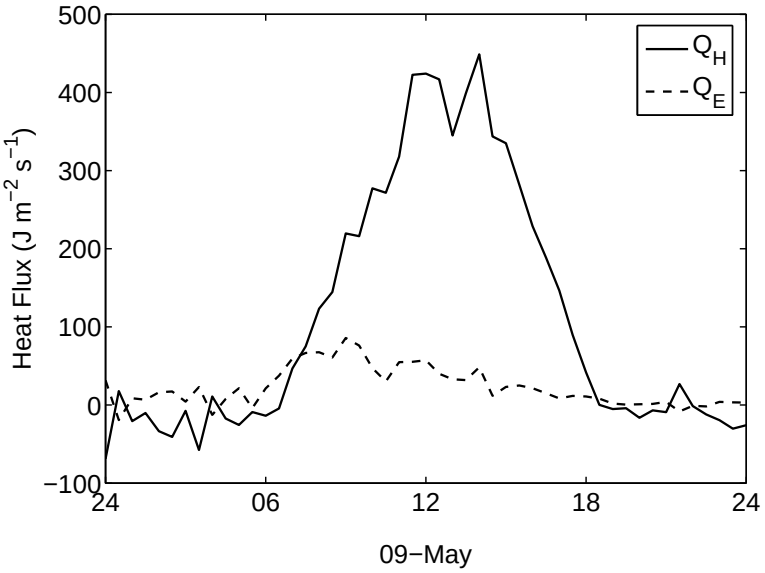

Figure 4.10: Sensible, Q_H, and latent, Q_E, heat fluxes on 9 May 2007 at the Lost Dutchman State Park (LDP) site. Approximately 1.5 mm of rain was measured at the LDP site on 8 May 2007. The maximum latent heat flux was 85 J m^{-2} s^{-1}.

where u, v, and w are the streamline coordinate wind velocity vectors. The friction velocity, which varies with the magnitude of the wind velocity and the surface roughness, is a scaling parameter that represents the magnitude of the wind stress on the surface. The Obukhov length, L, was calculated as

$$L = \frac{-\overline{\theta_v} u_*^3}{kg\left(\overline{w'\theta_v'}\right)} \tag{4.5}$$

where $k = 0.4$ is the von Karman constant, g is the gravitational constant, and $\overline{w'\theta_v'}$ is the kinematic sensible heat flux (Stull, 1988; Kaimal and Finnigan, 1994). The Obukhov length, L, is a surface layer scaling parameter that provides a measure of the stability.

Under near-neutral stability ($|L| > 1000$ m), wind speed is ≈ 0 at a height known as the aerodynamic roughness length, z_o. The wind speed increases logarithmically above z_o as

$$\frac{U}{u_*} = \frac{1}{k} \ln\left(\frac{z-d}{z_o}\right) \tag{4.6}$$

where z is the height above the surface and d is the displacement height. The displacement height is approximately 80% of the height of the vegetative canopy, h (Stull, 1988; Kaimal and Finnigan, 1994). For the Sonoran desert sites $h \approx 1$ m was assumed to reflect the air-surface interaction with the dominant vegetative species. A value of h that included the sparse, taller vegetation would likely increase turbulence and air-surface exchange. Thus, exchange rates using $h = 1$ m represent a low-range estimate for the Sonoran desert sites. Equation 4.6, known as the log-wind profile, was used to predict z_o at the LDP site using measurements of U and u_* under near-neutral stability (Kaimal and Finnigan, 1994). Measurements of $U < 2$ m s^{-1} were excluded in this procedure since slow or stagnant air may not generate sufficient surface stress to obey the log-wind profile (Kaimal and Finnigan, 1994; Schmid *et al.*, 2000). The mean value was $z_o = 0.27 \pm 0.08$ m for the terrain surrounding the measurement tower. This estimate is in agreement with suggestions that $z_o \approx 0.3h$ (Kaimal and Finnigan, 1994). Wind flow from 190–200 °, which includes the park staff buildings (see Figure 4.4), resulted in $z_o \approx 0.6$ m and periods when the wind direction indicated flow from this sector (approximately 5% of the 30 minute periods) were excluded from further analysis.

Under near-neutral stability, the logarithmic wind profile predicts that the friction ve-

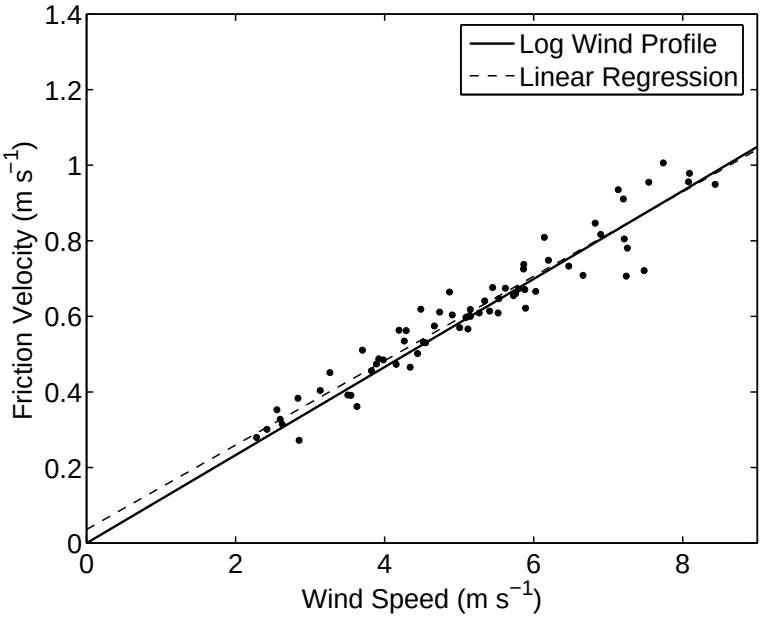

Figure 4.11: Friction velocity and wind speed measurements under near-neutral conditions from February 2007 to May 2007 at the Lost Dutchman State Park (LDP) site.

locity increases linearly with wind speed with a slope $\approx k \ln(z/z_o)^{-1}$. Using the value $z_o = 0.27$ for the LDP site, the log wind profile gives

$$u_* = 0.12U \tag{4.7}$$

where U is the mean wind speed. A linear regression of the friction velocity and wind speed measurements yielded $u_* = 0.11U + 0.04$, in good agreement with the log-wind relationship (see Figure 4.11).

Equation 4.7 was used to estimate the friction velocity from wind speed measurements made at all three sites. Friction velocities predicted using Equation 4.7 were in good agreement with direct measurements of u_* during the micrometeorological measurement period at the LDP site. This parameterization is limited to sectors of the local meteorological observations at each site where measurements are not affected by upwind obstructions. The presence of upwind obstructions likely increased turbulence and air-surface fluxes in these sectors. Thus, Equation 4.7 provided a lower estimate of u_* and the subsequently calculated fluxes.

4.3.3. *Deposition Velocity Model*

Gas deposition velocities were estimated from a process-oriented model (Wesely, 1989; Walmsley and Wesely, 1996). This parameterization does not require plant-specific information but the canopy resistance varies with land use category (LUC), seasonal categorey (SC), and, gas species. Here, LUC 11 (rocky open areas with low-growing shrubs) was selected to best describe the sites used in this work. Values for the adjustable parameters used to calculated the surface resistance for NH_3 are r_j = 300 s m^{-1}, r'_{lu} = 8000 s m^{-1}, r_{ac} = 120 s m^{-1}, r_{gsS} = 400 s m^{-1}, r_{gsO} = 200 s m^{-1}, r_{clS} = 8000 s m^{-1}, and r_{clO} = 800 s m^{-1}. Surface resistance to uptake of HNO_3 is generally small and deposition is controlled by the rate of transport above the canopy (Wesely and Hicks, 2000). This species is treated as a special case and the surface resistance is set to 10 s m^{-1} or the low temperature correction, r_{low}, whichever is larger (Walmsley and Wesely, 1996).

Mean daily deposition velocities were calculated for filter and denuder samples. Gas v_d estimates for HNO_3 were in the range 0.15–3.0 cm s^{-1} with a mean of 1.2 cm s^{-1}. The v_d values for HNO_3 have been predicted to be in the range 1–4 cm s^{-1} (Meyers *et al.*, 1998; Zhang *et al.*, 2003). Gas v_d values for NH_3 were in the range 0.10–0.19 cm s^{-1} with a mean of 0.15 cm s^{-1}. Model predictions of NH_3 v_d have been in the range 0.4–2.0 cm s^{-1} (Meyers *et al.*, 1998). In this case, uptake by the surface is the rate limiting step, so that vegetation type and meteorological conditions are the most important factors in predicting NH_3 v_d (Zhang *et al.*, 2003). The v_d of HNO_3 is predicted to be higher than that of NH_3 since HNO_3 is thought to more readily sorb to surfaces than NH_3.

The parameterizations of Zhang *et al.* (2001) were used to estimate particle dry deposition velocities, selecting LUC 10 (shrubs and interrupted woodlands) to best describe the Sonoran desert sites used in this work. The desert LUC is not appropriate in this case since the sites used in this study have a higher ratio of vegetated to open surface than those used by Zhang *et al.* (2001). Note that the 11 LUC codes of Zhang *et al.* (2001) for particle deposition velocity do not correspond to the 15 codes of Wesely (1989) for gas deposition velocity,

although some of the LUC definitions are comparable. Values of the adjustable parameters to calculate the surface layer resistance to deposition for LUC 10 were $\gamma_s = 0.54$, $\alpha = 1.3$, $\beta = 2$, $A = 10$ mm, and $\varepsilon_0 = 3$. A suggested value for the aerodynamic roughness length of $z_o = 0.1$ m was given for LUC 10, however, the value estimated from micrometeorological measurements at the LDP site, $z_o = 0.27$, was used here. All model parameters were independent of seasonal category for LUC 10 and were used for January and May sampling periods.

Ruijgrok *et al.* (1995) found that estimation of v_d using the mass median diameter of the particle size distribution resulted in underprediction by a factor of 1.5–5 compared to predicted values for the entire size distribution. Thus, v_d for size modes corresponding to fine and coarse particles was calculated using a mass-weighted mean v_d (Ruijgrok *et al.*, 1997). Particle deposition velocities, $v_d(t, D_p)$, were calculated for 308 size bins in the range 0.003–30 μm (see Figure 4.12). Particles were assumed to have the size distribution of a typical urban aerosol (see Figure 4.13) (Whitby and Cantrell, 1976). Deposition velocities, $v_d(D_p)$, were calculated as the cross product of the hourly v_d and the fraction of mass, $x(D_p) = (dV/dlogDp)/(\sum dV/dlogDp)$, in each size bin. Hourly v_d for the fine and coarse size modes were then calculated as the mean value, $v_d = \overline{v_d(D_p)\,x(D_p)}$, for particles in each mode (see Figure 4.14). Mean daily fine and coarse mode particle v_d were calculated from the hourly v_d estimates. Hourly HNO_3 and NH_3 deposition velocities were calculated and mean daily values were calculated from the mean of hourly v_d estimates.

Mean v_d were similar at the three sites. Coarse particle v_d in January were in the range 0.15–2.8 cm s^{-1} with a mean of 0.87 cm s^{-1}. Model predictions of coarse particle v_d are approximately 1.0 cm s^{-1} for similar surfaces (Slinn, 1982; Zhang *et al.*, 2001). Fine particle v_d were in the range 0.01–0.47 cm s^{-1} with a mean of 0.08 cm s^{-1}, in agreement with model predictions of approximately 0.1 cm s^{-1} (Zhang *et al.*, 2001).

4.3.4. *Nitrogen Deposition in the Phoenix Metropolitan Area*

Deposition fluxes at the WTM, DBG, and LDP sites were calculated for the January measurement period (see Figure 4.15 and Table 4.2). Typically, HNO_3 accounted for 50–80% of the

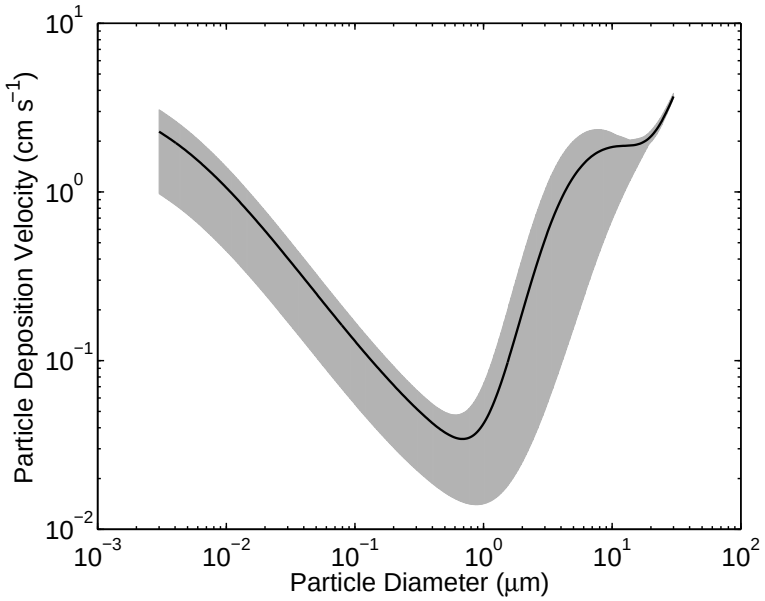

Figure 4.12: Deposition velocities calculated for particles at the Lost Dutchman State Park (LDP) site on 6 May 2007. The gray region represents the range of modeled deposition velocities for 24 hours calculated from parameterizations of hourly meteorological measurements. The line represents the mean of the predicted range.

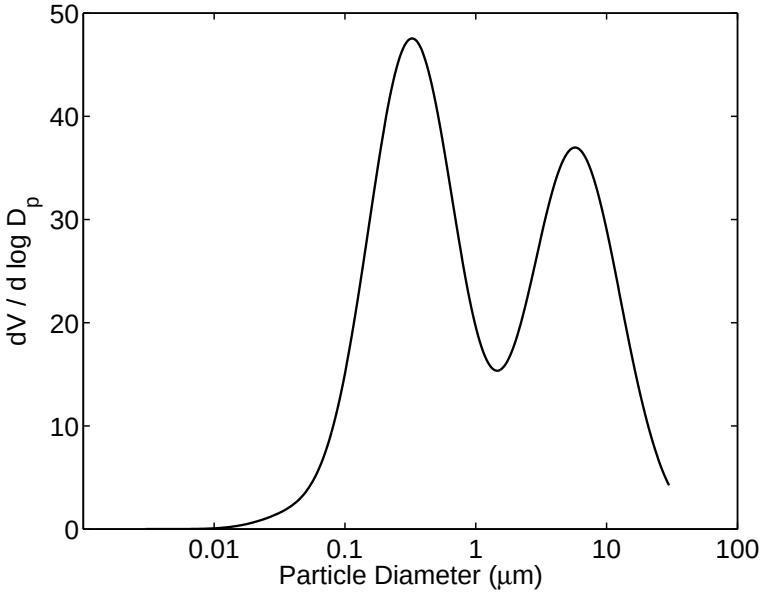

Figure 4.13: Typical urban aerosol volume distribution (Whitby and Cantrell, 1976). This distribution was assumed to describe particles in the atmosphere at the urban-influenced Sonoran desert sites.

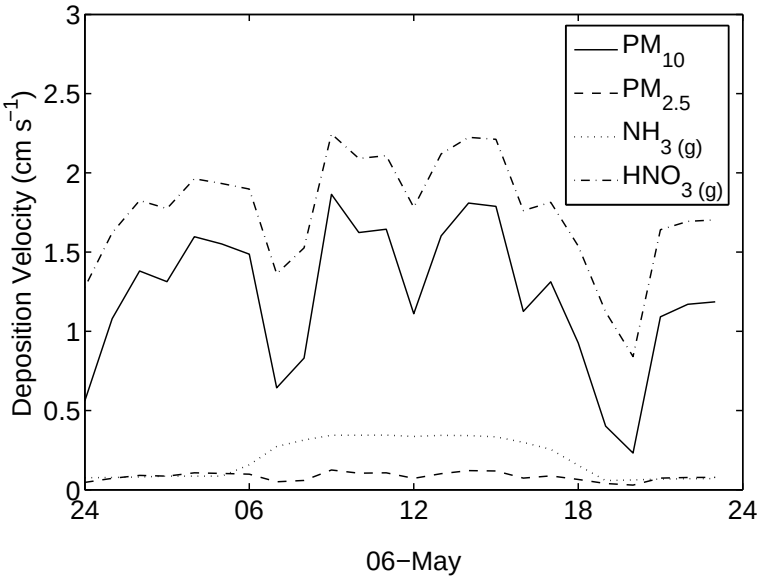

Figure 4.14: Deposition velocities predicted for coarse and fine particles, NH_3, and HNO_3 on 6 May 2007 at the Lost Dutchman State Park (LDP) site.

total nitrogen flux. On average, gaseous nitrogen (HNO_3 + NH_3) accounted for 88% of the total nitrogen flux. Particulate nitrogen deposition in January was low, corresponding to the low concentrations measured. Coarse and fine particulate nitrogen were 9% and 3% of the total nitrogen deposition, respectively.

Table 4.2: Mean Monthly Nitrogen Deposition Fluxes (kg N ha^{-1} y^{-1}) Measured During January and May 2007.

Month	Site	HNO_3	NH_3	NO_3^- (fine)	NH_4^+ (fine)	NO_3^- (coarse)	NH_4^+ (coarse)	Total
January								
	WTM	0.54	0.21	0.01	0.01	0.02	0.00	0.79
	DBG	1.15	0.23	0.02	0.01	0.11	0.05	1.57
	LDP	0.75	0.08	0.03	0.01	0.10	0.00	0.97
May								
	WTM	0.52	0.37	0.00	0.01	0.05	0.04	0.99
	DBG	2.09	0.97	0.02	0.06	0.06	0.06	3.26
	LDP	1.25	0.36	0.03	0.09	0.11	0.04	1.88

During May HNO_3 was the largest source of nitrogen flux, contributing 40–80% of the total (see Figure 4.15 and Table 4.2). Gaseous nitrogen accounted for 89% of the total flux on

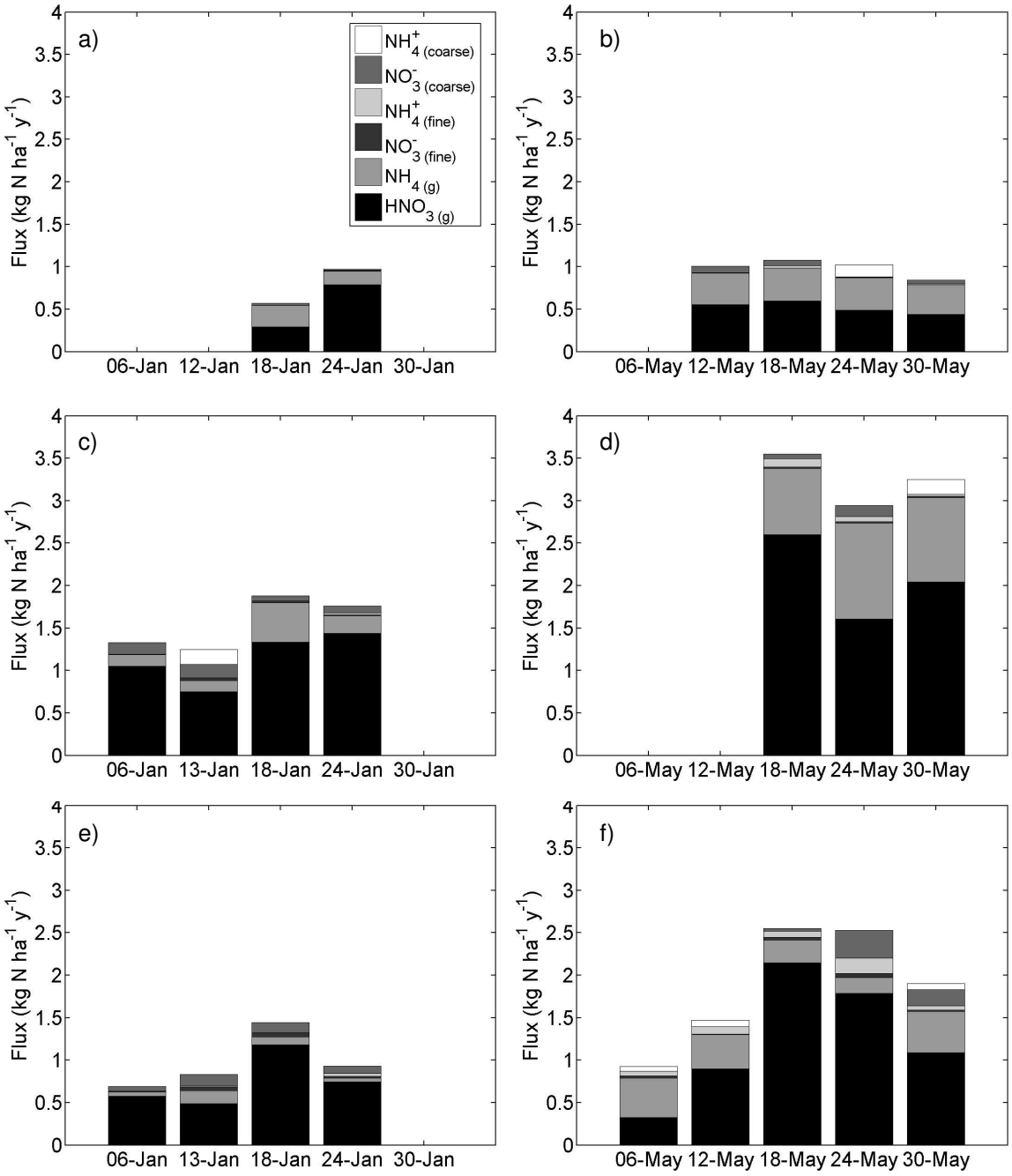

Figure 4.15: Inferred nitrogen fluxes during January (left column) and May (right column) 2007: a,b) White Tank Mountain (WTM), c,d) Desert Botanical Garden (DBG), and e,f) Lost Dutchman State Park (LDP) sites.

average. Coarse and fine particulate nitrogen fluxes were 7% and 4% of the total, respectively, during May. Total nitrogen deposition fluxes during the May measurement period were similar at the WTM site but higher at the DBG and LDP sites. This corresponds to the increase in total nitrogen concentrations from January to May.

The DBG site had the highest nitrogen deposition fluxes during both measurement periods. During January, the total nitrogen flux at DBG was double that at WTM and 1.6 times that at LDP. In May, the total nitrogen flux was more than three times the flux at the WTM site and 1.7 times that at the LDP site. Assuming that the concentrations and deposition fluxes at the WTM site represent background levels, the increased deposition at the DBG site was likely a result of increased nitrogen pollutant concentrations in the urban core. These pollutants were advected away from the urban core, along the dominant wind direction, and resulted in increased concentrations and deposition fluxes at the LDP site.

Annual nitrogen fluxes were calculated from the mean of the monthly mean deposition estimates (see Figure 4.16). Total nitrogen fluxes were 0.92 kg N ha^{-1} y^{-1} at the WTM site, 2.28 kg N ha^{-1} y^{-1} at the DBG site, and 1.47 kg N ha^{-1} y^{-1} at the LDP site. Mean annual nitrogen (HNO_3, NO_3^-, and NH_4^+) deposition has been estimated to be 0.7–1.1 kg N ha^{-1} y^{-1} at a desert site with no urban influence (Baumgardner *et al.*, 2002), similar to the annual deposition at the WTM site. Fenn *et al.* (2003) estimated nitrogen dry deposition of 7.5 kg N ha^{-1} y^{-1} for the upwind desert, 13.5 kg N ha^{-1} y^{-1} for the urban core, and 15 kg N ha^{-1} y^{-1} for the downwind desert. The ratio of deposition at the DBG site to that at the WTM site, 2.5, is similar to the ratio predicted for upwind to core deposition, 1.8, by Fenn *et al.* (2003). Deposition measured at the LDP site was elevated compared to the WTM site but lower than the DBG site. This suggests that nitrogen pollutants were transported from the urban core and deposited in the downwind desert.

4.4. Conclusions

Micrometeorological measurements at the LDP site were used to estimate boundary layer characteristics at a Sonoran desert site. Measurements of wind speed and friction ve-

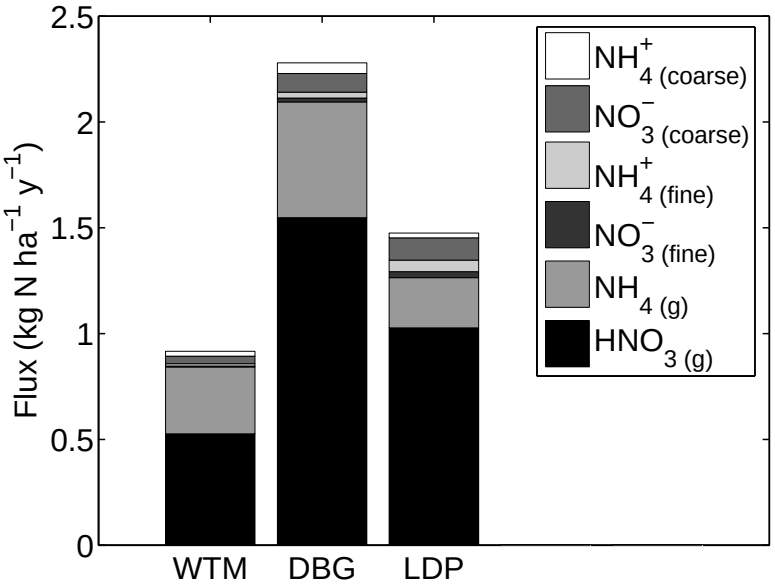

Figure 4.16: Annual nitrogen deposition to Sonoran desert sites in the Phoenix area.

locity were used to estimate the aerodynamic roughness length z_o = 0.27 m. The LDP site was assumed to represent typical atmospheric boundary layer characteristics at all three measurement sites since the vegetation and terrain were similar. Friction velocities were then parameterized using the mean wind speed for calculation from standard meteorological measurements at all three sites. Deposition velocities were calculated from standard meteorological measurements input to particle and gas deposition models. Parameters were chosen based on the model land use categories that best represent the Sonoran desert sites.

Atmospheric dry deposition of nitrogen species was measured using the inferential method at three sites upwind, within, and downwind of the Phoenix urban core. Atmospheric samples of HNO_3, NH_3, particulate NO_3^-, and particulate NH_4^+ were collected using a denuder and filter sampler. Ammonia gas was typically the largest component of atmospheric nitrogen, accounting for more than 50% of the total during the January and May 2007 measurement periods. Mean total nitrogen concentrations in January were 0.93, 0.97, and 0.44 μg N m^{-3} at the WTM, DBG, and LDP sites, respectively. In May, the concentrations were 1.12, 3.11, 1.44 μg N m^{-3} at the WTM, DBG, and LDP sites, respectively.

Atmospheric nitrogen dry deposition fluxes, calculated from measured atmospheric

concentrations and predicted deposition velocities, at the upwind site were similar in January and May. This indicates a relatively constant background of nitrogen deposition upwind of the Phoenix urban core. Nitrogen deposition fluxes were highest at the core site, with total fluxes 1.6–3 times those at the upwind site. Deposition fluxes at the downwind site were 1.5 times those at the upwind site, indicating transport of nitrogen pollutants from the urban core.

The measured fluxes were approximately an order of magnitude lower than previous model estimates (Baker *et al.*, 2001; Fenn *et al.*, 2003). Previous studies have shown that oxides of nitrogen, mainly NO_x and HNO_3, were the primary source of nitrogen deposition. Here, NH_3 was shown to be a significant source that has not been accurately measured or predicted. NO_x was not measured during this study. Model predictions may also overestimate nitrogen deposition since urban air pollution models have historically focused on high pollution events that are especially harmful to human health. The concentrations measured during this study were lower than those expected during high pollution events. The relative magnitude of deposition in the urban core compared to the upwind background is similar to that previously predicted, however, downwind deposition is not as high. This suggests increased dispersion during transport away from the urban core. Increased deposition at remnant desert sites in the Phoenix urban core and downwind desert may cause changes in ecosystem function from increases of nutrient pollutant inputs.

4.5. Nomenclature

Variables

A	characteristic collector radius
c	concentration
$\hat{c}_{\mathrm{p,air}}$	specific heat of air
Co	cospectrum
d	displacement height
D_p	particle diameter
f	frequency
F	flux
g	gravitational constant
h	mean canopy height
k	von Karman constant (0.4)
L	Obukhov length
L_v	latent heat of vaporization of water
Og	ogive function
q	atmospheric water vapor content
Q_E	latent heat flux
Q_H	sensible heat flux
Q_*	incoming solar radiation
r_{ac}	constant for canopy height dependent resistance
r_{clO}	resistance of the lower canopy for ozone
r_{clS}	resistance of the lower canopy for SO_2
r_{gsO}	resistance of the ground surface for ozone
r_{gsS}	resistance of the ground surface for SO_2
r_j	minimum bulk canopy stomatal resistance to water vapor
r_{low}	low temperature correction for canopy resistance

r'_{lu} leaf surface resistance in the upper canopy

RH relative humidity

T temperature

u longitudinal wind velocity

u_* friction velocity

U mean wind speed

v lateral wind velocity

v_d deposition velocity

V particle volume

w vertical wind velocity

x mass fraction

z measurement or reference height

z_o aerodynamic roughness length

Greek Symbols

α empirical constant for impaction efficiency

β empirical exponent for impaction efficiency

γ_s empirical constant for diffusion efficiency

ε_0 particle surface resistance constant

θ wind direction

θ_v virtual potential temperature

ρ_{air} density of air

Operators

$\overline{(\,)}$ time series mean

$(\,)'$ deviation from mean

REFERENCES

Allan, J. D., Alfarra, M. R., Bower, K. N., Williams, P. I., Gallagher, M. W., Jimenez, J. L., McDonald, A. G., Nemitz, E., Canagaratna, M., Jayne, J. T., Coe, H., and Worsnop, D. R. (2003a). Quantitative sampling using an Aerodyne Aerosol Mass Spectrometer: 2. Measurements of fine particulate chemical composition in two U.K. cities. *J. Aerosol Sci.*, 108(D3):4091. doi: 10.1029/2002JD002359.

Allan, J. D., Jimenez, J. L., Williams, P. I., Alfarra, M. R., Bower, K. N., Jayne, J. T., Coe, H., and Worsnop, D. R. (2003b). Quantitative sampling using an Aerodyne Aerosol Mass Spectrometer: 1. Techniques of data interpretation and error analysis. *J. Geophys. Res.*, 108(D3):4090. doi:10.1029/2002JD002358.

Allegrini, I., De Santis, F., Di Palo, V., Perrino, C., Possanzini, M., and Liberti, A. (1987). Annular denuder method for sampling reactive gases and aerosols in the atmosphere. *Sci. Total Environ.*, 67:1–16.

Ammann, M., von Ballmoos, P., Stalder, M., Suter, M., and Brunold, C. (1995). Uptake and assimilation of atmospheric NO_2-N by spruce needles (*Picea abies*): A field study. *Water Air Soil Poll.*, 85:1497–1502.

Baker, L. A., Hope, D., Xu, Y., Edmonds, J., and Lauver, L. (2001). Nitrogen balance for the Central Arizona-Phoenix (CAP) ecosystem. *Ecosystems*, 4:582–602.

Baldocchi, D. D., Hicks, B. B., and Meyers, T. P. (1988). Measuring biosphere-atmosphere exchanges of biologically related gases with micrometeorological methods. *Ecology*, 69:1331–1340.

Baumgardner, Jr, R. E., Lavery, T. F., Rogers, C. M., and Isil, S. S. (2002). Estimates of the atmospheric deposition of sulfur and nitrogen species: Clean Air Status and Trends Network, 1990–2000. *Environ. Sci. Technol.*, 36:2614–2629.

Binkowski, F. S. (1999). Aerosols in Models-3 CMAQ. Technical report, U.S. Environmental Protection Agency, Research Triangle Park, North Carolina.

Binkowski, F. S. and Shankar, U. (1995). The regional particulate matter model: 1. model description and preliminary results. *J. Geophys. Res.*, 100:26191–26209.

Bird, R. B., Stewart, W. E., and Lightfoot, E. N. (2002). *Transport Phenomena*. John Wiley & Sons, New York, 2nd edition.

Brain, J. D. and Valberg, P. A. (1979). Deposition of aerosol in the respiratory tract. *Am. Rev. Respir. Dis.*, 120:1325–1373.

Brockman, J. E. (2001). Sampling and transport of aerosols. In P. A. Baron and K. Willeke, eds., *Aerosol Measurement: Principles, Techniques, and Applications*. Wiley Interscience, New York, 2nd edition.

Brown, S. G., Frankel, A., Raffuse, S. M., Roberts, P. T., Hafner, H. R., and Anderson, D. J. (2007). Source apportionment of fine particulate matter in Phoenix, AZ, using positive matrix factorization. *J. Air Waste Manage. Assoc.*, 57:741–752.

Businger, J. A. (1986). Evaluation of the accuracy with which dry deposition can be measured with current micrometeorological techniques. *J. Clim. Appl. Meteorol.*, 25:1100–1124.

Businger, J. A. and Oncley, S. P. (1990). Flux measurements with conditional sampling. *J. Atmos. Ocean Tech.*, 7:349–352.

Businger, J. A., Wyngaard, J. C., Izumi, Y., and Bradley, E. F. (1971). Flux profile relationships in the atmospheric surface layer. *J. Atmos. Sci.*, 28:181–189.

Buzorius, G., Rannik, ., M kel , J. M., Vesala, T., and Kulmala, M. (1998). Vertical aerosol particle fluxes measured by eddy covariance technique using condensational particle counter. *J. Aerosol Sci.*, 29:157–171.

Campione, M., Walrath, K., and Huml, A. (1998). *The Java Tutorial Continued: The Rest of the JDK*. Prentice Hall, Upper Saddle River, New Jersey.

Canagaratna, M. R., Jayne, J. T., Jimenez, J. L., Allan, J. D., Alfarra, M. R., Zhang, Q., Onasch, T. B., Drewnick, F., Coe, H., Middlebrook, A., Delia, A., Williams, L. R., Trimborn, A. M., Northway, M. J., DeCarlo, P. F., Kolb, C. E., Davidovits, P., and Worsnop, D. R. (2007). Chemical and microphysical characterization of ambient aerosols with the Aerodyne Aerosol Mass Spectrometer. *Mass Spectrom. Rev.*, 26:185–222.

Chamberlain, A. C. (1966). Transport of gases to and from grass and grass-like surfaces. *Proc. Roy. Soc. Ser. A*, 290:236–265.

Chamberlain, A. C. (1967). Transport of lycopodium spores and other small particles to rough surfaces. *Proc. Roy. Soc. Ser. A*, 296:45–70.

Chamberlain, A. C. and Chadwick, R. C. (1953). Deposition of airborne radio-iodine vapor. *Nucleonics*, 8:22–25.

Chow, J. C. (1995). Measurement methods to determine compliance with ambient air quality standards for suspended particles. *J. Air Waste Manage. Assoc.*, 45:320–382.

Clarke, J. F., Edgerton, E. S., and Martin, B. E. (1997). Dry deposition calculations for the Clean Air Status and Trends Network. *Atmos. Environ.*, 31:3667–3678.

Darby, R. (2001). *Chemical Engineering Fluid Mechanics*. Marcel Dekker, New York, 2nd edition.

Davidson, C. I. and Wu, Y. L. (1990). Dry deposition of particles and vapors. In S. E. Lindberg, A. L. Page, and S. A. Norton, eds., *Acidic Precipitation*, volume 3. Springer-Verlag, New York.

Dockery, D. W., Pope III, C. A., Xu, X., Spengler, J. D., Ware, J. H., Fay, M. E., Ferris, Jr., B. G., and Speizer, F. E. (1993). An association between air pollution and mortality in six U. S. cities. *N. Engl. J. Med.*, 329:1753–1759.

Dyer, A. J. and Pruitt, W. O. (1962). Eddy-flux measurements over a small, irrigated area. *J. Appl. Meteor.*, 1:471–473.

Fan, S. M., Wofsy, S. C., Bakwin, P. S., Jacob, D. J., Anderson, S. M., Kebabian, P. L., McManus, J. B., Kolb, C. E., and Fitzjarrald, D. R. (1992). Micrometeorological measurements of CH_4 and CO_2 exchange between the atmosphere and subarctic tundra. *J. Geophys. Res.*, 97:16627–16643.

Fenn, M. E., Haeuber, R., Tonnesen, G. S., Baron, J. S., Grossman-Clarke, S., Hope, D., Jaffe, D. A., Copeland, S., Geiser, L., Rueth, H. M., and Sickman, J. O. (2003). Nitrogen emissions, deposition, and monitoring in the western United States. *Bioscience*, 53:391–403.

Fernandez, I. J. (1990). Effects of acidic precipitation on soil productivity. In D. C. Adriano and A. H. Johnson, eds., *Acidic Precipitation*, volume 2. Springer-Verlag, New York.

Foken, T. and Wichura, B. (1996). Tools for quality assessment of surface-based flux measurements. *Agr. Forest Meteorol.*, 78:83–105.

Foken, T., Wimmer, F., Mauder, M., Thomas, C., and Liebethal, C. (2006). Some aspects of the energy balance closure problem. *Atmos. Chem. Phys.*, 6:4395–4402.

Gallagher, M. W., Beswick, K. M., Duyzer, J., Westrate, H., Choularton, T. W., and Hummelshøj, P. (1997). Measurement of aerosol fluxes to Speulder forest using a micrometeorological technique. *Atmos. Environ.*, 31:359–373.

Gallagher, M. W., Nemitz, E., Dorsey, J. R., Fowler, D., Sutton, M. A., Flynn, M., and Duyzer, J. (2002). Measurements and parameterizations of small aerosol deposition velocities to grassland, arable crops, and forest: Influence of surface roughness length on deposition. *J. Geophys. Res.*, 107(D12). doi:10.1029/2001JD000817.

Galloway, J. N. (1996). Anthropogenic mobilization of sulphur and nitrogen: Immediate and delayed consequences. *Annu. Rev. Energy Environ.*, 21:261–292.

Galloway, J. N., Schlesinger, W. H., Levy II, H., Michaels, A., and Schnoor, J. L. (1995). Nitrogen fixation: Anthropogenic enhancement-environmental response. *Global Biogeochem. Cycles*, 9:235–252.

Giorgi, F. (1988). Dry deposition velocities of atmospheric aerosols as inferred by applying a particle dry deposition parameterization to a general circulation model. *Tellus*, 40B:23–41.

Golder, D. (1972). Relations among stability parameters in the surface layer. *Bound.-Lay. Meteorol.*, 3:47–58.

Gonzales, D. A., Allen, J. O., Smith, K. A., and Worsnop, D. R. (2006). Eddy-correlation measurement of size-segregated and composition-resolved aerosol depositional flux using an aerosol mass spectrometer: Final report. Technical report, U.S. Environmental Protection Agency, Research Triangle Park, North Carolina.

Gormley, P. G. and Kennedy, M. (1949). Diffusion from a stream flowing through a cylindrical tube. *Proc. Roy. Irish Acad. A*, 52:163–170.

Gregg, J. W., Jones, C. G., and Dawson, T. E. (2003). Urbanization effects on tree growth in the vicinity of New York City. *Nature*, 424:183–187.

Grimmond, C. S. B., Souch, C., and Hubble, M. D. (1996). Influence of tree cover on summertime surface energy balance fluxes, San Gabriel Valley, Los Angeles. *Clim. Res.*, 6:45–57.

Harvey, H. H. (1990). Effects of acidic precipitation on lake ecosystems. In D. C. Adriano and A. H. Johnson, eds., *Acidic Precipitation*, volume 2. Springer-Verlag, New York.

Heintzenberg, J. (1989). Fine particles in the global troposphere — a review. *Tellus*, 41B:149–160.

Hering, S. V. and Cass, G. (1999). The magnitude of bias in the measurement of $PM_{2.5}$ arising from volatilization of particulate nitrate from Teflon filters. *J. Air Waste Manage. Assoc.*, 49:725–733.

Hering, S. V. and McMurry, P. H. (1991). Optical counter response to monodisperse atmospheric aerosols. *Atmos. Environ.*, 25A:463–468.

Hicks, B. B. (1970). The measurement of atmospheric fluxes near the surface: A generalized approach. *J. Appl. Meteor.*, 9:386–388.

Hicks, B. B., Baldocchi, D. D., Meyers, T. P., Hosker, Jr, R. P., and Matt, D. R. (1987). A preliminary multiple resistance routine for deriving deposition velocities from measured quantities. *Water Air Soil Poll.*, 36:311–330.

Hicks, B. B., Hosker, Jr, R. P., Meyers, T. P., and Womack, J. D. (1991). Dry deposition inferential measurement techniques—I. Design and tests of a prototype meteorological and chemical system for determining dry deposition. *Atmos. Environ.*, 25:2345–2359.

Hinds, W. C. (1999). *Aerosol Technology: Properties, Behavior, and Measurement of Airborne Particles*. Wiley Interscience, New York, 2nd edition.

Horst, T. W. (1997). A simple formula for attenuation of eddy fluxes measured with first-order-response scalar sensors. *Bound.-Lay. Meteorol.*, 82:219–233.

Jayne, J. T., Leard, D. C., Zhang, X., Davidovits, P., Smith, K. A., Kolb, C. E., and Worsnop, D. R. (2000). Development of an aerosol mass spectrometer for size and composition analysis of submicron particles. *Aerosol Sci. Technol.*, 33:49–70.

Jimenez, J. L., Jayne, J. T., Shi, Q., Kolb, C. E., Worsnop, D. R., Yourshaw, I., Seinfeld, J. H., Flagan, R. C., Zhang, X., Smith, K. A., Morris, J. W., and Davidovits, P. (2003). Ambient aerosol sampling using the Aerodyne Aerosol Mass Spectrometer. *J. Geophys. Res.*, 108(D7):8425. doi:10.1029/2001JD001213.

Kaimal, J. C. and Finnigan, J. J. (1994). *Atmospheric Boundary Layer Flows: Their Structure and Measurement*. Oxford University Press, New York.

Kaimal, J. C. and Gaynor, J. E. (1991). Another look at sonic thermometry. *Bound.-Lay. Meteorol.*, 56:401–410.

Kaimal, J. C., Gaynor, J. E., Zimmerman, H. A., and Zimmerman, G. A. (1990). Minimizing flow distortion errors in a sonic anemometer. *Bound.-Lay. Meteorol.*, 53:103–115.

Kaimal, J. C., Wyngaard, J. C., Izumi, Y., and Coté, O. R. (1972). Spectral characteristics of surface-layer turbulence. *Quart. J. Roy. Meteorol. Soc.*, 98:563–589.

Katen, P. C. and Hubbe, J. M. (1985). An evaluation of optical particle counter measurements of the dry deposition of atmospheric aerosol particles. *J. Geophys. Res.*, 90:2145–2160.

Kiehl, J. T. and Rodhe, H. (1995). Modeling geographical and seasonal forcing due to aerosols. In *Aerosol Forcing of Climate*, pp. 281–296. Wiley, New York.

Latini, M. and Bernoff, A. J. (2001). Transient anomalous diffusion in Poiseuille flow. *J. Fluid Mech.*, 441:399–411.

Lenschow, D. H. and Raupach, M. R. (1991). The attenuation of fluctuations in scalar concentrations through sampling tubes. *J. Geophys. Res.*, 96(D8):15259–15268.

Leuning, R. and Moncrieff, J. (1990). Eddy covariance measurements using open- and closed-path CO_2 analysers: Correction for analyser water vapour sensitivity and damping fluctuations in air sampling tubes. *Bound.-Lay. Meteorol.*, 53:63–76.

Lohse, K. A. (2007). Atmospheric deposition of carbon and nutrients across a desert city. Unpublished data.

Lorenz, R. and Murphy, Jr, C. E. (1989). Dry deposition of particles to a pine plantation. *Bound.-Lay. Meteorol.*, 46:355–366.

Lovett, G. M. (1994). Atmospheric deposition of nutrients and pollutants in North America: An ecological perspective. *Ecol. Appl.*, 4:629–650.

Lovett, G. M. and Lindberg, S. E. (1984). Dry deposition and canopy exchange in a mixed oak forest as determined by analysis of throughfall. *J. Appl. Ecol.*, 21:1013–1027.

Lovett, G. M., Traynor, M. M., Pouyat, R. V., C., M. M., Zhu, W.-X., and Baxter, J. W. (2000). Atmospheric deposition to oak forests along an urban-rural gradient. *Environ. Sci. Technol.*, 34:4294–4300.

Lyons, R. G. (2001). *Understanding Digital Signal Processing*. Prentice Hall, Upper Saddle River, New Jersey.

Massman, W. J. (1991). The attenuation of concentration fluctuations in turbulent flow through a tube. *J. Geophys. Res.*, 96:15269–15273.

Massman, W. J. (2000). A simple method for estimating frequency response corrections for eddy covariance systems. *Agr. Forest Meteorol.*, 104:185–198.

Massman, W. J. and Lee, X. (2002). Eddy covariance flux corrections and uncertainties in long-term studies of carbon and energy exchanges. *Agr. Forest Meteorol.*, 113:121–144.

McMillen, R. T. (1988). An eddy correlation technique with extended applicability to non-simple terrain. *Bound.-Lay. Meteorol.*, 43:231–245.

Meyers, T. P., Finkelstein, P., Clarke, J., Ellestad, T. G., and Sims, P. F. (1998). A multilayer model for inferring dry deposition using standard meteorological measurements. *J. Geophys. Res.*, 103:22645–22661.

Meyers, T. P., Hicks, B. B., Hosker, Jr, R. P., Womack, J. D., and Satterfield, L. C. (1991). Dry deposition inferential measurement techniques—II. Seasonal and annual deposition rates of sulfur and nitrate. *Atmos. Environ.*, 25:2361–2370.

Moore, C. J. (1986). Frequency response corrections for eddy correlation systems. *Bound.-Lay. Meteorol.*, 37:17–35.

Munger, J. W., Wofsy, S. C., Bakwin, P. S., Fan, S. M., Goulden, M. L., Daube, B. C., Goldstein, A. H., Moore, K. E., and Fitzjarrald, D. R. (1996). Atmospheric deposition of reactive nitrogen oxides and ozone in a temperate deciduous forest and a subarctic woodland: 1. Measurements and mechanisms. *J. Geophys. Res.*, 101:12639–12657.

NCSA (2000). *HDF Reference Manual*. National Center for Supercomputing Applications. http://hdf.ncsa.uiuc.edu/.

Nemitz, E., Gallagher, M. W., Duyzer, J. H., and Fowler, D. (2002). Micrometeorological measurements of particle deposition velocities to moorland vegetation. *Quart. J. Roy. Meteorol. Soc.*, 128:2281–2300.

Nemitz, E., Sutton, M. A., Wyers, G. P., Otjes, R. P., Mennen, M. G., van Putten, E. M., and Gallagher, M. W. (2004). Gas-particle interactions above a dutch heathland: II. Concentrations and surface exchange fluxes of atmospheric particles. *Atmos. Chem. Phys.*, 4:1007–1024.

Ollinger, S. V., Aber, J. D., Lovett, G. M., Millham, S. E., Lathrop, R. G., and Ellis, J. M. (1993). A spatial model of atmospheric deposition for the northeastern U.S. *Ecol. Appl.*, 3:459–472.

Oncley, S. P., Businger, J. A., Itsweire, E. C., Friehe, C. A., LaRue, J. C., and Chang, S. S. (1990). Surface layer profiles and turbulence measurements over uniform land under near-neutral conditions. In *Ninth Symposium on Turbulence and Diffusion*, pp. 237–240. American Meteorological Society.

Perry, R. H. and Green, D. W. (1997). *Perry's Chemical Engineers' Handbook*. McGraw-Hill Book Company, New York, seventh edition.

Philip, J. R. (1963a). The damping of a fluctuating concentration by continuous sampling through a tube. *Aust. J. Phys.*, 16:454–463.

Philip, J. R. (1963b). The theory of dispersal during laminar flow in tubes. I. *Aust. J. Phys.*, 16:287–299.

Philip, J. R. (1963c). The theory of dispersal during laminar flow in tubes. II. *Aust. J. Phys.*, 16:300–310.

Pope, C. A., Burnett, R. T., Thun, M. J., Calle, E. E., Krewski, D., Ito, K., and Thurston, G. D. (2002). Lung cancer, cardiopulmonary mortality, and long-term exposure to fine particulate air pollution. *J. Am. Med. Assoc.*, 287(9):1132–1141.

Possanzini, M., Febo, A., and Liberti, A. (1983). New design of a high-performance denuder for the sampling of atmospheric pollutants. *Atmos. Environ.*, 17:2605–2610.

Pressley, S., Lamb, B., Westberg, H., Flaherty, J., Chen, J., and Vogel, C. (2005). Long-term isoprene flux measurements above a northern hardwood forest. *J. Geophys. Res.*, 110(D07301). doi:10.1029/2004JD005523.

Pyne, S. (2002). Small particles add up to big disease risk. *Science*, 295:1994.

Ruijgrok, W., Davidson, C. I., and Nicholson, K. W. (1995). Dry deposition of particles: Implications and recommendations for mapping of deposition over Europe. *Tellus*, 47B:587–601.

Ruijgrok, W., Tieben, H., and Eisinga, P. (1997). The dry deposition of particles to a forest canopy: A comparison of model and experimental results. *Atmos. Environ.*, 31:399–415.

Russell, A. G., McRae, G. J., and Cass, G. R. (1983). Mathematical modeling of the formation and transport of ammonium nitrate aerosol. *Atmos. Environ.*, 17:949–964.

Schery, S. D., Wasiolek, P. T., Nemetz, B. M., Yarger, F. D., and Whittlestone, S. (1998). Relaxed eddy accumulator for flux measurements of nanometer-size particles. *Aerosol Sci. Technol.*, 28:159–172.

Schlesinger, W. H. (1997). *Biogeochemistry: An Analysis of Global Change*. Academic Press, San Diego, 2nd edition.

Schmid, H. P., Grimmond, C. S. B., Cropley, F., Offerle, B., and Su, H. B. (2000). Measurements of CO_2 and energy fluxes over a mixed hardwood forest in the mid-western United States. *Agr. Forest Meteorol.*, 103:357–374.

Schmid, H. P., Su, H. B., Vogel, C. S., and Curtis, P. S. (2003). Ecosystem-atmosphere exchange of carbon dioxide over a mixed hardwood forest in northern lower Michigan. *J. Geophys. Res.*, 108(D14):4417. doi:10.1029/2002JD003011.

Sehmel, G. A. (1980). Particle and gas dry deposition: A review. *Atmos. Environ.*, 14:983–1011.

Sehmel, G. A. and Hodgson, W. H. (1978). A model for predicting dry deposition of particles and gases to environmental surfaces. Technical report, Battelle Pacific Northwest Laboratories, Richland, Washington.

Seinfeld, J. H. and Pandis, S. N. (1998). *Atmospheric Chemistry and Physics: From Air Pollution to Global Change*. Wiley-Interscience, New York.

Shimizu, T. (2007). Practical applicability of high frequency correction theories for CO_2 flux measured by a closed-path system. *Bound.-Lay. Meteorol.*, 122:417–438.

Sievering, H. (1982). Profile measurements of particle dry deposition velocity at an air-land interface. *Atmos. Environ.*, 16:301–306.

Slinn, W. G. N. (1982). Predictions for particle deposition to vegetative canopies. *Atmos. Environ.*, 16:1785–1794.

Solomon, P. A., Fall, T., Salmon, L., and Cass, G. R. (1989). Chemical characteristics of PM10 aerosols collected in the Los Angeles area. *J. Air Pollut. Control Assoc.*, 39:154–163.

Stevens, C. J., Dise, N. B., Mountford, J. O., and Gowing, D. J. (2004). Impact of nitrogen deposition on the species richness of grasslands. *Science*, 303:1876–1879.

Stull, R. B. (1988). *An Introduction to Boundary Layer Meteorology*. Kluwer Academic, Dordrecth, The Netherlands.

Suyker, A. E. and Verma, S. B. (1993). Eddy correlation measurement of CO_2 flux using a closed-path sensor: Theory and field tests against an open-path sensor. *Bound.-Lay. Meteorol.*, 64:391–407.

Taylor, G. I. (1953). Dispersion of soluble matter in solvent flowing through a tube. *Proc. R. Soc. London, Ser. A*, 219:186–203.

Taylor, G. I. (1954). Dispersion of matter in turbulent flow through a pipe. *Proc. R. Soc. London, Ser. A*, 223:446–468.

Tolocka, M. P., Solomon, P. A., Mitchell, W., Norris, G. A., Gemmill, D. B., Wiener, R. W., Vanderpool, R. W., Homolya, J. B., and Rice, J. (2001). East versus West in the US: Chemical characteristics of $PM_{2.5}$ during the winter of 1999. *Aerosol Sci. Technol.*, 34:88–96.

Tyree, C. A. and Allen, J. O. (2004). Diffusional particle loss upstream of isokinetic sampling inlets. *Aerosol Sci. Technol.*, 38:1019–1026.

Velasco, E., Lamb, B., Pressley, S., Allwine, E., Westberg, H., Jobson, B., Alexander, M., Prazeller, P., Molina, L., and Molina, M. (2005). Flux measurements of volatile organic compounds from an urban landscape. *Geophys. Res. Lett.*, 32(L20802). doi:10.1029/2005GL023356.

Vitousek, P. M., Aber, J. D., Howarth, R. W., Likens, G. E., Matson, P. A., Schindler, D. W., Schlesinger, W. H., and Tilman, D. G. (1997a). Human alteration of the global nitrogen cycle: Sources and consequences. *Ecol. Appl.*, 7:737–750.

Vitousek, P. M., Mooney, H. A., Lubchenco, J., and Melillo, J. M. (1997b). Human domination of earth's ecosystems. *Science*, 277:494–499.

Vong, R. J., Vickers, D., and Covert, D. S. (2004). Eddy correlation measurements of aerosol deposition to grass. *Tellus*, 56B:105–117.

Walmsley, J. L. and Wesely, M. L. (1996). Modification of coded parametrizations of surface resistances to gaseous dry deposition. *Atmos. Environ.*, 30:1181–1188.

Watson, J. G., Chow, J. C., Lurmann, F. W., and Musarra, S. P. (1994). Ammonium nitrate, nitric acid, and ammonia equilibrium in wintertime Phoenix, Arizona. *J. Air Waste Manage. Assoc.*, 44:405–412.

Wesely, M. L. (1989). Parameterizations of surface resistance to gaseous dry deposition in regional-scale, numerical models. *Atmos. Environ.*, 23:1293–1304.

Wesely, M. L., Cook, D. R., and Hart, R. L. (1983). Fluxes of gases and particles above a deciduous forest in wintertime. *Bound.-Lay. Meteorol.*, 27:237–255.

Wesely, M. L., Cook, D. R., Hart, R. L., and Speer, R. E. (1985). Measurements and parameterization of particulate sulfur dry deposition over grass. *J. Geophys. Res.*, 90:2131–2143.

Wesely, M. L. and Hicks, B. B. (1977). Some factors that affect the deposition rates of sulfur dioxide and similar gases on vegetation. *J. Air Pollut. Control Assoc.*, 27:1110–1117.

Wesely, M. L. and Hicks, B. B. (2000). A review of the current status of knowledge on dry deposition. *Atmos. Environ.*, 34:2261–2282.

Wesely, M. L., Hicks, B. B., Dannevik, W. P., Frisella, S., and Husar, R. B. (1977). An eddy correlation measurement of particulate deposition from the atmosphere. *Atmos. Environ.*, 11:561–563.

Wesely, M. L., Lenschow, D. H., and Denmead, O. T. (1989). Flux measurement techniques. In D. H. Lenschow and B. B. Hicks, eds., *Global Tropospheric Chemistry: Chemical Fluxes in the Global Atmosphere*, pp. 31–46.

Whitby, K. T. and Cantrell, B. K. (1976). Atmospheric aerosols — characteristics and measurement. In *International Conference on Environmental Sensing and Assessment*, pp. 29–1. Las Vegas, NV.

Zhang, L., Brook, J. R., and Vet, R. (2003). A revised parameterization for gaseous dry deposition in air-quality models. *Atmos. Chem. Phys.*, 3:2067–2082.

Zhang, L., Gong, S., Padro, J., and Barrie, L. (2001). A size-segregated particle dry deposition scheme for an atmospheric aerosol module. *Atmos. Environ.*, 35:549–560.

APPENDIX A

NATIONAL INSTRUMENTS APPLICATION PROGRAM INTERFACE USING JAVA (JNIDAQ)

A.1. Introduction

Fast response measurements of atmospheric variables are required for the eddy correlation method. Measurements of scalars must be synchronized with sonic anemometer measurements in order to calculate eddy correlation fluxes from measurements of the same air parcel. Estimation of water vapor, latent heat, and carbon dioxide fluxes are important in determining atmospheric measurement conditions in order to quality control flux measurements. In this research, water vapor and carbon dioxide fluxes were measured using a sonic anemometer and an infrared gas analyzer (IRGA) (see Chapter 3). A new data acquisition system was developed to record the IRGA voltage outputs, which were then scaled to concentration measurements and synchronized with the sonic anemometer measurements for eddy correlation calculations. A National Instruments data acquisition board and connector block (PCI-6024E and BNC-2110, Austin, TX) were used to acquire the IRGA data.

A new data acquisition program was developed in Java (JRE 1.4.2, Sun Microsystems, Santa Clara, CA) for IRGA data collection. Java was chosen because it is compatible with multithreaded processing and includes support for using Hierarchical Data Format (HDF) files. This program required development of a set of Java methods to access the National Instruments Data Acquisition Application Program Interface (NI-DAQ API). Note that DAQ is common abbreviation for data acquisition. A Java library of the NI-DAQ API was previously not available and the existing NI-DAQ API was a C language library to control National Instruments hardware. Thus, the Java Native Interface (JNI) was used to access the NI-DAQ API from Java based data acquisition programs. The Java-National Instruments Data Acquisition class (jnidaq) was developed to abstract the NI-DAQ API and provide semi-transparent access from Java. Jnidaq mainly serves as a bridging library from Java to the NI-DAQ API functions.

A.2. Jnidaq Design

The jnidaq class makes use of the JNI to access the NI-DAQ API from Java classes. This required special steps, briefly described here, to make the NI-DAQ API accessible (Campione *et al.*, 1998). First, the jnidaq class was written and compiled with methods to abstract the

NI-DAQ functions, creating the jnidaq.class file (see Section A.6). The jnidaq class declares that native methods will be used and includes commands to load the native methods from a shared library (see below). A header file, jnidaq.h, was generated using the javah tool. This header file was then included in the jnidaq.c function library, which acts as a "pipe" between the Java class and the NI-DAQ API. The jnidaq.c program was compiled into a dynamic link library (DLL). Finally, Java classes were written to implement NI-DAQ API functions using the DLL file by creating an instance of the jnidaq class (see Section A.7). Thus, to use the jnidaq class to access the NI-DAQ API, the Java data acquisition program must declare and instance of the jnidaq class and the jnidaq.dll file must be available on the Java CLASSPATH.

A.3. Jnidaq Development History

The first version of jnidaq (jnidaq v0.9) followed the development of the NIDaq class by José Lu s Malaquias at LaSEEB - Instituto de Sistemas e Robótica, Lisbon, Portugal (pt.laseeb.NIDaq; `http://laseeb.isr.ist.utl.pt/NIDaq`), but was modified for several practical reasons. First, the NIDaq class (v1.0, JRE unknown) used C++ to access the NI-DAQ API. Since jnidaq v0.9 was developed using C, significant changes were necessary to convert the NIDaq class. Second, the NIDaq class was tested on different hardware and several NI-DAQ API functions needed for the PCI-6024E were not included. Finally, the NIDaq class used `Buffer` classes (`ShortBuffer`, `DoubleBuffer`, `IntegerBuffer`, and `FloatBuffer`) to accomodate pass-by-reference of primitive data type variables in the NI-DAQ API. Newer versions of Java (JRE 1.4.2 or later) define a native `Buffer` class as containers for primitive data types with subclasses for each data type: `ShortBuffer`, `DoubleBuffer`, `IntBuffer`, `FloatBuffer`, `LongBuffer`, `ByteBuffer`, and `CharBuffer`. Thus, the second version of jnidaq (jnidaq v0.91) uses the Java `Buffer` class for pass-by-reference variables. No difference in program performance is apparent between these two methods for functions requiring pass-by-reference variables.

A.4. Jnidaq Conventions

All of the jnidaq methods and fields, corresponding to NI-DAQ functions and variables, in the current version of jnidaq use the same naming convention and are used in the

same manner as Java methods of an instance of the jnidaq class. The class constructor and several auxilliary functions (e.g. `getActiveDAQ`, `getDAQReady`, `getDeviceNumer`) follow Java programming conventions. To use NI-DAQ API functions requiring pass-by-reference variables, the Java Buffer class corresponding to the appropriate argument type must be declared and allocated with a capacity of 1. The `get` method is used to access data that is returned from a pass-by-reference function. The `clear` method must be used if the pass-by-reference variable is subsequently re-used.

A.5. Jnidaq Distribution

The jnidaq class is intended for open source distribution (see `http://www.fulton.asu.edu/~aerosol`). Most of the NI-DAQ API has been included in the jnidaq class as of the most recent update (March 2006), however, testing was limited to functions appropriate for the hardware (PCI-6024E and BNC-2110) used in development. Further testing on other hardware is the responsibility of end users.

A.6. Class Documentation

Table A.1 is an annotated list of the jnidaq class (jnidaq.java). This defines the jnidaq methods and members, most of which are abstractions of the NI-DAQ API functions.

Table A.1: Jnidaq Function List.

Function	Description
jnidaq[a]	Class constructor.
AI_Change_Parameter	Change analog input parameter.
AI_Check[b]	Status of analog input.
AI_Clear	Clear analog input circuitry.
AI_Configure	Configure input parameters.
AI_Mux_Config	Configure multiplex input parameters.
AI_Read[b]	Read an analog input.
AI_Read_Scan	Read multiple channel analog input.
AI_Setup	Select analog input parameters.
AI_VRead[b]	Read an analog voltage.
AI_VRead_Scan	Read multiple channel voltage input.
AI_VScale	Scale analog input to voltage.
AO_Change_Parameter	Change an analog output parameter.
AO_Configure	Configure output parameters.
AO_Update	Update analog output channels.

Table A.1: Jnidaq Function List (*Continued*).

Function	Description
AO_VScale[b]	Scale voltage to analog output.
AO_VWrite	Write a voltage to analog output.
AO_Write	Write a binary value to analog output.
Calibrate_E_Series	Calibrate E Series device.
Config_Alarm_Deadband	Configure analog input alarm.
Config_ATrig_Event_Message	Configure trigger event.
Config_DAQ_Event_Message	Configure DAQ event.
Configure_HW_Analog_Trigger	Configure hardware trigger.
DAQ_Check[b]	Status of DAQ operation.
DAQ_Clear	Clear DAQ operation.
DAQ_Config	Configure DAQ operation.
DAQ_DB_Config[b]	Configure double-buffered (DB) DAQ.
DAQ_DB_HalfReady[b]	Status of half buffer in DB mode.
DAQ_DB_Transfer[b]	Transfer half buffer in DB mode.
DAQ_Monitor[b]	Return data from DAQ operation.
DAQ_Op	Perform DAQ operation.
DAQ_Rate[b]	Configure DAQ rate.
DAQ_Start	Initiate DAQ operation.
DAQ_StopTrigger_Config	Configure DAQ stop trigger.
DAQ_to_Disk	Initiate DAQ and save to a disk file.
DAQ_VScale	Convert binary data to voltages.
DIG_In_Line[b]	Status of digital line.
DIG_In_Prt[b]	Data from digital line port.
DIG_Line_Config	Configure digital line on a port.
DIG_Out_Line	Set or clear digital line.
DIG_Out_Prt	Write to the digital port.
DIG_Prt_Config	Configure digital port direction.
getActiveDAQ[a]	Checks for active DAQ operation.
getDAQReady[a]	Checks for device ready condition.
Get_DAQ_Device_Info[b]	Retrieve device parameters.
getDeviceNumber[a]	Returns assigned device number.
Get_NI_DAQ_Version[b]	Version of NI-DAQ library.
GPCTR_Change_Parameter	GPCTR parameter.
GPCTR_Config_Buffer	Assign a GPCTR buffer.
GPCTR_Control	Control a GPCTR.
GPCTR_Set_Application	Set GPCTR application.
GPCTR_Watch[b]	Monitor GPCTR status.
Init_DA_Brds[b]	Initialize hardware.
SCAN_Demux	Demultiplex data from SCAN operation.
SCAN_Op	Perform synchronous multi-channel DAQ.
SCAN_Setup	Configure synchronous multi-channel DAQ.
SCAN_Start	Initiate synchronous multi-channel DAQ.
SCAN_to_Disk	Synchronous multi-channel DAQ to disk.
Select_Signal	Choose source and polarity of signal.
Set_DAQ_Device_Info	Change device settings.
Timeout_Config	Establish timeout limit.
WFM_Check[b]	Status of WFM operation.

Table A.1: Jnidaq Function List (*Continued*).

Function	Description
WFM_ClockRate	Set WFM update and delay rates.
WFM_DB_Config	Configure double-buffered (DB) WFM.
WFM_DB_HalfReady[b]	Status of half buffer in DB mode.
WFM_DB_Transfer	Transfers half buffer in DB mode.
WFM_from_Disk	Configure WFM from a disk file.
WFM_Group_Control	Initiate multi-channel WFM.
WFM_Group_Setup	Assign output channel(s) to group.
WFM_Load	Assign waveform buffer to ouput channel(s).
WFM_Op	Initiate WFM operation.
WFM_Rate[b]	Configure WFM rate.
WFM_Scale	Scale waveform to voltage.

[a] Auxiliary methods to facilitate Java data acquisition methods not in NI-DAQ API.
[b] Requires Buffer class variable for pass-by-reference variable(s).

A.7. Example Code

An example data acquisition program (SCANdoubleBuf.java), which was used for IRGA data acquisition during the Salt River 2005 experiment (see Chapter 3) and sampling line aerosol step input experiments (see Chapter 2), is included below.

A.7.1. *DAQinterface Class*

```
//v 1.3
import java.awt.*;
import java.awt.event.*;
import javax.swing.*;
import java.io.*;
import java.util.*;
import java.text.*;

// This program creates a user interface for the user to set up and
// run data acquisition using the jnidaq class and the NI-DAQ API.
// Copyright 2004-2007 Arizona Board of Regents
// Daniel A. Gonzales

public class DAQinterface implements ActionListener {
  // constants
  protected static final String START = "start";
  protected static final String STOP = "stop";
  protected static final String SET = "set";
  protected static final String EXIT = "exit";
  protected static final String PRINT = "print";
  protected static final int MAX_NUM_CHAN = 8;
```

```
/* Setup Window */
// Panels
private static JPanel inputPanel;
private static JPanel channelPanel;
private static JPanel controlPanel;

// Text Fields
private static JTextField studyField;
private static JTextField operatorField;
private static JTextField sourceField;
private static JTextField rateField;
private static JTextField dirField;
private static JTextField[] chanField = new JTextField[MAX_NUM_CHAN];

// Buttons
private static JButton startButton;
private static JButton stopButton;
private static JButton exitButton;
private static JButton setButton;

// Input strings
private String studyName;
private String operatorName;
private String sourceName;
private String[] chanString = new String[MAX_NUM_CHAN];

// Component labels
private static JLabel studyLabel;
private static JLabel operatorLabel;
private static JLabel sourceLabel;
private static JLabel rateLabel;
private static JLabel dirLabel;
private static JLabel chanLabel;
private static JLabel chanDescLabel;

// Channel check boxes
private static JCheckBox[] chanBox = new JCheckBox[MAX_NUM_CHAN];


/* Status Window */
private static JPanel statusPanel;
private static JTextArea statusArea;
private static JScrollPane statusPane;
private static JButton printButton;


// DAQ variables
private Double daqRate;
private short[] chanVector;
private short numChannels = 0;
private short status = 0;
private String fileName;
```

```
// SCANdoubleBuf object
SCANdoubleBuf runDAQ = new SCANdoubleBuf();

// Data directory File
File dirFile;

// Log file printstream

// ISO-date format
Date now;
SimpleDateFormat df = new SimpleDateFormat("yyyyMMdd'T'HHmmss");

// NIDAQ constants and error codes
jnidaqcns constant = new jnidaqcns();
jnidaqerr error = new jnidaqerr();

/************************************************
 Function: addWidgets()
 This function constructs and adds the GUI parts.
 Input: void
 Output:  void
************************************************/
private void addWidgets() {

  /* Setup Window */
  // Create labels and text fields
  operatorField = new JTextField(10);
  operatorLabel = new JLabel("Operator Name", SwingConstants.LEFT);

  sourceField = new JTextField(10);
  sourceLabel = new JLabel("Data Source", SwingConstants.LEFT);

  studyField = new JTextField(10);
  studyLabel = new JLabel("Study Name", SwingConstants.LEFT);

  rateField = new JTextField("1000");
  rateLabel = new JLabel("DAQ Rate (Hz)", SwingConstants.LEFT);

  dirField = new JTextField("d:/saltriver/log/");
  dirLabel = new JLabel("Data Directory", SwingConstants.LEFT);

  chanLabel = new JLabel("Channel", SwingConstants.LEFT);
  chanDescLabel = new JLabel("Variable Name", SwingConstants.LEFT);

  // Create channel components
  for (int i=0; i<MAX_NUM_CHAN; i++) {
    if (i<3) {
      chanBox[i] = new JCheckBox(new Integer(i).toString(),true);
    } else {
      chanBox[i] = new JCheckBox(new Integer(i).toString());
    }
```

```
  chanField[i] = new JTextField(10);
} // end of for ()


// Create control buttons
startButton = new JButton("Start Acquisition");
startButton.setMnemonic(KeyEvent.VK_S);
startButton.setActionCommand(START);

exitButton = new JButton("Exit");
exitButton.setMnemonic(KeyEvent.VK_X);
exitButton.setActionCommand(EXIT);

setButton = new JButton("Set Inputs");
setButton.setMnemonic(KeyEvent.VK_I);
setButton.setActionCommand(SET);

stopButton = new JButton("Stop Acquisition");
stopButton.setMnemonic(KeyEvent.VK_T);
stopButton.setActionCommand(STOP);

// Add components to panels
inputPanel.add(studyLabel);
inputPanel.add(studyField);
inputPanel.add(operatorLabel);
inputPanel.add(operatorField);
inputPanel.add(sourceLabel);
inputPanel.add(sourceField);
inputPanel.add(rateLabel);
inputPanel.add(rateField);
inputPanel.add(dirLabel);
inputPanel.add(dirField);

channelPanel.add(chanLabel);
channelPanel.add(chanDescLabel);
for (int i=0; i<MAX_NUM_CHAN; i++) {
  channelPanel.add(chanBox[i]);
  channelPanel.add(chanField[i]);
} // end of for ()

controlPanel.add(setButton);
controlPanel.add(startButton);
controlPanel.add(stopButton);
controlPanel.add(exitButton);
startButton.setEnabled(false);
stopButton.setEnabled(false);

// Label borders
operatorLabel.setBorder(BorderFactory.createEmptyBorder(5,5,5,5));
sourceLabel.setBorder(BorderFactory.createEmptyBorder(5,5,5,5));
studyLabel.setBorder(BorderFactory.createEmptyBorder(5,5,5,5));
rateLabel.setBorder(BorderFactory.createEmptyBorder(5,5,5,5));
```

```
  dirLabel.setBorder(BorderFactory.createEmptyBorder(5,5,5,5));
  chanLabel.setBorder(BorderFactory.createEmptyBorder(5,5,5,5));

  /* Status Window */
  statusArea = new JTextArea("DAQ Status:\n");
  statusArea.setEditable(false);
  statusPane = new JScrollPane(statusArea);
  statusPane.setPreferredSize(new Dimension(450, 700));
  statusPanel.add(statusPane, BorderLayout.CENTER);

  printButton = new JButton("Print Status Window");
  printButton.setMnemonic(KeyEvent.VK_P);
  printButton.setActionCommand(PRINT);
  statusPanel.add(Box.createRigidArea(new Dimension(450,5)));
  statusPanel.add(printButton);

}


/*************************************************
 Function: actionPerformed(ActionEvent event)
 Implementation of ActionListener interface.
 Listens for ActionEvent from the GUI.
 Input:  ActionEvent event
 Output:  void
*************************************************/
public void actionPerformed(ActionEvent event) {

  if (event.getActionCommand().equals(START)) {
    stopButton.setEnabled(true);

    // start data acquisition
    status = acquireData();
  }

  else if (event.getActionCommand().equals(STOP)) {
    // stop DAQ
    this.stopAcquisition();
    studyField.setEnabled(true);
    operatorField.setEnabled(true);
    sourceField.setEnabled(true);
    rateField.setEnabled(true);
    dirField.setEnabled(true);
    for (int i=0; i<MAX_NUM_CHAN; i++) {
      chanField[i].setEnabled(true);
      chanBox[i].setEnabled(true);
    } // end of for ()
    setButton.setEnabled(true);
    startButton.setEnabled(false);
  }

  else if (event.getActionCommand().equals(SET)) {
```

```
    // sets inputs
    studyField.setEnabled(false);
    operatorField.setEnabled(false);
    sourceField.setEnabled(false);
    rateField.setEnabled(false);
    dirField.setEnabled(false);
    for (int i=0; i<MAX_NUM_CHAN; i++) {
      chanField[i].setEnabled(false);
      chanBox[i].setEnabled(false);
    } // end of for ()
    setButton.setEnabled(false);
    startButton.setEnabled(true);

    // error check inputs
    status = checkInput();

    // write the status log
    this.writeLog();
  }

  else if (event.getActionCommand().equals(EXIT)) {
    if (runDAQ.endFlag == 0) {
      this.stopAcquisition();
    } // end of if ()

    // exit the interface
    System.out.println("Exiting DAQ interface.\n");
    System.exit(0);
  }
  else if (event.getActionCommand().equals(PRINT)) {
    // print the status window to a file
    this.writeStatusWindow();
  }
}


/*************************************************
 Function: writeLog()
 This function writes the log file.
 Input: void
 Output:  void
*************************************************/
private void writeLog() {
  PrintStream logFile = null;
  now = getCurrentTime();

  // set up a log file
  StringBuffer logFileName = new StringBuffer(df.format(now));
  logFileName.append("_log.txt");
  fileName = new String(logFileName);
  try {
    logFile = new PrintStream(new FileOutputStream(new
```

```
                                File(dirFile,fileName)));

    System.out.println("Printing log file to " + fileName);
    logFile.println("StudyName \t" + studyName);
    logFile.println("OperatorName \t" + operatorName);
    logFile.println("DataSource \t" + sourceName);
    logFile.println("DAQrate \t" + daqRate);
    for (int i=0; i<MAX_NUM_CHAN; i++) {
      logFile.println("Channel " + i + "\t" + chanField[i].getText());
    } // end of for ()

  } catch (IOException e) {
    System.err.println("Caught IOException : " + e.getMessage());

  } catch (NullPointerException e) {
    System.err.println("Caught NullPointerException : " +
                       e.getMessage());

  } finally {
    if (logFile != null) {
      System.out.println("Closing log file.");
      logFile.close();
    } else {
      System.out.println("Log file not open.");
    } // end of else
  } // end of finally
}


/************************************************
 Function: writeStatusWindow()
 This function writes the status window to a log
 file.
 Input: void
 Output:  void
************************************************/
private void writeStatusWindow() {
  PrintStream statFile = null;

  // set up a file
  now = getCurrentTime();
  StringBuffer statFileName = new StringBuffer(df.format(now));
  statFileName.append("_stat.txt");
  fileName = new String(statFileName);

  try {
    statFile = new PrintStream(new FileOutputStream(new
                                File(dirFile,fileName)));
    System.out.println("Printing current status window to " +
                       fileName);
    statFile.println(statusArea.getText());
```

```
  } catch (IOException e) {
    System.err.println("Caught IOException : " + e.getMessage());

  } catch (NullPointerException e) {
    System.err.println("Caught NullPointerException : " +
                       e.getMessage());

  } finally {
    if (statFile != null) {
      System.out.println("Closing status log file.");
      statFile.close();
    } else {
      System.out.println("Status log file not open.");
    } // end of else
  } // end of finally
}


/************************************************
 Function: getChanVect(short numChans)
 This function sets the channels selected vector.
 Input: void
 Output:  short status
************************************************/
// Get a vector of the channels to scan
private short getChanVect() {

  // determine number of channels
  for (int i=0; i<chanBox.length; i++) {
    if (chanBox[i].isSelected()) {
      numChannels++;
    }
  }

  chanVector = new short[numChannels];
  chanString = new String[numChannels];
  int space;
  short j = 0;
  for (int i=0; i<MAX_NUM_CHAN; i++) {
    if (chanBox[i].isSelected()) {
      chanVector[i] = j;
      chanString[i] = chanField[i].getText();
      space = chanString[i].indexOf(" ");
      if ((chanString[i].length() < 1) || (space > 0)) {
        System.err.println("Invalid variable name for channel  " + i);
        System.exit(0);
      } // end of if ()

      j++;
    }
  }
  return 0;
```

```
}


/************************************************
 Function: getRate()
 This function gets the DAQ rate entered.
 Input: void
 Output:  short status
************************************************/
// Get a vector of the channels to scan
private short getRate() {
  double tempRate = daqRate.parseDouble(rateField.getText());
  daqRate = new Double(tempRate);
  return 0;
}


/************************************************
 Function: getOperator()
 This function gets the operator name.
 Input: void
 Output:  short status
************************************************/
private short getOperator() {
  operatorName = operatorField.getText();
  return 0;
}



/************************************************
 Function: getStudy()
 This function gets the study name.
 Input: void
 Output:  short status
************************************************/
private short getStudy() {
  studyName = studyField.getText();
  return 0;
}


/************************************************
 Function: getSource()
 This function gets the data source name.
 Input: void
 Output:  short status
************************************************/
private short getSource() {
  sourceName = sourceField.getText();
  return 0;
}
```

```
/************************************************
 Function: getDir()
 This function gets the directory entered.
 Input: void
 Output:  short status
************************************************/
// Get a vector of the channels to scan
private short getDir() {
  try {
    dirFile = new File(dirField.getText());

  } catch (NullPointerException e) {
    System.err.println("Caught NullPointerException: " +
                       e.getMessage());
    System.exit(0);
    status = -1;
  } // end of try-catch

  return status;
}


/************************************************
 Function: getCurrentTime()
 Gets a Date object with the current time.
 Input: void
 Output:  Date now
************************************************/
private Date getCurrentTime() {
  Date currentTime = new Date(System.currentTimeMillis());
  return currentTime;
}


/************************************************
 Function: checkInput()
 Check the user inputs.
 Input: void
 Output:  short status
************************************************/
private short checkInput(){
  // get DAQ rate
  status = getRate();
  if (daqRate.doubleValue() <= 0 || daqRate.doubleValue() > 200000) {
    System.err.println("Rate out of bounds error: " +
                       error.unsafeSamplingFreqError);
    System.exit(0);
  }

  // get the directory input
```

```
  status = getDir();
  if (dirFile.exists() != true) {
    statusArea.append("Directory doesn't exist. Creating
                      directory.\n");
    if (dirFile.mkdirs() != true) {
      System.err.println("Unable to create directory.");
      System.exit(0);
    } else {
      status = 0;
    }
  }

  // get channels to scan
  status = getChanVect();
  if (numChannels == 0) {
    System.err.println("No channels selected!");
    System.exit(0);
  }

  // get operator name
  status = getOperator();

  // get operator name
  status = getStudy();

  // get operator name
  status = getSource();

  return status;
}


/************************************************
 Function: acquireData()
 This function instantiate SCANdoubleBuf object
 and start the data acquisition.
 Input: void
 Output:  short status
************************************************/
//Acquire the data
private short acquireData() {
  // modify necessary DAQ parameters from interface
  runDAQ.directory = dirFile;
  runDAQ.sampRate = daqRate.doubleValue();
  runDAQ.scanRate = daqRate.doubleValue()/10;
  runDAQ.numChans = numChannels;
  runDAQ.chanVect = chanVector;
  runDAQ.chanStrings = chanString;
  runDAQ.operator = operatorName;
  runDAQ.statusArea = statusArea;

  // Data acquisition call
```

```
  statusArea.append("Going to acquire data.\n");
  runDAQ.start();

  return status;
}


/************************************************
 Function: stopAcquisition()
 This function attempts to cleanly stop DAQ.
 Input: void
 Output:  short status
************************************************/
private void stopAcquisition() {
  statusArea.append("Stopping data acquisition.\n");
  runDAQ.stopRun();
  return;
}


/************************************************
 Function: main()
 Sets layout and displays the GUI.
 Input: String[] args
 Output:  void
************************************************/
// main method
public static void main(String[] args) {
  DAQinterface myInterface = new DAQinterface();

  // Set the look and feel.
  try {
    UIManager.setLookAndFeel(
              UIManager.getCrossPlatformLookAndFeelClassName());
  } catch(Exception e) {}

  JFrame setupFrame = new JFrame("Data Acquisition Setup");
  setupFrame.setSize(300, 500);
  inputPanel = new JPanel();
  inputPanel.setLayout(new GridLayout(5, 2));
  channelPanel = new JPanel();
  channelPanel.setLayout(new GridLayout(9, 2));
  controlPanel = new JPanel();
  controlPanel.setLayout(new GridLayout(4, 1));

  JFrame statusFrame = new JFrame("Data Acquisition Status");
  statusFrame.setSize(450, 700);
  statusPanel = new JPanel();
  statusPanel.setLayout(new
                  BoxLayout(statusPanel,BoxLayout.PAGE_AXIS));

  // Add the widgets.
```

```
    myInterface.addWidgets();

    Point lastLocation = setupFrame.getLocation();
    lastLocation.translate(235,0);
    statusFrame.setLocation(lastLocation);

    // Listen to events from buttons.
    startButton.addActionListener(myInterface);
    setButton.addActionListener(myInterface);
    stopButton.addActionListener(myInterface);
    exitButton.addActionListener(myInterface);
    printButton.addActionListener(myInterface);

    startButton.setToolTipText("Start data acquisition.");
    setButton.setToolTipText("Set input parameters.");
    stopButton.setToolTipText("Stop data acquisition.");
    exitButton.setToolTipText("Exit the DAQ interface.");
    rateLabel.setToolTipText("Data acquisition rate (Hz).");
    dirLabel.setToolTipText("Data/Log file directory.");
    chanLabel.setToolTipText("Channel(s) to scan.");

    // Add the panel to the frame.
    setupFrame.getContentPane().add(inputPanel, BorderLayout.NORTH);
    setupFrame.getContentPane().add(channelPanel, BorderLayout.CENTER);
    setupFrame.getContentPane().add(controlPanel, BorderLayout.SOUTH);
    statusFrame.getContentPane().add(statusPanel);

    // Exit when the window is closed.
    setupFrame.setDefaultCloseOperation(JFrame.EXIT_ON_CLOSE);
    statusFrame.setDefaultCloseOperation(JFrame.EXIT_ON_CLOSE);

    // Show the GUI.
    statusFrame.pack();
    statusFrame.setVisible(true);

    setupFrame.pack();
    setupFrame.setVisible(true);
  }
}
```

A.7.2. *SCANdoubleBuf Class*

```
import java.io.*;
import java.awt.*;
import java.awt.event.*;
import javax.swing.*;
import java.text.DecimalFormat;
import java.util.*;
import java.text.*;

// This class provides synchronous NI-DAQ double buffer mode data
```

```
// acquisition on multiple input channels.
// Copyright 2004-2007 Arizona Board of Regents
// Daniel A. Gonzales

public class SCANdoubleBuf extends Thread {
  protected static final int BUFFER_PER_CHAN = 200000;  // 0.4MB per
                                                        // channel

  public static short status = 0,
    device = 1,
    shortDNC = 0,
    acquireGain = 1,
    units = 0,  // 0 = points/second, 1 = seconds/point
    dbModeON = 1,
    dbModeOFF = 0,
    daqStopped = 0,
    numMUXBrds = 0,
    shortHalfReady = 0,
    shortPtsTfr = 0,
    numChans;

  public static volatile short endFlag = 0;

  public static boolean done = false;

  public static double sampRate,
    scanRate,
    gainAdjust = 1.0,
    offset = 0.0,
    sleepTime = 10;

  public static short[] chanVect;
  public static short[] gainVect;

  public static int numPts,
    timeout = 180,
    timeoutOff = -1,
    retrieved = 0;

  public static String[] chanStrings;
  public static String operator;

  // data file
  public static File fileName;
  public static File directory;
  public static SimpleDateFormat dateFormat = new
                SimpleDateFormat("yyyyMMdd'T'HHmmss");

  // NIDaq class Buffers
  private static ShortBuffer deviceNumCode = ShortBuffer.allocate(1);
  private static ShortBuffer halfReady = ShortBuffer.allocate(1);
  private static IntBuffer ptsTfr = IntBuffer.allocate(1);
```

```
private static ShortBuffer acqStopped= ShortBuffer.allocate(1);
private static IntBuffer dataRetrieved = IntBuffer.allocate(1);

private static short sampTB = 0,
  sampInt = 0,
  scanTB = 0,
  scanInt = 0;
private static ShortBuffer sampTimeBase = ShortBuffer.allocate(1);
private static ShortBuffer sampInterval = ShortBuffer.allocate(1);
private static ShortBuffer scanTimeBase = ShortBuffer.allocate(1);
private static ShortBuffer scanInterval = ShortBuffer.allocate(1);

private static jnidaq myJnidaq = new jnidaq(device);

// variable arrays
short[] buffer;
short[] halfBuffer;

short[][] chanBuffer;
double[][] chanVoltBuffer;

JTextArea statusArea;

PrintWriter dataOut = null;

/************************************************
 Function: setup()
 Setup data buffers and DAQ hardware settings.
 Input: void
 Output:  short status
************************************************/
public short setup() {
  buffer = new short[numPts];
  halfBuffer = new short[numPts/2];

  chanBuffer = new short[numChans][];
  chanVoltBuffer = new double[numChans][];

  for (int i=0; i<numChans; i++) {
    chanBuffer[i] = new short[numPts/numChans/2];
    chanVoltBuffer[i] = new double[numPts/numChans/2];
  } // end of for ()


  // all gains are 1
  gainVect = new short[numChans];
  for (int i=0; i<numChans; i++) {
    gainVect[i] = 1;
  } // end of for ()

  /* Initialize DAQ Board */
  status = myJnidaq.Init_DA_Brds(deviceNumCode);
```

```
if (status != 0) {
  System.err.println("InitDABrds error: " + status);
  System.exit(0);
} else {
  statusArea.append("DeviceNumberCode = " + deviceNumCode.get(0) +
                    "\n");
} // end of else

/* Rate Setup */
sampTimeBase.clear();
sampInterval.clear();
scanTimeBase.clear();
scanInterval.clear();
status = myJnidaq.DAQ_Rate(sampRate, units, sampTimeBase,
                           sampInterval);
if (status != 0) {
  System.err.println("DAQRate error: " + status);
  System.exit(0);
} else {
  statusArea.append("sampRate = " + sampRate + "\n");
} // end of else

status = myJnidaq.DAQ_Rate(scanRate, units, scanTimeBase,
                           scanInterval);
if (status != 0) {
  System.err.println("SCANRate error: " + status);
  System.exit(0);
} else {
  statusArea.append("scanRate = " + scanRate + "\n");
} // end of else


/* Scan Setup */
status = myJnidaq.SCAN_Setup(numChans, chanVect, gainVect);
if (status != 0) {
  System.err.println("SCANSetup error: " + status);
  System.exit(0);
} else {
  statusArea.append("SCANSetup done.\n");
} // end of else


// Set timeout limit
status = myJnidaq.Timeout_Config(timeout);
if (status != 0) {
  System.err.println("TimeoutConfig ON error: " + status);
  System.exit(0);
} else {
  statusArea.append("TimeoutConfig done.\n");
} // end of else

// Turn ON software double-buffered mode.
```

```
  status = myJnidaq.DAQ_DB_Config(dbModeON);
  if (status != 0) {
    System.err.println("DAQDBConfig ON error: " + status);
    System.exit(0);
  } else {
    statusArea.append("Double Buffer mode on.\n");
  } // end of else

  return status;
}


/************************************************
 Function: getFileName()
 This function creates data file name
 based on the current ISO-8601 date and time.
 Input: void
 Output:  short status
************************************************/
private short getFileName() {
  // Data file name based on ISO-8601 date and time notation.
  Date now = new Date(System.currentTimeMillis());

  StringBuffer datFileName = new StringBuffer(dateFormat.format(now));
  datFileName.append("_dat.txt");
  try {
    fileName = new File(directory, datFileName.toString());
    statusArea.append("Data will be saved in " +
                      fileName.getAbsolutePath() + "\n");
  } catch (NullPointerException e) {
    System.err.println("Caught NullPointerException " +
                       e.getMessage());
    return -1;
  } // end of try-catch

  return 0;
}


/************************************************
 Function: run()
 Implementation of Thread.run to start DAQ thread.
 Input: void
 Output:  void
************************************************/
public void run() {
  //Thread thisThread = Thread.currentThread();
  numPts = BUFFER_PER_CHAN * numChans;

  long startTime = 0,
    doneTime = 0,
    lastTime = 0;
```

```
// setup data buffers and DAQ hardware
status = setup();
if (status != 0) {
  System.err.println("Setup failed.");
  System.exit(0);
}

// get the data file
status = getFileName();
if (status != 0) {
  System.err.println("File name failed.");
  System.exit(0);
}

try {
  dataOut = new PrintWriter(new BufferedWriter(new
                            FileWriter(fileName)));
  System.out.println("Printing data file to " + fileName.getName());
  dataOut.println("% " + fileName.getName());
  dataOut.println("% Data generated by " + operator);
  dataOut.println("% Starting at " +
                  fileName.getName().substring(0,15));\
  dataOut.print("% ");
  for (int i = 0; i<numChans; i++) {
    dataOut.print(chanStrings[i] + "\t");
  } // end of for ()
  dataOut.println();

  startTime = System.currentTimeMillis();
  lastTime = startTime;

  /* Acquire data from multiple channels. */
  status = myJnidaq.SCAN_Start(buffer, numPts,
                               sampTimeBase.get(0),
                               sampInterval.get(0),
                               scanTimeBase.get(0),
                               scanInterval.get(0));
  if (status != 0) {
    System.err.println("SCANStart failed. Error " + status);
    System.exit(0);
  } else {
    statusArea.append("SCAN started.\n");
  }

  // Loop until stopButton clicked
  while ((done == false) && (status == 0)) {
    if (endFlag != 0) {
      done = true;
    } // end of if ()

    halfReady.clear();
```

```
acqStopped.clear();
status = myJnidaq.DAQ_DB_HalfReady(halfReady,acqStopped);
if ((halfReady.get(0) == 1) && (status == 0)) {

  ptsTfr.clear();
  acqStopped.clear();
  status = myJnidaq.DAQ_DB_Transfer(halfBuffer, ptsTfr,
                                    acqStopped);
  if (status != 0) {
    System.err.println("DAQDBTransfer failed. Error " + status);
    System.exit(0);
  } else {
    statusArea.append("\nHalf Buffer Transferred.\n");
    statusArea.append(ptsTfr.get(0) + " points transferred.\n");
    doneTime = System.currentTimeMillis();
    statusArea.append("Buffer acquisition time " +
                      (doneTime-lastTime)/1000 + " s\n");
    statusArea.append("Total acquisition time " +
                      (doneTime-startTime)/1000 + " s\n");
    lastTime = System.currentTimeMillis();
  }

  /* Rearrange the buffer */
  status = myJnidaq.SCAN_Demux(halfBuffer, ptsTfr.get(0),
                               numChans, numMUXBrds);
  if (status != 0) {
    System.err.println("SCANDemux failed. Error " + status);
    System.exit(0);
  } else {
    statusArea.append("Data de-multiplexed.\n");
  }

  /* Put data into channel vectors */
  for (int i=0; i<numChans; i++) {
    System.arraycopy(halfBuffer,i*chanBuffer[i].length,
                     chanBuffer[i],0,chanBuffer[i].length);
  } // end of for ()


  /* Scale binary data */
  for (int i=0; i<numChans; i++) {
    status = myJnidaq.DAQ_VScale((short)i, acquireGain,
                                 gainAdjust, offset,
                                 chanBuffer[i].length,
                                 chanBuffer[i],
                                 chanVoltBuffer[i]);
  } // end of for ()
  if (status != 0) {
    System.err.println("DAQVScale failed. Error " + status);
    System.exit(0);
  } else {
    statusArea.append("Data scaled to voltages.\n");
```

```
    } // end of else


    /* Print the data to the output file */
    DecimalFormat decFormat = new DecimalFormat("##0.000");
    for (int j = 0; j < chanBuffer[0].length; j++) {
      for (int i=0; i<numChans; i++) {
        dataOut.print(decFormat.format(
                      chanVoltBuffer[chanVect[i]][j]) + "\t");
      } // end of for ()
      dataOut.println();
    }

    // flush the data to the file
    statusArea.append("Flushing data buffer.\n");
    dataOut.flush();
    Date now = new Date(System.currentTimeMillis());
    StringBuffer currentTime = new
                 StringBuffer(dateFormat.format(now));
    statusArea.append("Buffer flushed at  " + currentTime +
                      ".\n\n");
  }
  else {
    try {
      sleep((int)sleepTime);
    } catch (InterruptedException e) {
      System.err.println("Caught InterruptedException " +
                         e.getMessage());
    } // end of try-catch
  }

}

// close the data file
dataOut.close();

statusArea.append("Continuous acquisition is done!\n");
/* Make sure DAQ is done */
status = myJnidaq.DAQ_Clear();
if (status != 0) {
  System.err.println("DAQClear error:  " + status);
} else {
  statusArea.append("DAQ Cleared.\n");
} // end of else


/* Turn off double buffer mode */
status = myJnidaq.DAQ_DB_Config(dbModeOFF);
if (status != 0) {
  System.err.println("DAQDBConfig OFF error: " + status);
} else {
  statusArea.append("Double Buffer mode off.\n");
```

```
    } // end of else


    /* Disable timeouts.*/
    status = myJnidaq.Timeout_Config(timeoutOff);
    if (status != 0) {
      System.err.println("Timeout OFF error: " + status);
    } else {
      statusArea.append("Timeout off.\n");
    } // end of else

  } catch (IOException e) {
    System.err.println("Caught IOException : " + e.getMessage());
    System.exit(0);
  } finally {
    if (dataOut != null) {
      System.out.println("Closing data log file.");
      dataOut.close();
    } else {
      System.out.println("Data log file not open.");
    } // end of else
  } // end of finally

}


/************************************************
 Function: stopRun()
 Stop data acquisition.
 Input: void
 Output:  short status
************************************************/
public void stopRun() {
  endFlag = 1;
  return;
}


/************************************************
 Function: toString()
 Print some interesting things about this object.
 Input: void
 Output:  void
************************************************/
public static String toString(String[] args) {
  StringBuffer parameters = new StringBuffer();

  parameters.append("Device: ");
  parameters.append(new Short(device).toString());
  parameters.append("\n");

  parameters.append("Sampling Rate: ");
```

```
    parameters.append(new Double(sampRate).toString());
    parameters.append("\n");

    parameters.append("Number of Channels: ");
    parameters.append(new Short(numChans).toString());
    parameters.append("\n");

    parameters.append("Channels Scanned: ");
    for (int i = 0; i<numChans; i++) {
      parameters.append(new Short(chanVect[i]).toString());
      parameters.append("\n");
    } // end of for ()

    return parameters.toString();
  }
}
```

APPENDIX B

DENUDER AND FILTER SAMPLER OPERATING PROCEDURES

B.1. Introduction

Atmospheric dry deposition fluxes, F, were inferred from measurements of atmospheric concentration, c, and estimates of deposition velocity, v_d (Hicks *et al.*, 1987; Wesely, 1989; Lovett, 1994) (see Chapter 4). The denuder and filter sampler (DFS) described here was used for the measurement of gaseous and particulate phase carbon and nitrogen species relevant to atmospheric deposition. The sampler was designed to reduce artifacts caused by volatilization of the collected particles (Hering and Cass, 1999). The denuders collected gas phase nitric acid (HNO_3) and ammonia (NH_3). The filter samples were collected in two size fractions: particulate matter with diameter, D_p, less than 10 μm (PM_{10}) and particulate matter with diameter less than 2.5 μm ($PM_{2.5}$) which have significantly different v_d values. The denuder and filter samples were then analyzed to determine the concentration of gaseous and particulate carbon and nitrogen.

B.2. Denuder and Filter Sampler

Samples were collected using a DFS consisting of two sampling trains, each with a size-selective cyclone inlet, two annular denuders and a three-stage filter pack (Figures B.1 and B.2). The cyclone inlets had a 50% cutpoint diameter of 2.5 μm (2000-30EH, URG, Chapel Hill, NC) and 10 μm (2000-30ENB, URG), to facilitate calculation of fine (D_p < 2.5 μm) and coarse (D_p 2.5–10 μm) particulate nitrogen concentrations. The designed flow through the DFS assemblies was 16.7 l min^{-1} to achieve the cyclone cutpoint diameter; this was controlled using a vacuum pump and a critical orifice. The flow rate for each DFS sampling train was measured before and after the start of the sampling period using a calibrated rotameter to be within 10% of the design flow rate. The flow rate for each sample was taken to be the average of the flows measured before and after each sampling period.

A laminar flow air stream was drawn through the annular denuders (2000-30x242-3CSS, URG) in series: the first was coated with citric acid to collect ammonia gas (NH_3) and the second was coated with sodium carbonate (Na_2CO_3) to collect nitric acid vapor (HNO_3) (Possanzini *et al.*, 1983; Allegrini *et al.*, 1987). Gas phase materials diffuse to the walls and

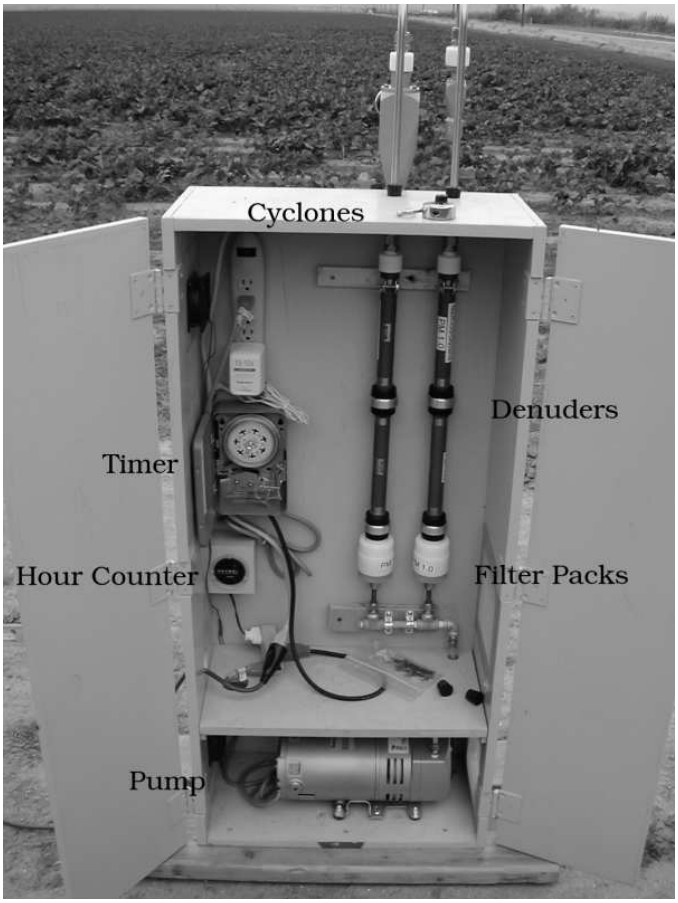

Figure B.1: Picture of the filter and annular denuder bank sampler.

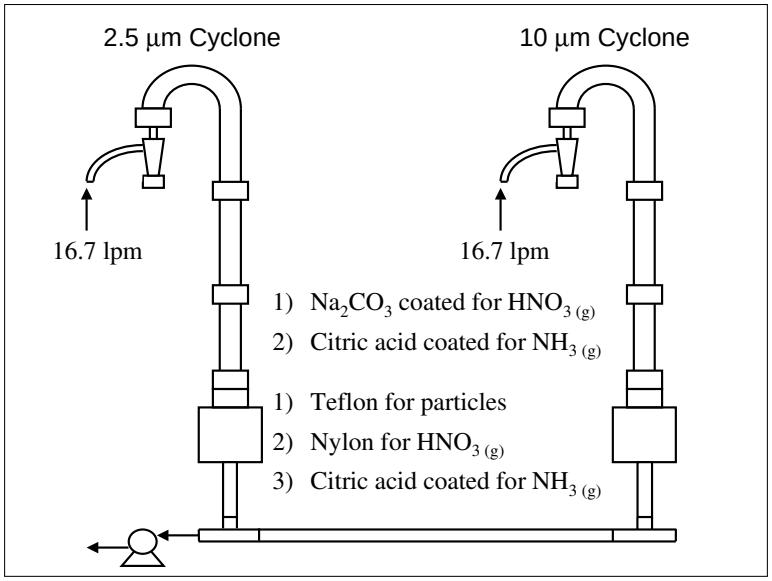

Figure B.2: Schematic of the filter and annular denuder bank sampler for collection of atmospheric carbon and nitrogen compounds.

become chemically sorbed. Particles have a diffusion coefficient 3-6 orders of magnitude lower than that of gases and pass through the denuder (Allegrini *et al.*, 1987).

Air then flowed into the filter pack (2000-30F, URG), which contained three filters: Teflon filter for particulate nitrate (NO_3^-) and ammonium (NH_4^+), nylon afterfilter for volatilized particulate HNO_3, and citric-acid-impregnated Teflon afterfilter for volatilized particulate NH_3 (Allegrini *et al.*, 1987). Quartz fiber filters (pre-baked at 600 °C for 12 hours) were also used in place of Teflon filters so that aerosol carbon could also be measured. Collection of gas phase HNO_3 and NH_3 using denuders and afterfilters is designed to reduce bias due to volatilization of particulate NH_4NO_3 from Teflon filters (Hering and Cass, 1999). Particulate NH_4NO_3 volatilization increases with increasing temperature (Russell *et al.*, 1983).

The DFS was mounted in a weather-proof wooden box with access holes for the size-selective cyclones and two cooling fans. An automatic timer was used to control sample duration and an hour counter was used to measure the actual sample duration to within 0.1 h.

The denuders and filters were extracted with 0.01 l of deionized (DI) water and the extracts were analyzed for NO_3^- and NH_4^+ in the Goldwater Environmental Laboratory. Atmospheric concentrations were calculated as

$$c = \frac{c_{\text{ext}}\, V_{\text{ext}}}{\dot{V}\, t} \tag{B.1}$$

where c_{ext} is the concentration of analyte in the extract, V_{ext} is the volume of the extracted sample, $\dot{V}$ is the volumetric flow rate of the DFS, and t is the sampling time. The DFS operating procedure was designed to collect samples such that c was greater than 10 times the minimum detection limit (MDL) of the analysis instrument to ensure sufficient material for analysis. The atmospheric detection limit (ADL) is the minimum atmospheric concentration detectable based on the MDL of the instrument. The MDL and ADL values for NO_3^- and NH_3 are given in Table B.1 for the analytical equipment used here.

Method blanks were prepared for each sampling date. Method blanks were collected by coating clean denuders with the same solution used for that sample date and loading new filters in a filter pack. The denuders and filters were then extracted using the same procedure

Table B.1: Minimum Detection Limits and Atmospheric Detection Limits for Denuder and Filter Sampler.

Analyte	Minimum Detection Limit (MDL) (ppm)	Atmospheric Detection Limit (ADL) (μg m^{-3})
NO_3^-	0.00085	3.5×10^{-3}
NH_4^+	0.003	1.2×10^{-2}

as normal samples. Method blank extracts were handled, stored, and analyzed in the same manner as normal samples.

B.3. Denuder and Filter Sampler Operation Overview

The DFS were used to collect 24 hour samples from midnight to midnight once every six days, corresponding to the U.S. EPA schedule for collection of particulate matter samples. Samples were collected by noon on the day following a collection period in order to prevent volatilization artifacts after sampling. The denuder and filter samples were then extracted and prepared for the next sample. Procedures used for the DFS were based on the denuder and filter pack manufacturer's instructions (`http://www.urgcorp.com`) and are outlined below.

B.3.1. *Field Equipment List*

To facilitate these tasks, the following equipment was necessary when collecting samples and preparing the DFS for the subsequent sampling period.

- Tools
  - 5/8" wrench
  - 7/16" wrench
  - Rotameter
- Spare Parts
  - Annular denuder
  - Graphite vane vacuum pump

- Filter Media: Teflon (or pre-baked quartz), nylon, and citric-acid-impregnated Teflon.
- Coating Solutions
  - 2% Citric acid in methanol: 100 ml
  - 1% Sodium Carbonate - 1% Glycerol in 1:1 methanol:water: 100 ml
- Extraction and Cleaning Solutions
  - Nanopure DI water: 1500 ml
  - Methanol: 350 ml

B.4. Solution Preparation

B.4.1. *2% Citric Acid Solution*

1. Weigh 2 g of citric acid and transfer to a cleaned 120 ml jar.
2. Add 100 ml of methanol to the jar and dissolve the citric acid by agitation.
3. Label the jar with the date and contents. Refrigerate solution for up to 30 days.

B.4.2. *1% Sodium Carbonate - 1% Glycerol Solution*

1. Weigh 1 g of Na_2CO_3 and transfer to a cleaned 120 ml jar.
2. Add 50 ml of nanopure DI water to the jar and dissolve the Na_2CO_3 by agitation. Sonicate for 5-10 min if necessary.
3. Add 1 ml of glycerol and 50 ml of methanol and mix until dissolved. Sonicate if necessary for 5-10 min. Solution may fizz as glycerol dissolves.
4. Label the jar with the date and contents. Refrigerate solution for up to one week.

B.5. Denuder Cleaning and Coating

1. Rinse with DI water: Cap one end and add 10-20 ml of water to the denuder. Cap the other end and rotate it for about 1 min, then discard the water. Repeat 4 times.
2. Allow to drain and air dry for a few minutes.

3. Rinse twice with about 5 ml of methanol in the same manner as for DI water.
4. Allow to drain and air dry completely. To expedite drying, assemble the denuders and connect the assembly to a tank of ultra-high purity nitrogen. Flow nitrogen at $\approx 2\,\mathrm{l\,min^{-1}}$ for 2-3 minutes.
5. Cap the end of the denuder that is not recessed from the edge.
6. Add 5 ml of coating solution and cap the other end.
7. Rotate gently for 30-40 seconds to coat the entire surface.
8. Empty the solution into the appropriate waste container and repeat with another 5 ml of coating solution.
9. Allow to drain and air dry completely. To expedite drying, assemble the denuders and connect the assembly to a tank of ultra-high purity nitrogen. Flow nitrogen at $\approx 2\,\mathrm{l\,min^{-1}}$ for 2-3 minutes.
10. Cap and store until ready to install in the sampler.

B.6. Filter Coating

1. Use tweezers to place Teflon filter in a clean Petri dish.
2. Add 1 ml of coating solution (2% citric acid in methanol) to the Petri dish.
3. Agitate for 30 seconds to completely cover the filter.
4. Decant the solution into the appropriate waste container.
5. Allow filters to air dry in the Petri dish for 10-15 min. Store filters in the dry Petri dish or load directly into filter packs.

B.7. Filter Pack Assembly

1. Remove the Delrin outer sleeve from the filter pack. Place the sleeve upside down on a flat surface to be used as a stand to assemble the remaining parts.

2. Place the aluminum housing outlet upside down on the sleeve.
3. Place a Teflon spacer on the aluminum housing with the O-ring down and snap into place.
4. Place a support screen on the Teflon spacer, making sure the side with the larger holes is oriented toward the flow, next to the filter.
5. Place the citric-acid-coated filter on the support screen.
6. Place another Teflon spacer on the filter with the O-ring down and snap into place.
7. Place another support screen on the Teflon spacer, making sure the side with the larger holes is oriented toward the flow, next to the filter.
8. Place the Nylon filter on the support screen.
9. Place another Teflon spacer on the filter with the O-ring down and snap into place.
10. Place another support screen on the Teflon spacer, making sure the side with the larger holes is oriented toward the flow, next to the filter.
11. Place the Teflon filter on the support screen.
12. Place the filter housing inlet on top of the filter and snap into place.
13. Turn the Delrin sleeve upright, slide the assembled filter pack into the sleeve and thread the pieces together.

B.8. Denuder and Filter Sampler Assembly

1. Connect the sodium-carbonate-coated denuder to the filter pack inlet using a black adapter ring. Orient the denuder with the flow straightening section (glass annuli recessed by 1 in) toward the incoming flow.
2. Connect the citric-acid-coated denuder to the sodium-carbonate-coated denuder using another adapter ring. Orient the denuder with the flow straightening section (glass annuli recessed by 1 in) toward the incoming flow.

3. Attach the assembled parts to the flow manifold at the bottom of the enclosure using 11/16” and 5/8” wrenches.

4. Push the denuders into the spring clips near the top of the enclosure to hold them in place.

5. Attach the $PM_{2.5}$ cyclone to the U-shaped stainless steel tubing and connect through the hole in the top of the enclosure to the top of the denuder with a URG adapter.

6. Attached the PM_{10} cyclone to the U-shaped stainless steel tubing to the denuder, then connect the cyclone. The PM_{10} cyclone is larger and heavier; secure it to the extra clamp on the outside of the enclosure.

7. Unscrew the dust collector at the bottom of the cyclone and remove any collected material.

B.9. Denuder and Filter Sampler Operation

1. Connect the extension cord from a power supply to the 3-way splitter, which provides constant power to the cooling fans and the timer.

2. Set the timer to the current day and time by turning the dial.

3. Set the sampling time by pushing in the pins around the dial that correspond to the desired sampling period. Each pin corresponds to 2 hours; be sure only the pins for the correct time are pushed in.

4. Test the flow rate through the cyclone by connecting the rotameter to the cyclone inlet using rubber tubing and manually turning on the timer (silver lever). The flow rate should be within 10% of the 16.7 l min^{-1} design value. Note the measured flow rate.

5. Note the reading on the hour counter once the setup is complete. The hour counter will reflect the total sampling time with a precision of 0.1 h.

B.9.1. *Troubleshooting*

The main sources of operating error are due to the power supply or flow through the sampler. The following are *brief* troubleshooting procedures for these problems.

- No Power to the Pump

    1. Check that the main power supply, where the extension cord is plugged, has power. Use the vacuum pump or another device that is known to be functioning. If the cooling fans are running, the problem is not the main power supply.
    2. Check the connections from the extension cord to the timer. Use a fan or other functioning device to make sure there is power from the timer when it is turned on.

- Low or No Flow Through the Cyclone

    1. If the pump runs, but the flow is low, check the cyclone inlets for obstructions. If there are no obstructions, check the critical orifices and the flow manifold itself for debris. Also check for loose connections, following the flow from the cyclone to the pump.
    2. If power to the pump is okay (above), the pump has probably failed and should be replaced with the spare.

B.10. Denuder and Filter Sample Collection

1. Verify the flow rate using the same setup described above.
2. Remove the cyclone inlets then the denuder and filter pack assemblies.
3. Record the reading on the hour counter and calculate the sampling time. If the sampling time is not approximately 24 hours, record the elapsed time and troubleshoot the system to determine what caused the failure.

B.11. Denuder Sample Extraction

1. Cap one end of the denuder and add 5 ml of nanopure DI water to the denuder.

2. Cap the other end and rotate gently for 30-40 seconds.
3. Decant the extract into a clean test tube.
4. Add a second 5 ml portion of nanopure DI water to the denuder and repeat the previous two steps.
5. Cap the test tube and refrigerate the extract until analysis.

B.12. Filter Sample Extraction

1. Use cleaned tweezers to remove filter from filter pack and place filter in a clean test tube.
2. Add 10 ml of nanopure DI water to the test tube with the filter and cap the test tube.
3. Sonicate for 10 min.
4. Refrigerate the extract until analysis.

B.13. Sample Analysis Preparation

The majority of the preparation is for the ammonium samples (acid-coated denuders and acid-coated filters). This is because the acid used to capture the ammonia interferes with the analysis methods and high ammonia concentrations may be present in these samples. First, the samples should be diluted 1:10 using nanopure DI water. Use a pipettor to add 1 ml to the analysis container, then add 9 ml of nanopure DI water to the container or smaller volumes if needed.

Next, the pH must be adjusted to ≈ 7 using a concentrated solution of NaOH. The neutralizing solution must be concentrated to minimize the volume added to the sample and avoid unnecessary dilution. Ideally, an extra blank can be used to determine the approximate volume of NaOH solution needed, then add this volume of neutralizing solution to each sample and verify pH = 7. The more time consuming method is to adjust each sample manually:

1. Using a clean glass pipette, add concentrated NaOH to the extracted sample one drop at a time.

2. Check the pH after each drop and repeat until pH = 7.

3. Record the approximate volume of NaOH solution added to neutralize the sample.

B.14. Nomenclature

Variables

F	flux
v_d	deposition velocity
c	atmospheric concentration
c_{ext}	concentration in the extract
D_a	aerodynamic diameter
V_{ext}	extract volume
$\dot{V}$	volumetric flow rate
t	sampling time

APPENDIX C

INFERENTIAL FLUX MEASUREMENT CALCULATIONS

C.1. Introduction

Atmospheric dry deposition fluxes, F, were inferred from measurements of atmospheric concentration, c, and estimates of deposition velocity, v_d (Hicks *et al.*, 1987; Wesely, 1989; Lovett, 1994) (see Chapter 4). The procedure described here was used to calculate atmospheric fluxes from gaseous and particulate nitrogen concentrations measured using the denuder and filter sampler (DFS) described in Appendix B and deposition velocities estimated from meteorological measurements.

C.2. Gaseous and Particulate Nitrogen Concentrations

Atmospheric concentrations of materials collected with each denuder and filter were calculated as

$$c = \frac{c_{\text{ext}}\, V_{\text{ext}}}{\dot{V}\, t} \tag{C.1}$$

where c_{ext} is the concentration of analyte in the extract, V_{ext} is the volume of the extracted sample, $\dot{V}$ is the volumetric flow rate of the DFS, t is the sampling time, and c has units of μg N m^{-3}. Subscript notation for the sample concentrations are summarized in Table C.1. The concentrations, with units of μg N m^{-3}, of ammonia gas (NH_3), nitric acid vapor (HNO_3), coarse and fine particulate ammonium (NH_4^+), and coarse and fine particulate nitrate (NO_3^-) were then calculated as

$$\begin{aligned}
c_{\text{NH}_3} &= \left(c_{\text{c,AD,NH}_3} + c_{\text{f,AD,NH}_3}\right)/2 \\
c_{\text{HNO}_3} &= \left(c_{\text{c,CD,HNO}_3} + c_{\text{f,CD,HNO}_3}\right)/2 \\
c_{\text{c,NH}_4^+} &= c_{\text{c,TF,NH}_4^+} + c_{\text{c,AF,NH}_4^+} \\
c_{\text{f,NH}_4^+} &= c_{\text{f,TF,NH}_4^+} + c_{\text{f,AF,NH}_4^+} \\
c_{\text{c,NO}_3^-} &= c_{\text{c,TF,NO}_3^-} + c_{\text{c,NF,NO}_3^-} \\
c_{\text{f,NO}_3^-} &= c_{\text{f,TF,NO}_3^-} + c_{\text{f,NF,NO}_3^-}
\end{aligned}$$

Measurements of gas concentrations from the coarse and fine sampling trains were within 10% of each other for all of the samples used here. Method blanks were subtracted from all samples and sample concentrations below the absolute value of the atmospheric detection limit were reported as 0 μg N m^{-3}.

Table C.1: Subscript Notation for Atmospheric Concentrations Measured Using Denuder and Filter Samplers

Sampling Train		
	c	coarse
	f	fine
Sample		
	CD	sodium-carbonate-coated denuder
	AD	citric-acid-coated denuder
	TF	Teflon filter
	NF	nylon afterfilter
	AF	citric-acid-impregnated afterfilter
Analyte		
	NH_3	gaseous NH_3
	HNO_3	gaseous HNO_3
	NH_4^+	particluate NH_4^+
	NO_3^-	particulate NO_3^-

C.3. Meteorological Data

Meteorological variables were measured from meteorological towers at the intensive measurement sites (see Chapter 4). At the Desert Botanical Garden (DBG) site a 10 m tower and meteorological sensors were installed. At the Lost Dutchman State Park (LDP) site meteorological sensors were installed on an existing 10 m tower. Wind speed, U and direction, θ, at 10 m were measured using a propeller-type anemometer (05103-L, R.M. Young, Co., Traverse City, MI). Air temperature, T, and relative humidity, RH, were measured using a Vaisala probe (HMP45C-L, Vaisala, Inc., Woburn, MA). Solar radiation, Q_*, was measured using a silicon pyranometer (CS300-L, Apogee Instruments, Inc., Roseville, CA). Precipitation was measured using a tipping bucket rain gauge (TE525WS-L, Texas Electronics, Inc., Dallas, TX). Continuous measurements of U, θ, T, RH, and Q_* were recorded as ten minute averages using a data logger (CR1000, Campbell Scientific, Inc., Logan, UT). Total precipitation was recorded for each ten minute period. Ten-minute data was subsequently averaged (or summed for precipitation) to hourly data.

Meteorological measurements for the White Tank Mountain (WTM) site were obtained from the Waddell, Arizona, meteorological station approximately 4 km northeast of the WTM

site. Hourly averages and totals of the same meteorological variables above were retrieved from the Arizona Meteorological Network website (`http://ag.arizona.edu/azmet/`).

Using 3 months of micrometeorological measurements at the LDP site, friction velocities, u_*, were parameterized from wind speed measurements to characterize the atmospheric boundary layer at the Sonoran desert sites. The aerodynamic roughness length, z_o, was estimated using the log-wind profile, assuming a displacement heigth of $0.8h$, where h is the mean height of the vegetative canopy. At the Sonoran desert sites the major vegetative species were bursage bush and creosote bush; minor species were saguaro cactus and palo verde trees. A mean canopy height of 1 m was assumed to reflect the air-surface interaction with the dominant vegetative species. A value of h that included the sparse, taller vegetation would likely increase turbulence and air-surface exchange. Thus, exchange rates using $h = 1$ m represent a low-range estimate for the Sonoran desert sites. A value of z_o was predicted from measurements of u_* and U under near-neutral conditions and $U > 2$ m s^{-1}. The log-wind profile was then used to parameterize u_* using measurments of U. The resulting equation, $u_* = 0.12U$, was used to calculate friction velocities from hourly wind speed measurements at the WTM, DBG, and LDP sites.

C.4. Deposition Velocity Calculation

C.4.1. *Gaseous Nitrogen*

The deposition velocity represents the cumulative effect of the physical processes responsible for dry deposition including turbulent transport, diffusion, and surface interaction (Slinn, 1982; Wesely, 1989; Zhang *et al.*, 2001). The gas deposition velocity was calculated as

$$v_d = \frac{1}{r_a + r_b + r_c} \tag{C.2}$$

where r_a, r_b, and r_c are the aerodynamic, surface layer, and canopy resistances, respectively.

Gas v_d values were calculated from model parameterizations of gas deposition resistances in Equation C.2 (Wesely, 1989; Walmsley and Wesely, 1996). This parameterization did not require plant-specific information but the canopy resistance varies with land-use category (LUC), seasonal category (SC), and, gas species. Here, LUC 11 (rocky open areas with low-

growing shrubs) and SC 5 (transitional spring with partially green short annuals) was selected to best describe the Sonoran desert sites during the both measurement periods.

The aerodynamic resistance was calculated as

$$r_a = \frac{\ln(z/z_o) - \Psi_H}{k u_*} \tag{C.3}$$

where z is the measurement height, z_o is the aerodynamic roughness length, Ψ_H is the stability function, and k is the von Karman constant (0.4). The aerodynamic resistance was calculated by estimating the stability function in terms of the measurement height and the Obukhov length scale (Zhang *et al.*, 2001). The Obukhov length was estimated using a straight-line approximation of the aerodynamic roughness length as a function of Obukhov length relationship (Golder, 1972). The surface layer resistance accounts for molecular diffusion through the layer of air very near the surface

$$r_b = \frac{5\mathrm{Sc}^{2/3}}{u_*} \tag{C.4}$$

where $\mathrm{Sc} = \nu/\mathcal{D}$ is the particle Schmidt number, ν is the kinematic viscosity of air, and $\mathcal{D}$ is the particle diffusivity (Hicks *et al.*, 1987).

The canopy resistance is an area of continuing research. Multilayer models subdivide r_c into resistances of the stomata, mesophyll cells, and leaf cuticles for deposition to vegetative canopies. Transfer of gases through the cuticle is generally smaller than through the stomata and is often neglected (Meyers *et al.*, 1998). Transport through the lower canopy and to the ground are also included. The canopy resistance was calculated as

$$r_c = \left(\frac{1}{r_{st} + r_m} + \frac{1}{r_{lu}} + \frac{1}{r_{dc} + r_{cl}} + \frac{1}{r_{ac} + r_{gs}} \right)^{-1} \tag{C.5}$$

where the first term includes r_{st}, the stomatal resistance, and r_m, the mesophyll resistance; the second term is r_{lu}, the resistance of the outer leaf surface in the upper canopy; the third term includes r_{dc}, the resistance to transfer by buoyant convection in the lower canopy, and r_{cl}, the resistance to uptake by leaves and other surfaces; and the fourth term includes r_{ac}, a resistance at the ground surface for processes that depend only on canopy height, and r_{gs}, the resistance to uptake by materials at the ground surface.

The stomatal resistance was calculated as

$$r_{st} = r_j \left[1 + \left(\frac{200}{Q_* + 0.1} \right)^2 \left(\frac{400}{T\,(40 - T)} \right) \right] \tag{C.6}$$

where r_j is the minimum bulk canopy stomatal resistance for water vapor (Wesely, 1989). This equation is valid for T between 0 and 40 °C, and r_{st} was set to a large value (10^{25}) outside this range (Walmsley and Wesely, 1996). The combined stomatal and mesophyll resistance was then calculated as

$$r_{sm} = r_{st} \left(\frac{\mathcal{D}_{\mathrm{H_2O}}}{\mathcal{D}} \right) + \frac{1}{3.3 \times\ 10^{-4} H^* + 100 f_0} \tag{C.7}$$

where $\mathcal{D}_{\mathrm{H_2O}}$ is the molecular diffusivity of water vapor, $\mathcal{D}$ is the molecular diffusivity of the depositing gas, H^* is the Henry's law constant of the gas in M atm^{-1}, and f_0 is a gas reactivity factor. The gas reactivity factor is zero for most gas species, including NH_3 and HNO_3.

The leaf surface resistance in the upper canopy was calculated as

$$r_{lu} = r'_{lu} \left(\frac{1}{10^{-5} H^* + f_0} \right) + r_{\mathrm{low}} \tag{C.8}$$

where r'_{lu} is parameterized for each LUC.

The buoyant convection resistance was calculated as

$$r_{dc} = 100 \left(1 + \frac{1000}{Q_* + 10} \right) \left(\frac{1}{1 + 1000\phi} \right) \tag{C.9}$$

where ϕ is the slope of the local terrain in radians. The lower canopy resistance to uptake by leaves and other surfaces was calculated as

$$r_{cl} = \left(\frac{10^{-5} H^*}{r_{clS}} + \frac{f_0}{r_{clO}} \right)^{-1} + r_{\mathrm{low}} \tag{C.10}$$

where r_{clO} and r_{clS} are parameterizations for each LUC. The ground surface resistance, r_{gs}, was calculated from Equation C.10, using parameterizations of r_{gsS} and r_{gsO} for each LUC in place of r_{clS} and r_{clO}, respectively. The canopy height dependent resistance, r_{ac}, was a constant for each LUC.

Values for the adjustable parameters used to calculated the surface resistance for NH_3 were taken from Wesely (1989). Surface resistance to uptake of HNO_3 is generally small and deposition is controlled by the rate of transport above the canopy (Wesely and Hicks, 2000).

This species was treated as a special case and the surface resistance is set to 10 s m^{-1} or the low temperature correction, r_{low}, whichever was larger (Walmsley and Wesely, 1996). Inputs required for the gas v_d model were u_*, U, z_o, and Q_*. The aerodynamic roughness length estimated from micrometeorological measurements at the LDP site, $z_o = 0.27$, was used here in place of the LUC estimate given by Wesely (1989). Hourly HNO_3 and NH_3 deposition velocities were calculated and mean daily values were calculated from the mean of hourly v_d estimates.

Note that when the vegetative canopy is wet from rain or dew, the leaf cuticle component of the surface resistance to gaseous deposition is lower than that for a dry canopy. This adjustment was not made here because DFS samples were not collected during rain events or when air temperatures were above the dew point. The modified parameterizations given by Walmsley and Wesely (1996) should be used to account for wet conditions.

C.4.2. *Particulate Nitrogen*

Deposition velocities of particulate nitrogen were calculated as

$$v_d = \frac{1}{r_a + r_b + r_a r_b v_s} + v_s \tag{C.11}$$

where r_a and r_b are the aerodynamic and surface layer resistances, respectively, and v_s is the gravitational settling velocity.

The parameterizations of Zhang *et al.* (2001) were used to estimate particle dry deposition velocities. This model included parameterization of particle deposition velocities for several LUC and SC to represent the range of conditions necessary for a large spatial and temporal scale model. LUC 10 (shrubs and interrupted woodlands) was selected to best describe the Sonoran desert sites used in this work (see Chapter 4). The desert LUC is not appropriate in this case since the sites used in this study have a higher ratio of vegetated to open surface than those used by Zhang *et al.* (2001). Note that the 11 LUC codes of Zhang *et al.* (2001) for particle deposition velocity do not correspond to the 15 codes of Wesely (1989) for gas deposition velocity, although other LUC definitions are comparable.

The aerodynamic resistance is assumed to be independent of PM composition; r_a was

calculated using Equation C.3. The surface layer resistance was parameterized as

$$r_b = \frac{1}{u_* \left(E_B + E_{IM} + E_{IN}\right) R_1 \varepsilon_0} \tag{C.12}$$

where E_B, E_{IM}, and E_{IN} are collection efficiencies for Brownian diffusion, impaction, and interception, respectively; R_1 is the fraction of particles that stick to the surface without rebound; and ε_0 is an empirical constant with a value of 3 commonly used (Zhang *et al.*, 2001).

The diffusion collection efficiency has the form

$$E_B = \mathrm{Sc}^{-\gamma_s} \tag{C.13}$$

where γ_s is an empirical constant which varies with surface type. Slinn (1982) found $\gamma_s = 2/3$ for vegetated surfaces. Zhang *et al.* (2001) suggests $\gamma_s = 0.54$ for LUC = 10.

Several functional forms have been proposed for the impaction collection efficiency (Zhang *et al.*, 2001). Here E_{IM} is calculated as

$$E_{IM} = \left(\frac{\mathrm{St}}{\alpha + \mathrm{St}}\right)^{\beta} \tag{C.14}$$

where $\mathrm{St} = v_s u_*^2 / g\nu$ is the particle Stokes number, and α and β are empirical constants with values of 1.3 and 2, respectively, for LUC = 10.

Interception occurs when particles pass within one particle radius of an obstacle. The interception collection efficiency is calculated as

$$E_{IN} = \frac{1}{2}\left(\frac{D_p}{A}\right)^2 \tag{C.15}$$

where A is the characteristic radius of the collection surface and D_p is the particle diameter (Slinn, 1982). Estimates of A for "large" collectors (e.g. stalks, needles, etc.) and "small" collectors (e.g. vegetative hairs) have been made. For LUC = 10, A = 10 mm is suggested (Zhang *et al.*, 2001).

Particle rebound is possible for $D_p > 5$ μm, but theoretical and experimental predictions remain uncertain. Slinn (1982) and others suggest the fraction of particles that stick to the surface is

$$R_1 = \exp(-b\ \mathrm{St}^{1/2}) \tag{C.16}$$

where b is an empirical constant, often assumed to be 1 (Giorgi, 1988; Zhang *et al.*, 2001).

The inputs required for the particle v_d model were particle diameter (D_p), u_*, U, z_o, and Q_*. The aerodynamic roughness length estimated from micrometeorological measurements at the LDP site, z_o = 0.27, was used here in place of the LUC estimate given by Zhang *et al.* (2001). Hourly particle deposition velocities were calculated for 308 size bins in the range 0.003–30 μm. Particles were assumed to have the size distribution of a typical urban aerosol (Whitby and Cantrell, 1976). Mass-weighted deposition velocities, $v_d(D_p)$ were then calculated as the cross product of the hourly v_d and the fraction of mass, $x(D_p) = (dV/dlogDp)/(\sum dV/dlogDp)$, in each size bin. Hourly v_d for the fine and coarse size modes were then calculated as the mean value, $v_d = \overline{v_d(D_p)\,x(D_p)}$, for particles in each mode. Mean daily fine and coarse mode particle v_d were calculated as the mean of the hourly v_d estimates.

C.5. Nomenclature

Variables

A	characteristic collector radius
b	particle sticking constant
F	flux
c	atmospheric concentration
c_{ext}	concentration in the extract
D_p	particle diameter
$\mathcal{D}$	Brownian diffusivity
$\mathcal{D}_{\text{H2O}}$	molecular diffusivity of water
E_{B}	Brownian diffusion collection efficiency
E_{IM}	impaction collection efficiency
E_{IN}	interception collection efficiency
f_0	gas reactivity factor
F	flux
h	mean canopy height
H^*	Henry's law constant
k	von Karman constant (0.4)
L	Obukhov length
Q_*	solar radiation
r_a	aerodynamic resistance
r_{ac}	constant for canopy height dependent resistance
r_b	surface layer resistance
r_c	canopy resistance
r_{clO}	resistance of the lower canopy for ozone
r_{clS}	resistance of the lower canopy for SO_2
r_{gsO}	resistance of the ground surface for ozone

r_{gsS} resistance of the ground surface for SO_2

r_j minimum bulk canopy stomatal resistance to water vapor

r_{low} low temperature correction for canopy resistance

r'_{lu} leaf surface resistance in the upper canopy

R_1 fraction of sticking particles

RH relative humidity

Sc Schmidt number, $\mu/\rho\mathcal{D}$

St Stokes number, $v_s u_*^2/g\nu$

t sampling time

T air temperature

U mean wind speed

u_* friction velocity

v_d deposition velocity

v_s gravitational settling velocity

V volume

V_{ext} extract volume

$\dot{V}$ volumetric flow rate

x mass fraction

z measurement height

z_o aerodynamic roughness length

Subscripts

AD citric-acid-coated denuder

AF citric-acid-impregnated filter

c coarse fraction

CD sodium-carbonate-coated denuder

f fine fraction

NF nylon filter

TF Teflon filter

Greek Symbols

α empirical constant for impaction efficiency

β empirical exponent for impaction efficiency

γ_s empirical constant for diffusion efficiency

ε_0 particle surface resistance constant

θ wind direction

ϕ slope of the local terrain in radians

Ψ_H atmospheric stability function